Spin Transport In Aluminum Grains and Single Debye Relaxation In BST Nanoparticles

A Thesis
Presented to
The Academic Faculty

by

Liyuan Zhang

In Partial Fulfillment
of the Requirements for the Degree
Doctor of Philosophy

School of Physics
Georgia Institute of Technology
August, 2007

Spin Transport In Aluminum Grains and Single Debye Relaxation In BST Nanoparticles

Approved by:

Professor Dragomir Davidović,
School of Physics, Georgia Tech, Chair

Professor Alexei Marchenkov,
School of Physics, Georgia Tech

Professor Phillip First,
School of Physics, Georgia Tech

Professor Edward H. Conrad,
School of Physics, Georgia Tech

Professor Zhonglin Wang
Materials Science and Engineering, Georgia Tech

Date Approved: May, 16, 2007

To my daughter,

Gracie Zhang,

PREFACE

This thesis consists of two distinct components: (1) Spin-polarized electron transport through aluminum array nanoparticles, (2) A single electric relaxation process in Barium Strontium Titanate (BST) nanoparticles.

For the first component (chapters 2-5), we studied electron spin transport in nanometer scale aluminum grains as embedded in a ferromagnet tunneling junction. We observed tunnelling-magnetoresistance (TMR) and spin valve effects. From the TMR strong asymmetry with bias voltage, we explored spin relaxation effects. Additionally we also obtained the spin-coherence time on the order of nanoseconds by using the Hanle effect.

For the second component (chapters 6-9), we investigated the dielectric response of BST and Barium Titanate (BTA) (high dielectric constant ferroelectrics) nanoparticles. The results were found to be quite unusual when compared with the dielectric response of film or bulk. The dielectric response is Debye relaxation with only a single relaxation time, and the relaxation time exhibits the Arrhenius Law at temperatures below 200 Kelvin.

ACKNOWLEDGEMENTS

I have spent an exciting and enjoyable five years at Georgia Tech, largely due to the amazing people with whom I had the good fortune to associate. The research described in this thesis is the culmination of years of work and would not have been possible without the help of a number of people. I want to thank them for their help and support.

First of all, I am grateful to my advisor Dragomir Davidović for his advice, encouragement, and support over these years. His enthusiasm for new ideas is infectious and has helped to broaden my interest in physics. I have enjoyed learning from him.

Special thanks are given to the members of the group who participated actively in this work Cuiyun Wang, Yaguang Wei, and Xiya Liu. Not only were they helpful in my experiments, they were also around to share my frustrations and excitements, to support and to encourage. Appreciation goes to the former members of the group Andrei Korotkov, Changshi Lao, Anaya Armando, Rupa Bhaumik and Michael Bowman. I also give thanks to Judy Melton for her help editing and writing. I also recognize assistance and cooperation from Velera Pate, Kevin Carter, Keith Garner, Sam Mize, Mark Miller, Debbie James, and Lori Sheridan.

I thank Nan Liu, my wife for her love, patience, and unwavering support. She has changed my life, and made it richer in countless ways.

I also want to thank my parents, and my old brothers and sister for their love and encouragement. This work would not have been possible without their support. My parents inculcated in me the ethic for hard work, and I cannot thank them enough for that.

TABLE OF CONTENTS

LIST OF TABLES

LIST OF FIGURES

CHAPTER I

INTRODUCTION

The subject of this thesis is nanoscale physics in magnetic and ferroelectric materials. In small systems (e.g., on nanometer scale), the properties are often fundamentally different from properties in bulk. Nanoscale physics is one of the most interesting areas of condensed matter physics, because most of the things we know about bulk need to be reexamined at this small length scales.

This thesis consists of two distinct components. The first component explores spin-polarized electron transport through aluminum nanoparticle arrays. The second component covers electric relaxation in Barium Strontium Titanate (BST) nanoparticles.

As we know, long spin relaxation times for polarized carriers are necessary for the development of spintronic devices. In quantum dots, where electrons are confined in zero dimensions, spin relaxation times are strongly enhanced compared to bulk. For this reason, the spin of an electron confined in a quantum dot is a candidate quantum bit [1]. The suppression of spin relaxation in quantum dots is caused by energy level quantization, which drastically reduces the density of initial and final states involved in spin-flip transitions. Unfortunately, the spin-coherence time T_2, measured in a semiconducting quantum dot, is only $\sim$ ns, despite the fact that the spin-relaxation time is extremely long, up to $\sim$ ms [2].

In metallic grains system, the electron spin-relaxation time T_1 has not been documented. In order to gain a better understanding of spin relaxation in metallic grains (which are also quantum dots), we investigate the spin transport in metallic grains. In 1997, Agam, et al. [3], predicted that the energy relaxation time in metallic nanoparticles is much longer than that in metal film (he estimated T_e is around 10 ns). This enhancement in relaxation time is caused by the chaotic nature of the wave functions of the electrons confined in the nanoparticle. By the same token, spin-relaxation time in a metallic nanoparticle is expected to be much longer than in bulk, and electron spin in a metallic grain is also a candidate for

a quantum bit.

In the first component of this thesis, we studied electron spin transport in nanometer scale aluminum nanoparticles connected to ferromagnetic reservoirs via tunnelling junctions at 4.2 K. We found strong asymmetric tunnelling magneto-resistance (TMR) effects. This asymmetric TMR is explained by spin relaxation in aluminum grains and asymmetric electron dwell times. Then we made the estimate that spin-relaxation time T_1 on aluminum nanoparticles is extremely long, on the order of μs. This result is somewhat analogous to the discovery of ms long spin-relaxation times in semiconducting quantum dots.

We also measured the Hanle effect from spin-precession in the perpendicular applied magnetic field. The Hanle effect in the metellic grains has not been measured prior to our work. Our main result is that the spin-coherence time (T_2^*) measured using the Hanle effect, is on the order of ns. The dephasing time is extremely short compared to the anticipated long spin relaxation time T_1. Fast dephasing is attributed to electron spin-precession in local magnetic fields, which is also known as inhomogeneous broadening. Interestingly, this dephasing process does not destroy tunneling magneto-resistance, and spin transport remains partially spin-coherent. This finding reveals that the T_2, the spin-coherence time in the absence of inhomogeneous broadening, in a single aluminum grain is much longer.

This finding is also a proof of principle that one can create, transfer, and manipulate the quantum spin information in metallic grains instead of the semiconducting quantum dots. Although technologically this goal would be too difficult to accomplish today, in principle it increases our options for quantum computing, assuming that several other major challenges can be resolved in the future.

We also demonstrated that the asymmetric tunneling magneto-resistance can be dominated by controlling the structure of tunneling junction. Those behaviors make our tunnelling device work as a mesoscopic spin diode, i.e., the intrinsic spin relaxation time is longer than the dwell time on aluminum grain in one side bias voltage direction, whereas, the spin relaxation time is suppressed for the opposite one.

In the second component of this thesis, we investigated the physical properties of nanoparticles made from ferroelectric materials, such as Barium-Titanate ($BaTiO_3$ or BTA)

and Barium-Strontium-Titanate ($Ba_{(1-x)}Sr_xTiO_3$ or BST).

There seems to be no general theory of phenomena describing ferroelectric properties in nm-scale particles. By contrast, properties of individual nm-scale ferromagnetic particles and molecular magnets have been studied extensively, both experimentally and theoretically.

Nano-structure ferroelectric device has already made waves in ultrahigh density and high speed recording. In an article by Auicello [4], et al. in Physics Today, the connection between physics and applications of ferroelectric films was described. The applications of ferroelectricity include sensors, infrared detector, piezoelectric actuators, and microwave phase filters, and high-Q resonators. The most attractive application for ferroelectric materials is ferroelectric random access memories (FRAM) [4, 5, 6] because of their high dielectric constant. BST is one of the leading materials because its ferroelectric phase transition can be operated at the room temperature by setting the appropriate composition. Also BST is an innoxious ferroelectric (contains no heavy metals, such as lead).

The properties of nanometer scale ferroelectrics are also expected to be fundamentally different from those in bulk because of the small number of degrees of freedom. For example, bulk BTA is ferroelectric, while BTA nanoparticles lose ferroelectric properties when the nanoparticle diameter is below about 20 nm [7].

Recent advances in science and nanotechnology of nanoscale ferroelectric structures make it possible to investigate and understand those new physical phenomena in nanometer scale range. In addition, a better understanding of their dielectric and ferroelectric properties is essential before they may be successfully integrated in commercial devices.

Since future trends in microelectronics will be fast and high density, microelectronic cell will be made ultra small. Hence, an important question is - below a certain size, what kinds of behaviors will occur in ferroelectric polarization? Since the concept of permanent (nonvolatile) memory is that memory does not forget the information stored in it, the regime in small particles could set the ultimate limit of size below which no permanent memories can be created. If electric polarization does occur, the important questions are: Will nanoparticles in this regime still exhibit enhanced dielectric properties? Will the dielectric constant of these nano-particles exhibit strong frequency dependence?

In this second component, we investigated the dielectric response of Barium Titanate (BTA) and BST (high dielectric constant ferroelectrics) nanoparticles. We discovered that the dielectric properties are very unusual when compared with the dielectric response of film or bulk. In particular, at low temperatures, where electric dipoles are expected to be frozen in by the ferroelectric order, we find that there remains a significant fraction of electric dipoles that are responsive to external fields. The polarizability due to these dipoles is quite strong and comparable to the peak polarizability of large particles at the Currie temperature. Somehow, reduction in the particle size creates a frustration effect which prevents locking of the dipoles into the ferroelectric configuration.

Although there is no understanding of this frustration at present and more theoretical work is necessary, recent some theories predict that the nature of the ferroelectric state below certain diameter is fundamentally altered from the bulk ferroelectricity, and there is no real ferroelectricity anymore. Hence, it is not surprising to observe a significant fraction of unlocked dipoles below certain particle diameter.

The dielectric response of these unlocked (frustrated) dipoles is Debye relaxation with only one relaxation time. The relaxation time exhibits the Arrhenius Law at temperatures below 200 Kelvin. Intriguingly, the energy barrier for the frustrated dipoles is independent of samples, showing that this frustration mechanism should be calculable from the first principle calculations. Thus, we expect that this finding will stimulate further theoretical research and discover fundamental new physics for ferroelectric nanoparticles.

From a practical standpoint, the frustration of the ferroelectric state shows that there exists a fundamental limit to how small a ferroelectric memory cell can be made. Our smallest nanoparticles are on the order of 5 nm, showing that this fundamental limit occurs above 5 nm diameter.

CHAPTER II

THEORETICAL BACKGROUND

In this chapter, we will provide some important background and context about spintronics that needed to understand electron spin transport in metallic grains. We will also talk about motivation and principles of our case that metallic grains connected to ferromagnetic reservoirs via tunnelling junctions.

2.1 Spintronics Devices

Spintronics is a neology for "spin-based electronics", a rapidly emerging technology that exploits the quantum spin states of electrons, as well as the conventional electronics which are based on the charge of the electron [1, 8, 9]. To make use of electron spin, the primary requirement is to make a device that can generate the spin polarized electron current, which has a nonequilibrium state for spin-up and spin-down electrons. There are many methods to generate the spin polarized current, and the most natural way is to inject the current through a ferromagnetic material. Another requirement is this device that can detect the spin information of the electrons. In addition, the steady spin current is necessary during the electron transit time though the device. In other words, the spin relaxation time must be longer than the time it takes to inject, measure, and manipulate spin information in investigation of spin transport.

There are some well known examples of spintronics devices. Devices like giant magneto-resistance (GMR) and magnetic tunnel junctions (MTJs) spin valves (each which can store an "1/0" state that can be read by a current pulse) are about to challenge the silicon in the lucrative area of random access memory as well. Following, we will discuss them in detail.

2.1.1 Giant Magneto-Resistance

The first example of spintronics is the giant magneto-resistance. The basic structure in GMR device is a spacer layer of non-magnetic conducting metal between two ferromagnetic

layers (Figure 2.1). Those thin ferromagnetic layers tend to be aligned in the one direction when an external magnetic field is applied, whereas the magnetizations of the ferromagnetic layers are antiparallel when there is a lack of the magnetic field. Thus, there are two kinds of configurations for those two magnetic layers, i.e. parallel and antiparallel configurations that is illustrated schematically in the Figure 2.1.

In the parallel (or P) configuration, spin-up electrons can pass easily through the device whereas spin-down electrons are scattered in both two magnetic layers. Reversing the magnetization orientation of one of the magnetic layers yields the anti-parallel (or AP) configuration. In the AP case, all the spin electrons are scattered strongly within one of those magnetic layers, because the electron's spin direction is antiparallel to one of the magnetization directions wherever those electron spins are spin-up or spin-down. Hence, in the AP configuration, the total resistivity of the device is higher than the P case.

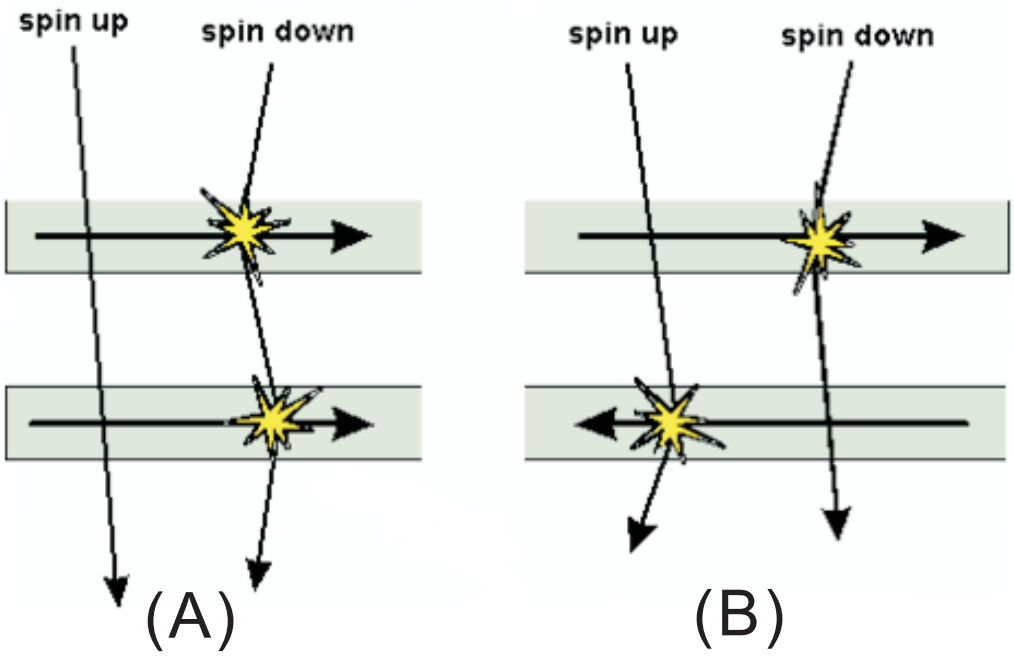

Figure 2.1: (A) GMR with low resistance in parallel magnetization configuration, (B)GMR with a high resistance is in antiparallel magnetization configuration.

From the above description, the GMR effect is then the difference of the conductivities for the P and the AP configurations. Prototypical examples comprise for example cobalt/copper and ferrum/chromium systems. The applied magnetic field is used to change

the magnetic orientation if one layer is magnetically hard and the other is soft. Note that the GMR could be as high as 80 %. Today, the commercial application of GMR effect is used in the data storage industry, such as read heads of modern computer hard disks and magnetic memory chips.

2.1.2 Tunneling Magneto-Resistance and Jullière's Model

The second example of spintronics is tunneling magneto-resistance (TMR) of magnetic tunnel junctions (MTJs). TMR is an effect of spin-dependent tunnelling. In the first part of this thesis, we will focus on the TMR effect.

The main structure of MTJ is illustrated schematically in Figure 2.2. This device consists of two ferromagnetic electrodes (F1 and F2), and they are separated by a thin insulating barrier layer (e.g. thin aluminum oxide layer), in contrast to the GMR which utilizes a conducting non-magnetic layer. When a bias voltage is applied between ferromagnetic electrodes (F1 and F2), the electrons will tunnel through the insulating barrier. Similarly, the TMR is also the change of the resistivity when turning from the P to the AP configuration. Most experiments on TMR are performed by measuring the electric current in MTJs. The external applied magnetic field is used again to switch the magnetic orientation of the magnetic parts of the system.

The discovery of TMR retrospect to 1970's, Tedrow and Meservey did a series of the pioneering experiments [10, 11, 12] using superconducting layers as detectors. They measured the spin polarization of the tunnelling current from different ferromagnetic electrodes.

To explain the TMR effect, Jullière [13] proposed a simple model (called as Jullière model). The key of this model is the density of states (DOS) in the ferromagnetic electrodes. The DOS is the number of electronic states per energy (interval). For a normal metal like copper, the DOS for spin-up electrons is equal to that of spin-down electrons. But for a ferromagnetic material like cobalt, the DOS is spin dependent. In fact, the spin-up DOS can be viewed as shifted down in energy with respect to the spin-down DOS that appears to be shifted upward in energy. Furthermore, the spin-up DOS is typically less than the spin-down DOS at the Fermi energy (in cobalt) (see Figure 2.3). In this figure, the distinction

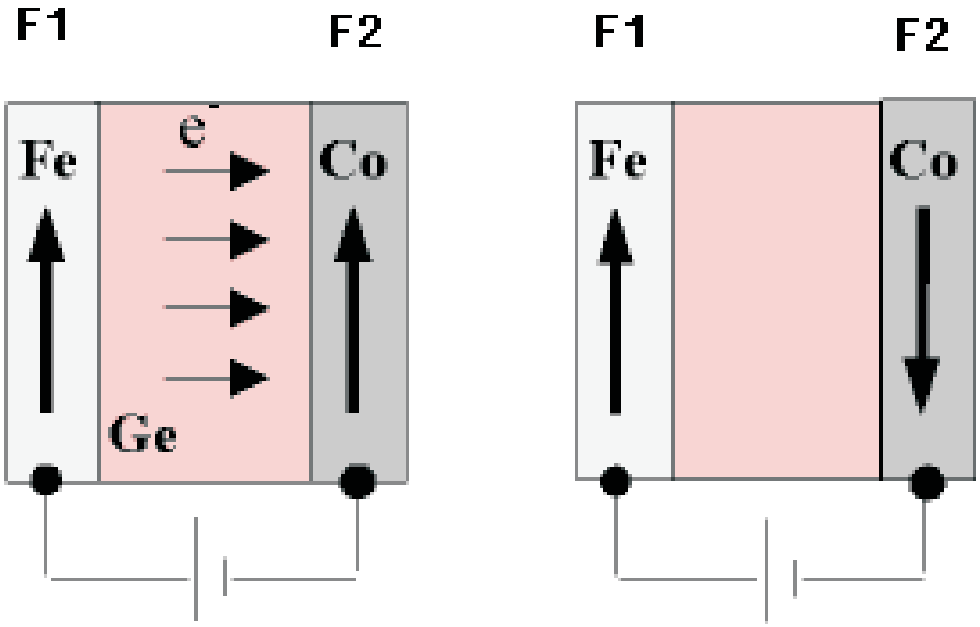

Figure 2.2: Jullière experimental setup (parallel and antiparallel states), spin polarized electrons are tunnelling from Fe to Co, which is either parallel or antiparallel magnetization configuration.

between up and down spin relies on the orientation of the magnetic moments. As we will see later, both orientations can be the majority or the minority spin orientation. The spin-up refers to the majority spin and spin-down to the minority spin. Here, we are concerned in the following with 4 partial DOS configurations, either up or down for the two electrode Left (L) and Right (R) (see Figure 2.4).

The idea of Jullière model is to relate the probability of tunneling between the electrodes to the DOS. This is quite plausible because the probability will be zero if there are no electronic states to tunnel from or to tunnel into. With zero bias voltage, one has to consider only the states at the Fermi energies of the ferromagnetic electrodes.

For the P configuration, the conductance is then proportional to the DOS product of the left and the right ferromagnetic electrodes. We have to sum over both spin channels (or spin orientations), since without spin-orbit coupling, the spin-flip processes do not take place.

In the AP configuration, one reverses the orientation of the magnetization in the right

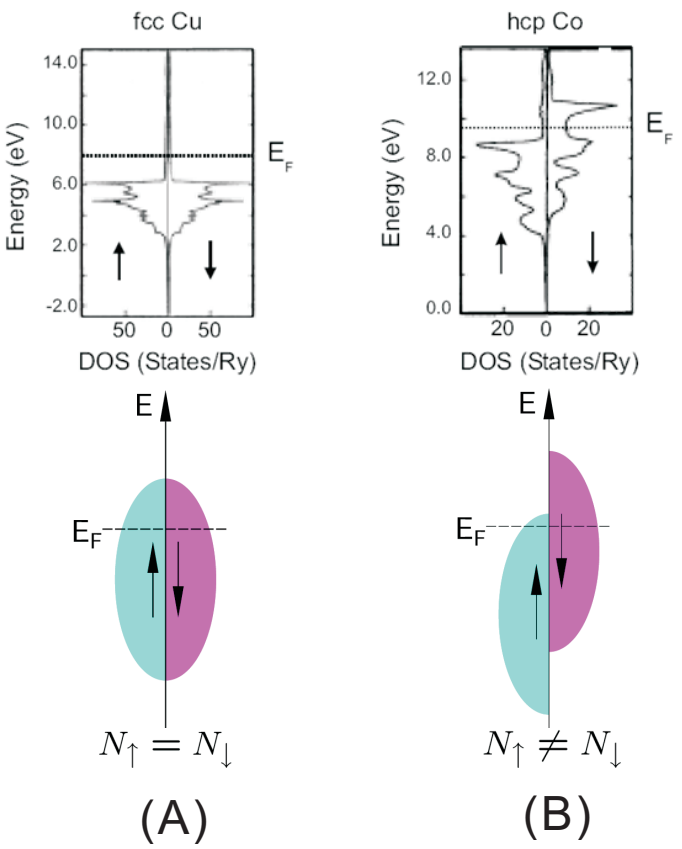

Figure 2.3: (A) DOS of a normal metal (i.e., Cu), is symmetry at the Fermi energy.(B) DOS of a ferromagnetic metal (i.e., Co), is asymmetry at the Fermi energy. Note that although the total number of spins for spin-up (majority spins) is larger than that of spin-down (minority spins), the density of states at the Fermi energy has the opposite distribution - more states of the minority-spin than the majority spin. For simplicity, the bands of a ferromagnet are often approximated with semi-elliptic bands (shown in the bottom). This simple picture exemplifies the complicated band structure of ferromagnets. See reference [13].

ferromagnetic electrode. Therefore, the orientation of majority- and minority-spin electrons reverses. The DOS of the former spin-up electrons becomes that of the now spin-down electrons, and vice versa. Hence, the conductance is given now by the spin-mixed DOS products.

As we have seen for cobalt, the DOS for down electrons is rather large compared to that of the up electrons. Hence, G(P) is governed by the down-down DOS product, giving a large conductance. In the AP configuration, we have to multiply the small up DOS by the larger down DOS, resulting in a medium conductance. Therefore, the conductance for the

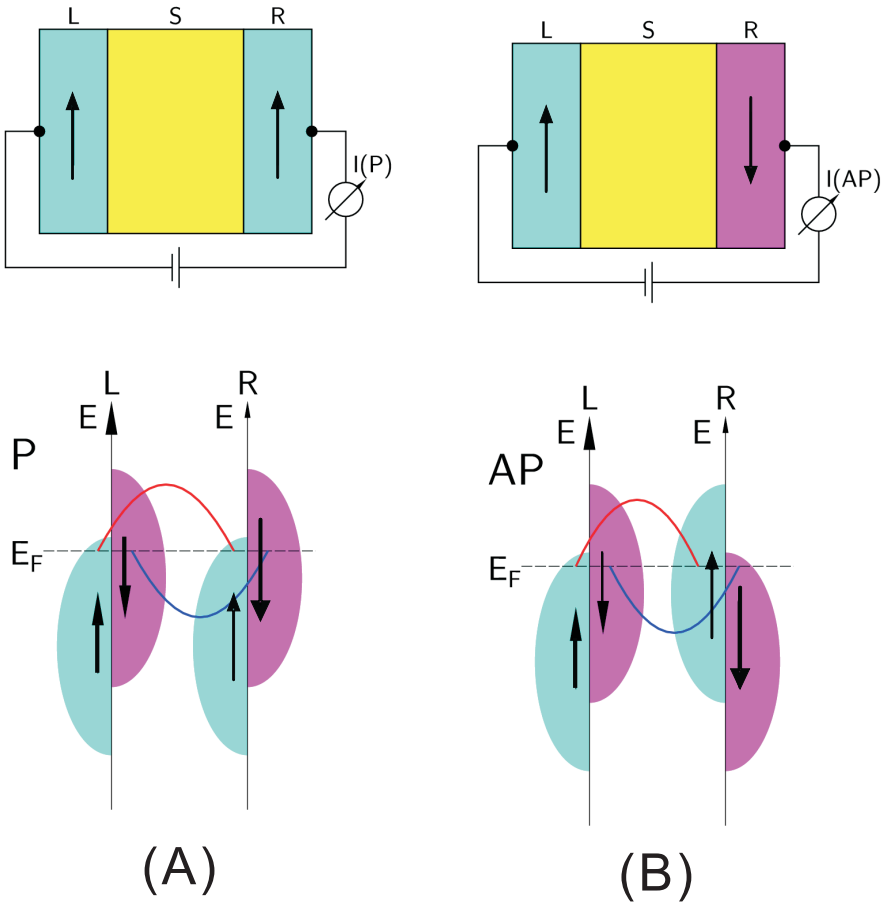

Figure 2.4: (A) Tunelling junction in parallel configuration with low resistance, the resistance reduced because the DOS product reduced (B) Tunelling junction in antiparallel configuration with high resistance, because the DOS product is larger than that of parallel configuration.

parallel and antiparallel alignment, G_P and G_{AP}, can be written as follows:

$$G(P) \propto N_L^{\uparrow} N_R^{\uparrow} + N_L^{\downarrow} N_R^{\downarrow} \tag{2.1}$$

and

$$G(AP) \propto N_L^{\downarrow} N_R^{\uparrow} + N_L^{\uparrow} N_R^{\downarrow} \tag{2.2}$$

Normally, G(P) is typically larger than G(AP), where $N_i^{\uparrow}$ and $N_i^{\downarrow}$ are the tunnelling DOS of the ferromagnetic electrodes (designated by index i = L, R) for the majority- and minority-spin electrons.

Then, the TMR is given by the difference of the conductances. Introducing the spin polarization as the asymmetry of the spin-resolved DOS, the TMR equals the product of the two ferromagnetic electrode spin polarizations. Hence, the TMR is independent of the spacer in Jullière model. If one of the electrodes is a normal metal (P = 0), that is, non-magnetic, the TMR vanishes, as it should. P_L and P_R are the spin polarizations of the two ferromagnetic electrodes.

It follows from equations 2.1 and 2.2 that the parallel and antiparallel-magnetized MTJs have different conductances, which implies a non-zero TMR. The TMR is defined as the conductance difference between parallel and antiparallel magnetizations, normalized by the antiparallel conductance, i.e.,

$$TMR = \frac{G(P) - G(AP)}{G(AP)} = \frac{I_{\uparrow\uparrow} - I_{\uparrow\downarrow}}{I_{\uparrow\downarrow}} \tag{2.3}$$

where $I_{\uparrow\uparrow}$ and $I_{\uparrow\downarrow}$ are the currents in the parallel and the antiparallel magnetization configurations, respectively. Using equations 2.1 and 2.2, we arrive then at Jullière's formula:

$$TMR = \frac{2P_L P_R}{1 - P_L P_R}. \tag{2.4}$$

Then the TMR is expressed in terms of the effective spin polarization of the two ferromagnetic electrodes:

$$P_i = \frac{N_i^{\uparrow} - N_i^{\downarrow}}{N_i^{\uparrow} + N_i^{\downarrow}}. \tag{2.5}$$

The Jullière's model can be used to interpret a number of experiments on TMR. Later, Slonczewski developed a simple quantitative model (Slonczewski model), that was the first accurate theoretical consideration of TMR. He treated the insulator layer as a rectangular potential barrier, and two ferromagnetic electrodes are described by two parabolic bands. Then, the Schrodinger equation was solved to determine transmissivity, which is given by the current expression for the total wave function. The potential between the electrodes is constant but differs for up and down electrons. Hence, one can obtain the conductance,

which is a function of the relative magnetization alignment of the two ferromagnetic electrodes. From this, one can also obtain the TMR that can be written as in Jullière's model as a product of two spin polarizations and a transmission factor.

2.1.3 Spin Valve

The third example of spintronics is the spin valve effect, which is one of most successful effects used in spintronic devices to date. Spin valves are used in magnetic sensors and hard disk read heads.

Normally, the device is composed of two material layers with different hysteresis curves so one layer ("soft" layer, e.g., Cr) changes polarity while the other ("hard" layer, e.g., Fe) keeps its polarity. In the Figure 2.5, the top layer is soft and the bottom layer is hard.

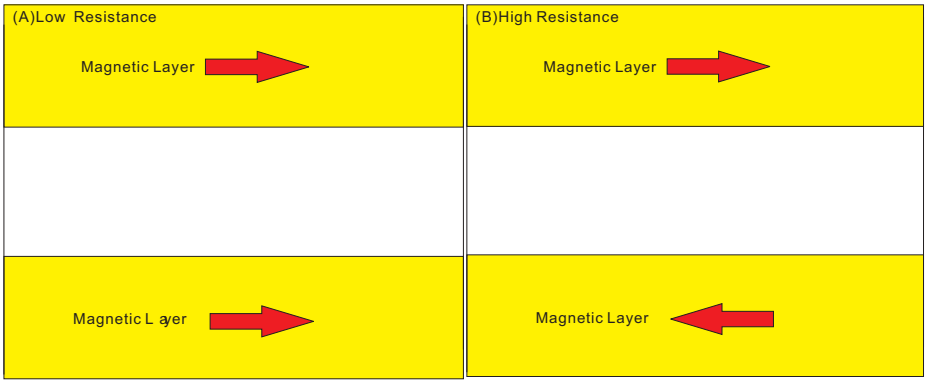

Figure 2.5: (A) Spin valve with the parallel configuration (normally it has low resistance), (B) Spin valve with antiparallel configuration (normally it has high resistance).

When a ferromagnetic layer is polarized, the carrier electrons align their spins to the external magnetic field. Once a potential exists across a spin valve, the spin-polarized electrons keep their spin alignment as they move through the device. If these electrons encounter a material with a magnetic field pointing in the same direction (see Figure 2.5 (A)), the electrical resistance of the device is normally at its minimum. If these electrons encounter the opposite direction of magnetic orientation layer compared with the external magnetic field (see Figure 2.5 (B)), then they have to flip spins to find an empty energy state in the new material. This flip requires extra energy that normally causes the device to have a higher resistance than when the magnetic materials are polarized in the same

direction.

2.2 Spin Relaxation and Mechanisms

In this section, we will discuss with the spin relaxation, and use two phenomenological parameters T_1 and T_2 to describe the processes of spin relaxation. We also will introduce three main mechanisms for spin relaxation.

2.2.1 Spin Relaxation

Spin relaxation refers to processes that unbalanced population of spins change into equilibrium. The presence of several types of interactions will cause the non-equilibrium of population of spins to decay exponentially towards zero.

Two main relaxation processes can be identified. The z component of the spin (i.e., the component along the spin quantization axis) decreases as individual spins flip, bringing the population towards equilibrium. However, this direct process in a magnetic field requires energy relaxation towards the lattice (therefore named spin lattice relaxation T_1), and as a consequence is a rather slow process.

The second type of process that is not requiring energy exchange, but this process can destroy the coherence of the perpendicular component. Because every spin will see the field created by the neighboring spins, the precessing in a local field contains a random component. This causes the perpendicular component to decay with a different time constant T_2 (also called as spin decoherence time).

T_2 can be much faster than longitudinal spin-relaxation time T_1 because decoherence is sensitive to spatial and temporal inhomogeneities. These inhomogeneities are important in measurements of decoherence in ensembles of spins. The spin decoherence by the these inhomogeneities is reversible and can be reduced by careful sample design and special spin-measurement techniques (such as spin-echo).

To express them in mathematic form, we assume that the good spin quantization axis is the z axis (the applied magnetic field direction). The total spin of the system is $\mathbf{S}$ and the external magnetic field is $\mathbf{B}$. The symbols $\parallel$ and $\perp$ describe the components parallel and

perpendicular to the z axis. The time evolution of the spin can be described by the Bloch equations:

$$\frac{dS_\perp}{dt} = \gamma(B \times S_\perp) - S_\perp/T_2 \tag{2.6}$$

$$\frac{dS_\parallel}{dt} = \gamma(B \times S_\parallel) - (S - S_\parallel)/T_1 \tag{2.7}$$

Here, T_1 and T_2 are the two phenomenological constants that describe spin flip processes. The longitudinal spin relaxation time (T_1) is the decay time from a spin-down state into a spin-up state in a strong magnetic field applied parallel to spin direction. At low temperatures, this decay process involves emission of energy into the environment (phonon, for example). This relaxation is irreversible.

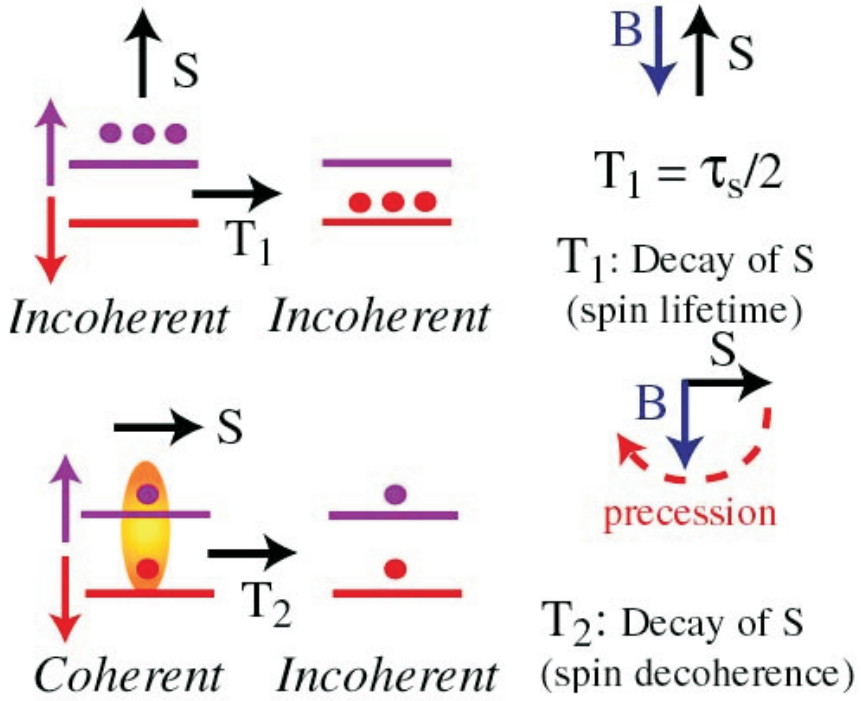

Figure 2.6: Spin coherence times (T_1 versus T_2). Here, T_1 and T_2 are the two phenomenological constants that describe spin flip processes. T_1 is the decay time from a spin-up state into a spin-down state, and spin direction is parallel to the applied strong magnetic field. T_2 is the time for transverse electron spins to lose their phase, and T_2 is also called as spin decoherence time. The electron spin direction is perpendicular to the applied magnetic field.

The T_2 is classically the time it takes for an ensemble of transverse electron spins, initially precessing in phase about the longitudinal field, to lose their phase due to spatial-temporal fluctuations of the precessing frequencies. Here, it needs to point out that T_2^* is used to describe spin dephasing of ensemble spins, while the symbol T_2 is reserved for irreversible loss of the ensemble spin phase. In general, $T_2^* \leq T_2$.

One method to measure spin-coherence time is to find spin-relaxation time in zero magnetic field, which can be done by injection and detection using ferromagnets. Another method to find T_2 is to measure the transverse spin-relaxation time in a strong magnetic field, using spin resonance.

The maximally long spin-coherence time, T_2 is limited by the coupling between spins and the excitations in the environment. The decoherence from the environment is irreversible and has the same physical origin as the longitudinal spin-relaxation process, and it can not be connection.

2.2.2 Spin Relaxation Mechanisms

In metals and semiconductors, three main spin relaxation mechanisms were found as the most relevant for conduction electrons. They are:

(1) The Elliot-Yafet mechanism [14], it arises because real crystals Bloch states (i.e, momentum eigenstates) are not spin eigenstates anymore. The physical origin of the spin mixing in the Bloch states is that the lattice ions induce a local atomic electric field, which, via the spin orbit interaction, will mix spin up and spin down states (see Figure 2.7 (A)).

The Elliot-Yafet mechanism leads to a spin relaxation rate $1/T_2^*$ proportional to the momentum scattering rate. Usually this is expected to be the main spin-flip mechanism in metals. If Elliot-Yafet is the main spin scattering mechanism, the spin flip length $\lambda_{sf} = \sqrt{D\tau_{sf}}$ will be linearly proportional to the mean free path.

(2) D'yakonov Perel' mechanism [15], this mechanism is related to spin mixing due to the presence of a finite electric field in crystals lacking inversion symmetry (the crystal field). In this case, the electrons feel a momentum dependent effective magnetic field and the spin precesses around this effective field (see Figure 2.7 (B)). The process can be imagined as a

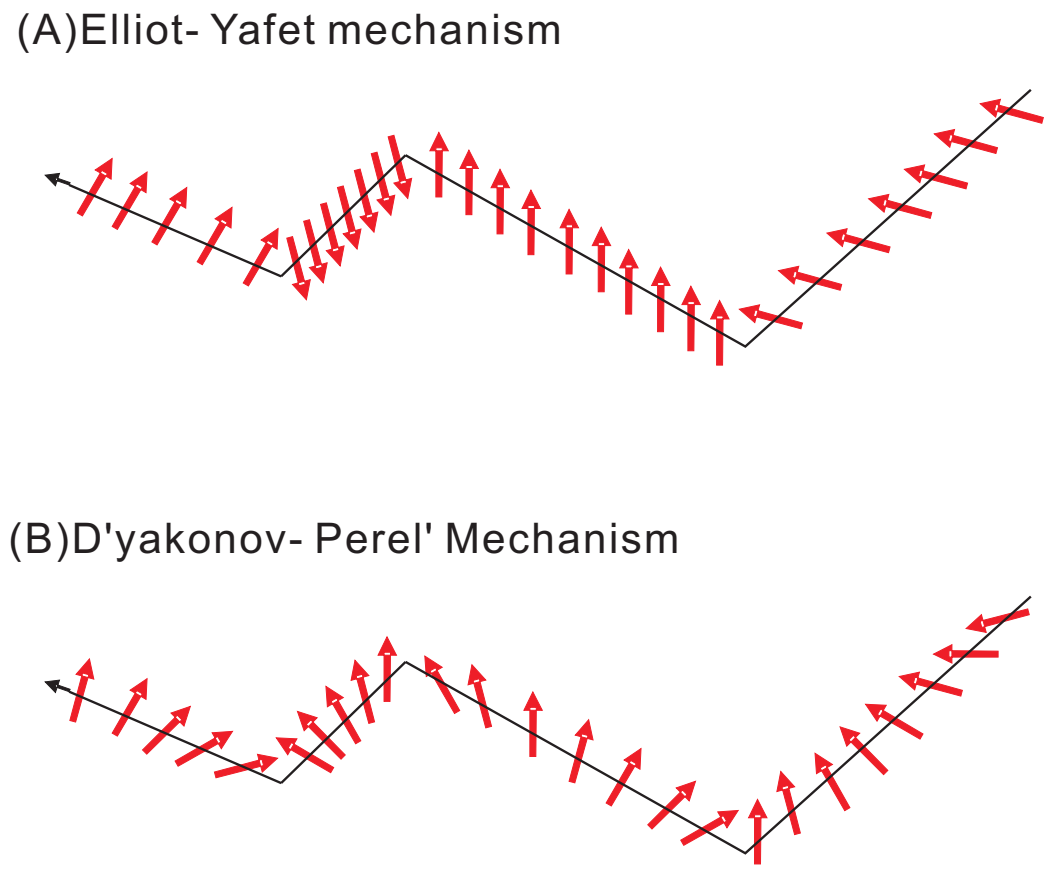

Figure 2.7: (A) The Elliot-Yafet spin flip mechanism is due to the interaction of spins with the electric field of the atomic nuclei. The corresponding spin lifetime is proportional to the momentum scattering time. (B) The D'yakonov Perel' spin flip mechanism is due to the presence of a crystal field, and the spin flip length is independent of the mean free path.

random walk in spin space. Since the spin relaxation rate will be inversely proportional to the momentum scattering rate, the corresponding spin flip length will be independent of the mean free path. Thus, the dependence on the momentum scattering rate will be canceled out by the diffusion constant.

(3) Bir-Aronov Pikus mechanism [16], this mechanism plays an important role in semiconductors with a high overlap between the electron and hole wave functions, and it is due to the electron-hole exchange interaction. Because of different effective mass and effective hole concentration, it will produce an fluctuating effective magnetic field that is generated by the total spin of holes. This magnetic field induces a precession of the electron spin around an instantaneous axis, analogous to the D'yakonov Perel' mechanism.

2.3 Our Motivation

The goal of the this part of this thesis is to investigate the phenomena and mechanism of electron-spin relaxation in nanometer scale normal metal grains (quantum dots). As we mentioned before, it is necessary that the polarized carriers have long spin relaxation times for spintronic devices. In a quantum dot, the conduction electrons spin will be confined to a small volume (one said to exist in zero dimension ($0D$)). The spin relaxation times are expected to be enhanced and influenced dramatically by this confinement.

In semiconductor, one of the challenges faced in spintronics is that electron spin can be flipped in normal metals and semiconductors, which can lead to a finite relaxation time of the spin-polarized current. The electron spin relaxation time can be enhanced by orders of magnitude as a function of dopant concentration [17].

At present, most measurements of spin-relaxation have been used by optical techniques in semiconductor quantum dots. In semiconducting heterostructures and quantum dots [18], electron spin relaxation times on the order of nanoseconds persist, even at room temperature.

Because of its stability, the spin of an electron confined in a semiconducting quantum dot has been proposed as a candidate quantum bit [19, 20]. It has been shown theoretically that the dominant spin-flip scattering mechanisms of the bulk become significantly suppressed in quantum dots because of the the zero-dimensional character of the electronic wavefunctions [21, 22]. The theoretical predictions have been confirmed experimentally in GaAs quantum dots. Recently longitudinal spin relaxation times (T_1) exceeding 200 μs [23], 50 μs [24], similar to 0.85 ms [2], have been demonstrated.

Another most natural method for injecting spins into quantum dots would be to use ferromagnets as electron source and drain reservoirs. Spin-polarized current can also be generated without ferromagnets, using semiconductors in strong magnetic fields. Ferromagnets have the advantage that they have spin-dependent density of states in zero magnetic field, which makes it possible to investigate spin-relaxation in zero magnetic field. Spin relaxation in zero magnetic field is the same as spin decoherence.

Effective electrical injection of spin polarized carriers into nonmagnetic semiconductors

has proven to be quite difficult. A possible explanation is that the conductivity mismatch between the metallic injecting electrodes and the semiconductor [25] reduces spin-injection efficiency.

However, effective spin-injection into normal metals is well established experimentally [26, 27]. So, if it were possible to attain long spin relaxation in a metallic system, the problem of inefficient spin injection could be bypassed. Thus the determination of the spin relaxation in metallic systems should be useful in the spintronics community.

It has been shown that the spin relaxation time in homogeneous metal films is rather small. The dominant spin-relaxation mechanism is caused by the spin-orbit interaction.[14, 28]. Spin-flip scattering through spin-orbit interaction leads to a spin relaxation time τ_{SO} that is proportional to the momentum relaxation time τ, $\tau_{SO} = \tau/\alpha$. This equation is known as the Elliot-Yafet relation. At low temperatures, where electron-phonon scattering is suppressed, τ becomes equal to the elastic electron scattering time. The scattering ratio $\alpha \ll 1$ depends on the atomic number and band structure of the metal. In aluminum thin films, for example, α is enhanced by the "spin hot-spots" in the band-structure [29, 30, 31] and the spin relaxation time is $T_1 \sim 0.1$ ns [32]. This time is too short to be useful for quantum computing.

Since the physical properties change in a fundamental way in response to the confinement, it not be surprising that the spin-flip process in metallic grains is very different from that in bulk. Analogous to the way that spin relaxation time is enhanced in semiconducting quantum dots relative to bulk semiconductors [21, 22], we expect that the spin relaxation time in nanometer-scale metallic grains should be much longer than that in bulk metals or metallic thin films.

There has been little investigation into spin relaxation in metallic grains. Deshmukh et al.[33], have found that the energy-relaxation time of some excited states in an aluminum grain in a weak magnetic field was comparable to or larger than 19 ns. The spin-preserving energy relaxation time, on the other hand, was predicted to be ~ 10 ns [3], suggesting that the spin-relaxation time may be comparable to or larger than 19 ns.

Spin-polarized transport through a metallic grain with quantized levels has not yet

been studied experimentally and has been studied theoretically only very recently [34]. It has been predicted that spin-polarized transport in metallic grains exhibits novel physical properties, such as exchange interaction induced spin precession.

In order to gain a better understanding of spin relaxation in metallic grains, fundamental questions need to be answered (i.e., how long is the spin decoherence time, and how is spin decoherence measured in metallic grains, and what is the mechanism of spin relaxation in nanometer scale metal grains). Once a measurement technique is developed, we shall study the origin of spin decoherence in metallic grains. One challenge is that spin decoherence time is possibly very long, so one needs to think how to access experimentally such a long relaxation time scale. Also other properties of metallic grains are needed to gain a better understanding. For example, studying spin decoherence shows it is possible to explore effects of shape anisotropy in normal metal nanoparticles (for the first time). In addition, statistical distributions of electron g-factors are studied.

In this thesis, we will investigate spin transport in nanometer-scale normal metallic particles connected to ferromagnetic reservoirs via tunnelling junctions. The interplay between single electron charging effects and ferromagnetism in single metallic particles was studied both experimentally [35, 36, 37] and theoretically [38, 39, 40, 41, 42, 43, 44, 45, 46, 47, 48]. In these studies, however, metallic particles were large and did not exhibit discrete quantum states. For a recent review, see reference [49]. In nanometer-scale aluminum particles, Deshmukh and Ralph [50] have used discrete quantum states as spin-filters to investigate spin-polarization effects in one ferromagnetic reservoir.

We use cobalt to make the reservoirs, and nonmagnetic metals (aluminum) to make the nanometer scale grains. The grains are sufficiently small so that the energy level spacing is smaller than the thermal energy at our experimentally accessible temperatures. The relaxation time of electron spins is determined through spin injection and detection, and extensions of these techniques, such as conduction-electron-spin-resonance (CESR). We will investigate spin-polarized transport through ensembles of aluminum grains, i.e., through a large number of aluminum grains placed in parallel (in about 10^{10} grains). But we do not investigate spin polarized electron transport in single grains.

2.4 Spin Transport in Metallic Grains

2.4.1 Elliot-Yafet Mechanism in Metallic Grains

In individual nanometer scale metallic grain, the conduction electrons are confined to a small volume - this is said to exist in zero dimension ($0D$) [51, 52, 53]. This confinement has a profound influence on the physical properties of the material [54, 55], thus opening up a new way to study these properties. Examples include studies of superconductivity [56], ferromagnetism [57, 58] , electron-electron interactions [33, 59], and the spin-orbit interaction [60, 61, 62, 63].

Consider a metallic grain in weak tunnel contact with two reservoirs (electron source and drain). If an electron enters the grain from one reservoir and then exits to another reservoir, one would naively expect that the spin-flip probability is small if the transit time through the grain is smaller than τ/α and that the spin-flip probability is large if the transit time through the grain is larger than τ/α. τ is the momentum relaxation time in the grain. However, this naive picture is incorrect because of the quantization of energy.

In 0D, the probability of a spin-flip through momentum scattering is independent of the transit time. In nanometer scale grains, the spin-orbit interaction only changes the energy levels and the eigenstates and does not lead to spin-relaxation [54, 64, 65]. Only interactions between electron spins and the environment can lead to spin-relaxation [21, 22]. Such interactions include spin-orbit coupling to phonons and hyperfine coupling to nuclear spins.

In the metallic grains system, we assume that the grains are ballistic. In this case, the elastic scattering time inside the grains is given by $\tau = D/V_F$, where D is the grain diameter and V_F is the Fermi velocity. The electron dwell time on the grain (τ_0) is roughly equal to $\frac{Rh}{R_Q\delta}$, where $R_Q = h/e^2 = 25.8k\Omega$ is the resistance quantum, δ is the single-electron level spacing of the grain, and R is the resistance of the tunnelling junction through which an electron exits the grain [55].

In zero magnetic field, the eigenstates of the grain are two-fold degenerate because of the Kramers degeneracy [54]. Theoretically, the spin-orbit interaction in $0D$ is characterized by a strength parameter $S = h/(\tau_{SO}\delta)$, where $\tau_{SO} = \tau/\alpha$ [64, 65]. S is independent of the

transit time. If $s \ll 1$, then spin-orbit scattering is weak. In this case, the eigenstates are approximately pure spin-up and spin-down states, and the g-factors are close to 2. The calculations predict the g-factors slightly smaller than two, [59, 64] roughly,

$$2 - g \sim S^2 \sim (\frac{D}{D^*})^4, \tag{2.8}$$

Where D^* is a characteristic diameter defined below.If $s \gg 1$, then spin-orbit scattering is strong, and the spin-up and spin-down states are significantly mixed in the eigenstates. The g-factors are suppressed significantly (g $\gg$ 1/s $\ll$ 2.0), and they vary among different energy levels and different directions of the applied magnetic field ($rms(g \sim g)$). The characteristic diameter, defined as $D^* \sim \lambda_F/\sqrt{\alpha}$, D^* is a borderline diameter. If $D < D^*$, then spin-orbit scattering is weak; if $D > D^*$, then spin-orbit scattering is strong. The effects of spin orbit interaction on energy levels and g-factors in metallic grains have been investigated thoroughly, both experimentally [60, 61, 62, 63] and theoretically [59, 64, 65]. The experiments are in good agreement with the theory.

2.4.2 Spin Transport Though Grains

Here we will discuss electron spin transport through metallic grains in weak tunnelling contact with ferromagnetic reservoirs. Spin transport is used to measure spin-relaxation effects.

We assume that the junctions in Figure 2.8 are asymmetric. The average resistance between Left and the grains (R_L) is much smaller than the average resistance between the grains and Right (R_R), i.e., $R_L \ll R_R$. At positive bias, electrons flow from L to grains and from grains into R. The average dwell time of an electron on the grains is $\tau_+ = \tau_R \sim \frac{hR_R}{\delta R_Q}$. For negative bias, electrons flow from R to grains and from grains to L. The average dwell time is $\tau_- = \tau_L \sim \frac{hR_L}{\delta R_Q}$. So, $\tau_- \ll \tau_+$.

Next, we investigate the effects of spin relaxation on tunneling magneto resistance. The TMR definition is described in equation 2.3.

To apply the jullière's model of spin polarized tunneling, we neglect single-electron charging and spin relaxation effects, and assume that spin-polarized current arises from the

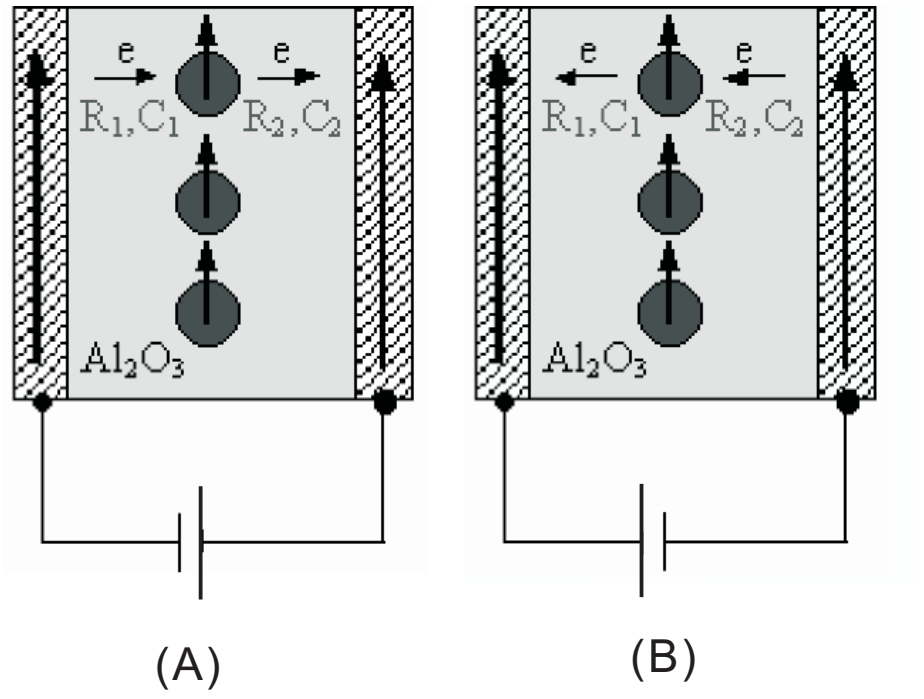

Figure 2.8: (A) The negative bias voltage across tunnelling junction, (B)The positive bias voltage across tunnelling junction.

different densities of spin-polarized carriers in the reservoirs. We obtain:

$$TMR = 2P^2, \tag{2.9}$$

Where P have the same form in equation 2.5

$$P = \frac{N_\uparrow - N_\downarrow}{N_\uparrow + N_\downarrow}, \tag{2.10}$$

and we assume $P^2 << 1$.

It is the degree of spin-polarized density of states in the ferromagnets, and $N_\uparrow$ and $N_\downarrow$ are the densities of states of spin-up and spin-down electrons. This result is similar to the usual expression for TMR of tunnelling junctions [13].

If we take into account spin relaxation, then injected spins decay during the dwell time, which reduces the spin polarization when electrons exit the grains. In particular, if the spin polarization at the injector is P, then, when an electron exits the grain at the detector, the spin polarization is reduced to a value $P' < P$ and the detector senses the reduced P_0. In

this simplest model, $TMR = 2PP' < 2P^2$.

P' depends on dwell time and spin-relaxation time T_2. Assume that $\tau_L < T_2 < \tau_R$. When the negative bias voltage is applied, electron transport is faster than spin-relaxation, so $P' \sim P$ and $TMR = 2P^2$. However, at positive bias, spin-relaxation is faster than electron transport, and we measure $TMR = 2PP' < 2P^2$. Thus, a signature of spin-relaxation in grains is an asymmetry in TMR around zero bias voltage.

2.4.3 Hanle Effect in Metallic Grains

The Hanle effect was discovered and explained by the German physicist Hanle eighty years ago. The effect is observed optically in an increase in the degree of depolarization of the resonance fluorescence.

Hanle measurements have been realized in semiconductor quantum dots [66]. The spin dephasing time ($T_2^\star$) can be extracted from the depolarization of their photoluminescence in a magnetic field perpendicular to the spin direction. The optical realization of such a Hanle experiment involves the measurement of the fluorescent emission of polarized light from semiconductor quantum dots. This method is used to measure an ensemble of spins, thus the total signal varies with the spin dephasing time $T_2^\star$ rather than the decoherence time $T_2 > T_2^\star$, or $T_2 >> T_2^*$ in a typical case.

In our tunnelling junctions, the structure is composed of two ferromagentic electrodes, and grains are embeded in the junction. The number of grains that participate in electron transport is not known making it difficult to estimate the resistances between the grains and the reservoirs. As a result, τ_L and τ_R cannot be extracted from TMR and the IV curves because we do not know the values of R_L and R_R. Fortunately, because electron transport is spin-polarized, we can use the Hanle effect to characterize the spin dephasing time $T_2^\star$ [26]. This Hanle measurement experiment can be realized by using electron spin current transport through aluminum grains, and applying the magnetic field perpendicular to the magnetization direction.

The Hanle effect in a quantum dot has recently been calculated by Braun, et al.[67]. In their calculation, they showed that a perpendicular field induces Larmour precession of the

injected spin, which reduces spin polarization of the current.

Their device consists of a quantum dot and two ferromagentic electrodes with magnetization directions anti-parallel to each other (see Figure 2.9).

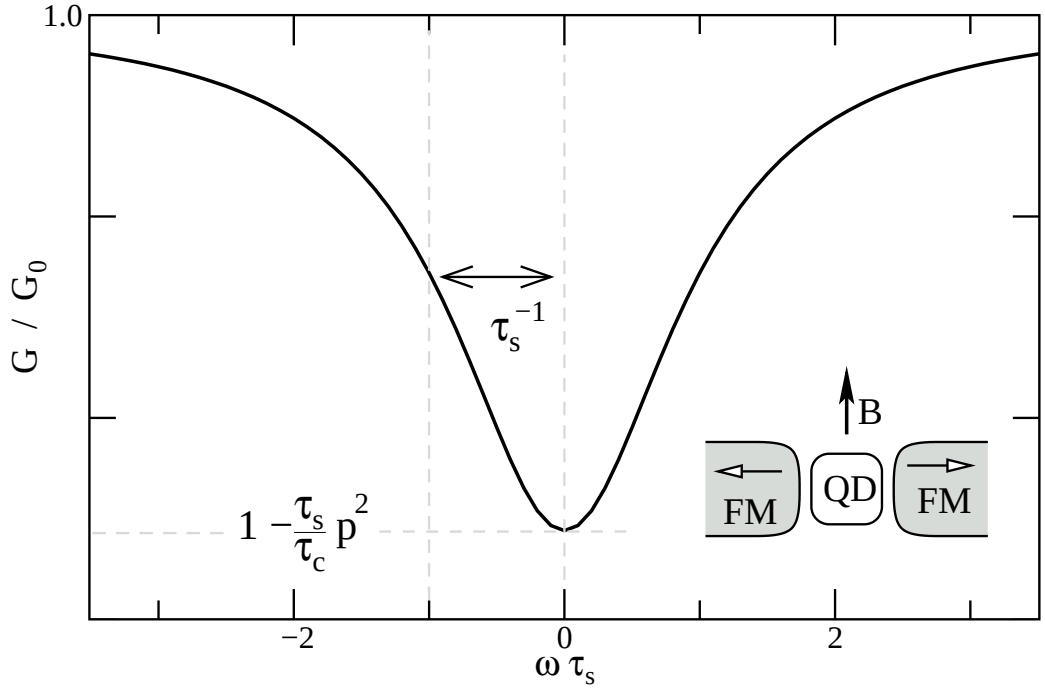

Figure 2.9: Differential conductance, for ferromagentic leads with anti-parallel magnetization, as a function of the magnetic field ω applied perpendicular to the accumulated spin. The half line width of the Hanle resonance directly determines the spin coherence time τ_s. From reference: Braun, et al., "Hanle effect in transport through quantum dots coupled to ferromagnetic leads" Europhysics Letters, 2005,72 (294–300).

In their calculation, they assumed that their device has symmetric coupling constants, $\Gamma_{\rm L} = \Gamma_{\rm R}$, with an equal degree of polarization $P_{\rm L} = P_{\rm R} = P$ and in a linear-response regime. The exchange field originating from the left and the right tunnel barrier cancel out each other so $\omega_{\rm x} = 0$, and the dot spin precesses due to the external magnetic field. The linear conductance, then, is:

$$\frac{G}{G_0} = 1 - p^2 \frac{\tau_2^*}{\tau_{\rm c}} \frac{1 + (\frac{\hat{\boldsymbol{n}}_{\rm L} - \hat{\boldsymbol{n}}_{\rm R}}{2} \boldsymbol{\omega}_{\rm B} \tau_2^*)^2}{1 + (\boldsymbol{\omega}_{\rm B} \tau_2^*)^2} \,. \tag{2.11}$$

Finally they assumed the field to be aligned perpendicular to the electrode magnetizations (see figure 2.9), and their calculation results showed the Lorentzian dependence on

the external magnetic field that familiar from the optical Hanle effect. The depth of the dip was given by $p^2\tau_2^*/\tau_c$ while the half-width of the dip in figure 2.9 provides a direct access to the spin coherence time τ_2^*.

CHAPTER III

SAMPLE FABRICATION AND MEASUREMENT PROCEDURES

The idea that electron tunneling could be used to probe properties of nanometer scale metallic clusters is several decades old, and was pioneered by Giaever and Zeller [68]. Our device is a recreation of a tunnelling device made by Zeller and Giaver in the 1960s , which demonstrated Coulomb blockade for the first time. The difference between our sample and the prior devices is that we have spin-polarized leads. Our measurements involved measuring the I-V characteristics of metallic clusters embedded in insulating films; this allowed us to probe the charging properties. However, these measurements were ensemble measurements since a large number of metallic clusters were involved in the current transport.

There are practical reasons to investigate spin-transport through ensembles of aluminum grains. These include: 1) the devices containing a large number of grains are easier to fabricate than devices containing a single grain; 2) measured properties are ensemble averages; consequently the data is sample to sample reproducible.

3.1 Sample Fabrication

The device fabrication process is not lithography based and it is relatively simple. Device geometry is sketeched in Figure 3.1 (A). The top and the bottom electrodes are made from cobalt. The thickness of the cobalt films is $100\mathring{A}$. The top and the bottom layers are $100\mathring{A}$ thick cobalt films. The width$\times$ length is $1.5mm \times 15mm$ and $1mm \times 20mm$ for the bottom and the top layer, respectively. The sample cross-section, sketched in Figure 3.1 (B), shows nanometer scale aluminum grains embedded in aluminum oxide. The magnetization of the film is in the film plane, which is evidenced by large P in our spin-valve signal described later. The electrodes are long rectangles and the easy axes is along the long direction of the rectangles. This enables the parallel and the antiparallel configurations in zero magnetic

field. Consequently, large P (averaged over the junction area) is obtained.

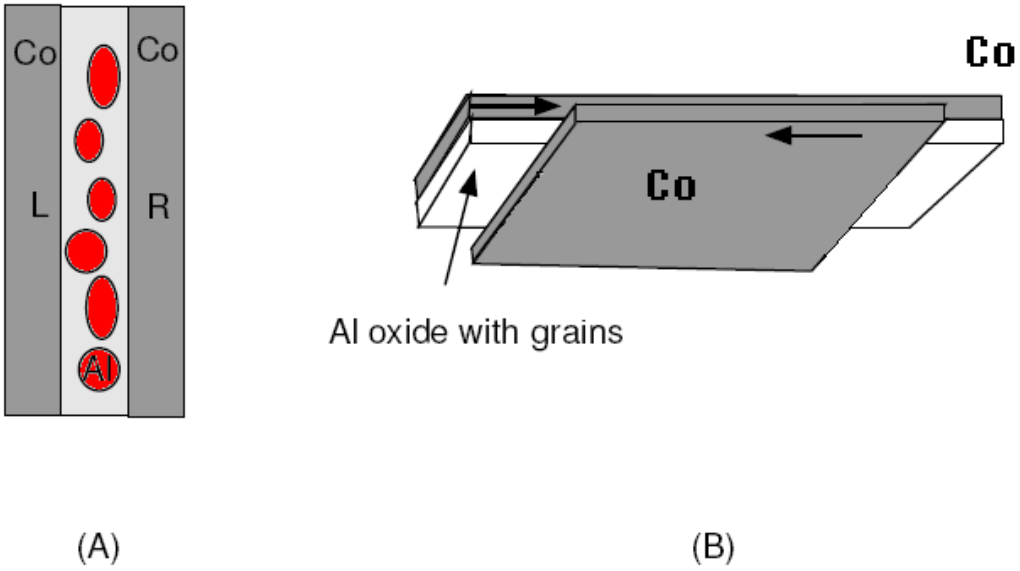

Figure 3.1: (A) Zeller-Giaver tunnelling junction with ferromagnetic leads, (B) Geometry of the tunnelling junction.

The device is fabricated in two evaporation steps. First, we thermally evaporate a cobalt film on a SiO_2 substrate, which is a silicon wafer with a thermally grown oxide on the top, through a mask at 4×10^{-7} Torr pressure. The deposition of cobalt is stopped by closing the shutter. Next, we change the metal source to aluminum and evaporate aluminum in high vacuum, while the shutter remains closed. Then we open the shutter for 1 second and close the shutter again. The deposition rate is 0.2 nm/sec. So, the cobalt layer is now covered with a seed layer of aluminum with nominal thickness 0.2 nm.

Our next deposition step is the reactive deposition of aluminum oxide. In this step, oxygen is introduced into the chamber, which exposes the cobalt surface to oxygen vapor. The oxidation of cobalt surface should be minimal, because paramagnetic impurities in cobalt-oxide could affect spin-polarized tunnelling. Our strategy to minimize oxidation of cobalt is to apply as little oxygen as possible for as little time as possible. In addition, the seed layer also provides some protection of cobalt before passivation by the deposited

aluminum oxide. The seed layer must be very thin, because if any metallic aluminum remains on the cobalt surface after oxidation, then spin-polarized tunnelling density of states will be reduced.

Immediately after closing the shutter the second time, we introduce oxygen into the deposition chamber while evaporating aluminum. The oxygen is introduced at a flow rate of 200 sccm. The chamber is continuously pumped with the cryopump gate valve fully open. Oxygen pressure increases and reaches 10^{-5} scale Torr in few seconds and stabilizes at 4×10^{-5} Torr after 30 sec. Only during these initial 30 seconds, while the pressure increases and stabilizes, cobalt surface with a 0.2 nm seed layer of aluminum is exposed to oxygen. After 30 sec, when the pressure is stabilized, we open the shutter and evaporate 5 nm of aluminum at a rate of 0.2 nm/s, to deposit the bottom aluminum-oxide film, which is 7 nm thick.

In general, the thickness of the deposited oxide at fixed aluminum evaporation rate will be an increasing function of oxygen pressure. In our case, thickness of the deposited oxide versus pressure saturates at 7 nm at approximately 1×10^{-5} Torr. Any further increase in oxygen pressure will not increase the aluminum oxide thickness. Consequently, in our deposition process nearly all aluminum atoms that are deposited at 4×10^{-5} Torr are oxidized, however, the oxygen pressure is only three times larger than the minimal oxygen pressure for the oxidation of aluminum (the saturation pressure).

The oxygen pressure of 4×10^{-5} is substantially smaller than typical oxygen pressures used to thermally oxidize aluminum surfaces in tunnelling junctions. For example, in Reference [69], nanometer sized aluminum nanoparticles were oxidized at 0.1 Torr of oxygen for $1-2$ minutes. This process created tunnelling barriers of resistance in mega ohm range, which corresponds to oxide thickness of approximately 1 nm. Since our oxygen pressure is smaller by four orders of magnitude and the oxidation time is shorter, the thickness of the surface aluminum oxide in our case must be considerably smaller than 1 nm. Thus, we expect that the seed aluminum layer of nominal thickness 0.2 nm provides some protection of cobalt surface from oxidation.

This reactive evaporation technique was used to create tunnelling junctions containing a

single metallic grain [60]. The junctions were of high quality and they displayed well resolved Coulomb-Blockade steps and discrete energy levels of the grain at low temperatures. So, the aluminum oxide in our samples is a suitable insulator for the studies of properties of metallic grains.

The sample, which is now passivated, is exposed to air and the mask is replaced. Next, the sample is evacuated to base pressure and we deposit 1.5 nm of aluminum, which creates isolated grains, as shown by the image in figure 3.2. Then we deposit another layer of aluminum oxide, by evaporating 5 nm of aluminum at rate 0.2 nm/s at 4×10^{-5} Torr of oxygen. Finally, we deposit the top cobalt layer.

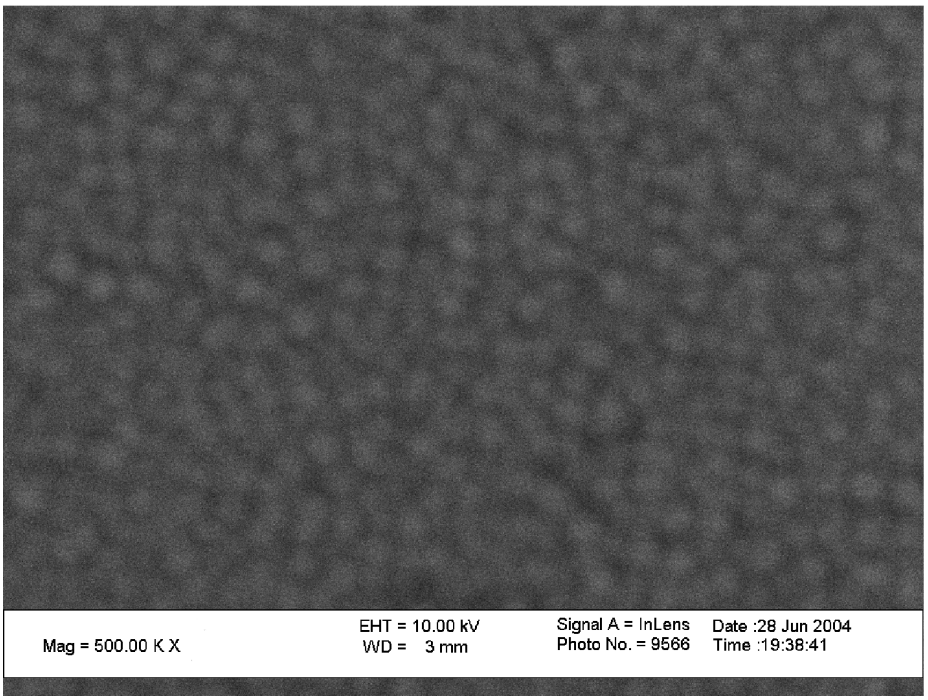

Figure 3.2: Here is the scanning electron micrograph of nanosize aluminum grains. The aluminum grains are in different sizes. The average grain diameter is $\sim$ 6 nm, and the number of grains in the junctions is estimated as $N = 2.5 \times 10^{10}$.

The average grain diameter is $\sim$ 6 nm. If we assume that the grains are hemispherical, analogous to reference [69]. We estimate that the average electron-in-a-box mean level spacing is 0.2 meV. Note that there is a relatively wide distribution of grain diameters in Figure 3.2, as some grains have coalesced. Hence, the range of level spacings in the ensemble is rather large.

In addition, the grains are exposed to oxygen vapor before deposition of the top oxide layer, at 4×10^{-5} Torr for 30 seconds. As a result, the grain surface is oxidized from above, but we expect that the oxide thickness is considerably smaller than 1 nm, as discussed above. Additionally, there is generally chemisorbed oxygen remaining on the underlying oxide surface. Consequently, the grain surface may be oxidized from below. Thus, the average size of the metallic core of the grains could be smaller than the apparent grain size because of this effect, by up to about 1 nm.

The number of grains in the junctions is $N = 2.5 \times 10^{10}$. Although the junctions are very large, the resistance of the junctions (R) varies significantly among samples made at the same time. R is in the range $1k\Omega < R < 10M\Omega$. We also make tunnelling junctions as described above but without aluminum grains and find these devices to be insulating. In addition, we make control samples without aluminum grains and with the aluminum-oxide layers at half the thicknesses from those above. If we fabricate 24 junctions at the same time, the resistance of the junctions may vary within a factor of 100 among different samples. The control sample resistance is in the same range ($1k\Omega < R < 10M\Omega$),which shows that tunnelling in the devices with grains take place via the grains. The junctions age in air, and we find that the samples must be cooled down to liquid nitrogen (or below) within 24 hours.

The fluctuations in sample resistance among samples made at the same time show that the tunnel current must be dominated by the current flow through weak spots. Consequently, the number of grains that are active in transport is $\ll N$. The weak spots may result from thickness variations in the oxide layer across the junction area or from defects in the oxide, or from both. Also the samples are extremely sensitive to electrostatic discharge, and they must be very carefully treated.

We measured the surface roughness of a single aluminum oxide film deposited over SiO_2 by the atomic force microscope and found that it was $\sim$ nm. This surface roughness can cause weak spots in the tunnelling barrier, because the tunnel resistance decay length in oxides (0.1 nm) is much smaller than the surface roughness.

In addition, it is known that amorphous aluminum oxide has coordination number defects, which may be caused by oxygen vacancies [70]. These defects could give rise to hole traps near the valence band edge, which could result in weak spots for tunnelling. These oxygen vacancies could be paramagnetic, which could affect spin-polarized tunnelling.

3.2 Sample Testing and Mounting

The measurements of the devices are carried out in two step: the first step is to pre-select the good samples, and the second one is cooling down the good samples.

First, we select our samples at room temperature. The bias voltage are supplied through a voltage divider box. The output voltage is set using a toggle switch to select the proper resistor for the voltage divider and in that way a voltage of order of mV is applied. We use a DC voltage source. The bias voltage is 10 mV and is applied through the tunnelling junctions.

We use a probe circuit measurement to measure resistance between each pair of electrodes. The schematic of the circuit is shown in Figure 3.3. We can observe that 2 voltage dividers are used to apply voltage between the two ends of the sample. The applied bias voltage is set to $10mV$ to avoid blowing our samples. The current is measured by a low noise Ithaco 1211 current amplifier that is set in serial with the circuit. We use a micro manipulator to make contact in the contact pads of our samples. The resistance is in the range from $1k\Omega$ to $10M\Omega$ (open circuit see in Figure 3.3).

After testing our samples, we proceed to mount those good samples on a sample holder that is designed to facilitate the electrical connection.

A schematic of a sample holder is shown in Figure 3.4. The sample holder is made of a printed circuit board which was etched in ferric acid for about 15 minutes. The dimensions of the sample holder are approximately 9 mm wide and 15 mm long. A 4-pin Microtech female connector is soldered to the small piece of board. The pins are distributed as follows: 1 pin for V^+, 1 pin for V^-. Then a four pin sample holder can be loaded with two samples.

To connect the contact pads of our sample to the point contact in our sample holder, we use thin non-insulated wires. To connect this wire with the contact pads, we use indium

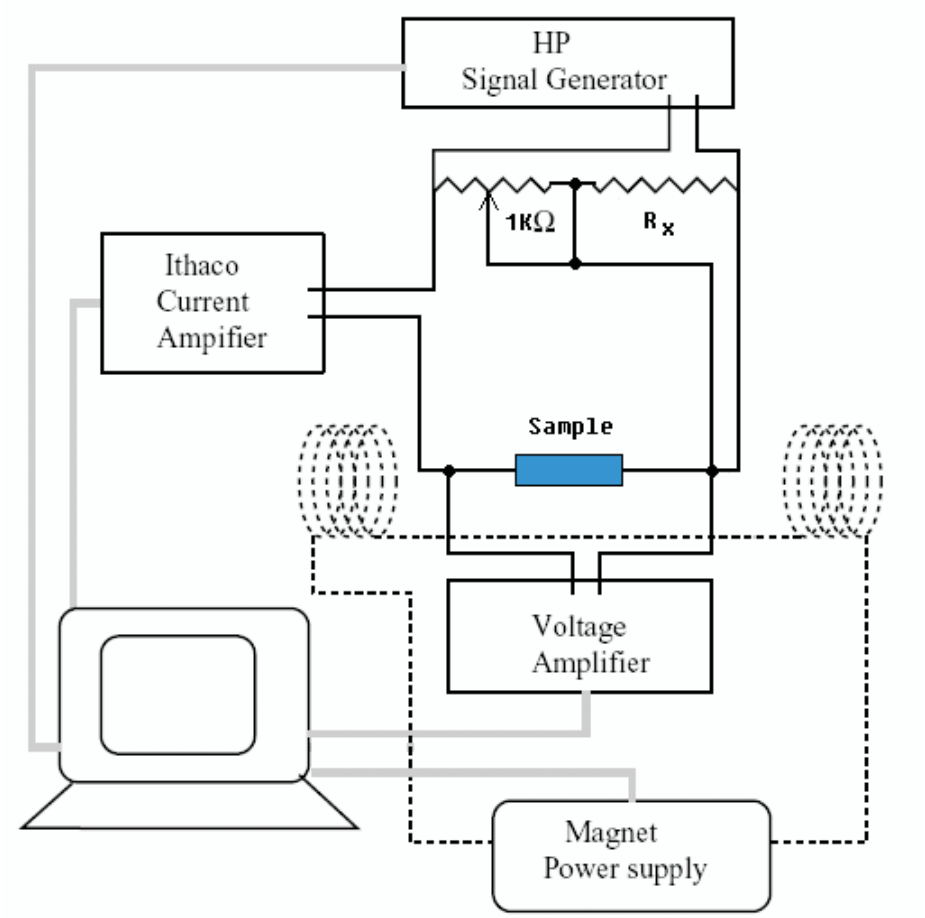

Figure 3.3: Schematic of electrical measurement circuit: black lines indicate electrical connections. Dashed lines indicate the superconductor solenoid that provide the magnetic field, whereas grey lines indicate lines of communication between the data-acquisition computer and various equipments.

dots pressed with a small allen tool. Because indium is very malleable, it is easy to press against the contact pad. After pressing, the indium dot sticks to the contact and the wire is in between.

As mentioned earlier, the samples are extremely sensitive to electrostatic discharge, so it is crucial that one grounds oneself with a grounding strap, and the sample holder's terminals are shorted to each other. This ensures that some voltage is not accidently applied across the device. Once the samples are loaded onto a dipstick, we need to test our samples to verify that they do not blow them. Then the samples are pre-cooled to liquid nitrogen temperature. As soon as the boiling stops, the dipstick can be inserted into a helium dewar; this cools the samples immediately to 4 K. Once the samples have cooled they can

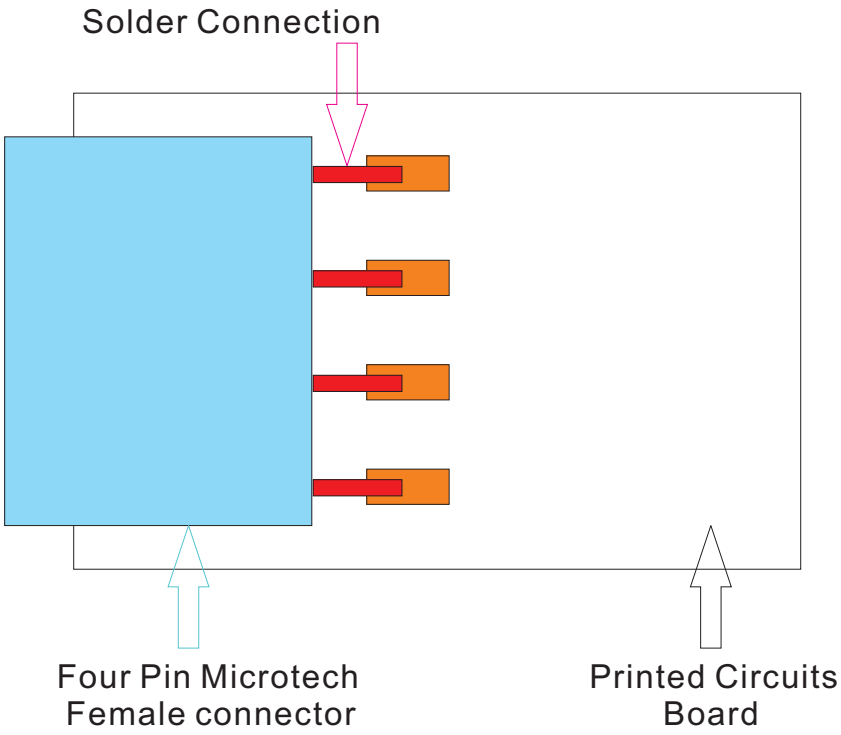

Figure 3.4: The Structure of Sample holder

be connected into the circuit using the make-before-break switch. The computer acquisition program will acquire an IV curve as the bias is swept at a frequency 10 mHz. It is also useful to look at the current through the device on an oscilloscope since bad devices can be detected quickly. This category of good devices is closely related to the devices of the resistive kind. In this case the blockade is smooth and the IV curve lacks sharp features. This occurs mostly due to multiple particles in parallel connecting the two electrodes.

3.3 Noise Reduction

The following sources of noise should be checked before connecting the samples to the external circuit.

Ground loops are a prominent source of noise and are caused by the presence of two grounds in the circuit. The best way to check for them is by looking over the circuit and ensuring that the only ground that you use to connect to the outer shields of a coaxial, or a triaxial, cable is the one connected to the sample holder's support structure,and that it

is the only ground used in the measurement setup.

§ 1. Amplifiers and the voltage generators

The amplifiers used in the measurement have internal batteries, and I strongly recommend using this feature since connecting them to the mains causes the output to be more noisy. The signal generators used should be floating, and this can be checked by using an ohmmeter; if they are not floating, then one is sure to run into problems with the ground loops. One way to make doubly sure that there are no ground loops is to connect the signal generators to the mains via isolation transformers.

§ 2. Bad cables

Bad triaxial cables can create extra noise in the system by inadequately shielding the cables. This should be the last resort in terms of minimizing the noise and requires replacing the cables one at a time to find the bad one. Once the noise is reduced to a level of 0.5 pA the setup is ready for acquisition. Note that the sources of noise that have been addressed above are mainly due to the external circuit. However, there is always the high frequency noise that travels from the equipment down to the samples. Once the noise in the circuit is minimized, the samples can be measured.

CHAPTER IV

EXPERIMENTAL RESULTS

As mentioned in Chapter 3, the MTJs could be used to probe a variety of physical phenomena. We use a probe circuit measurement (Figure 3.3) to measure the current and sweep the driving voltage between each pair of electrodes. This measurements display the I-V characteristic curve of metallic grains embedded in MTJs, and this allowed us to probe the charging properties and the spin polarization of the ferromagnet when a magnetic field was applied for the samples.

4.1 IV-Curves at 4.2K

We present three Samples with aluminum grains. Figure 4.1 displays the IV-curve of sample 1 at 4.2 K. The other two samples have similar IV-curves. The conductance is suppressed at zero bias voltage, as expected from Coulomb-Blockade on aluminum grains, consistent with reference [68].

The average charging energy E_C is obtained by extrapolating the linear part of the IV-curve at high voltage (V) to zero current (I) and finding the offset voltage, as indicated. We averaged the Coulomb Staircase IV-curve [71] over the background charge, capacitance ratios, and over capacitance range $(C/4, 7C/4)$, where C is the total capacitance of a grain. The corresponding offset was $1.3E_C/e$, where $E_C = e^2/2C$. E_C is 4.3 meV in samples 1 and 2, and 6 meV in sample 3.

We also made tunneling junctions without aluminum grains, but with the aluminum oxide at half the thickness using the same procedure as described in the section 3.1. The data for IV curves (with aluminum grains) and (without aluminum grains) are shown in the Figure 4.1 (A) and (B). These samples do not exhibit any significant conductance suppression at $V = 0$, so Coulomb-blockade like behavior in our samples is caused by aluminum grains.

In an ensemble, there are particles with different diameters. At low bias voltage ($<< k_BT/e$), most of the current is carried through the largest particles, because they have the smallest charging energy. Smaller particles contribute less here because the current through them is blocked by the Coulomb blockade for a wide range of the background charge. As the bias voltage increases, the relative contribution to the current from smaller particles increases. Consequently, the contribution to TMR from smaller particles increases with voltage.

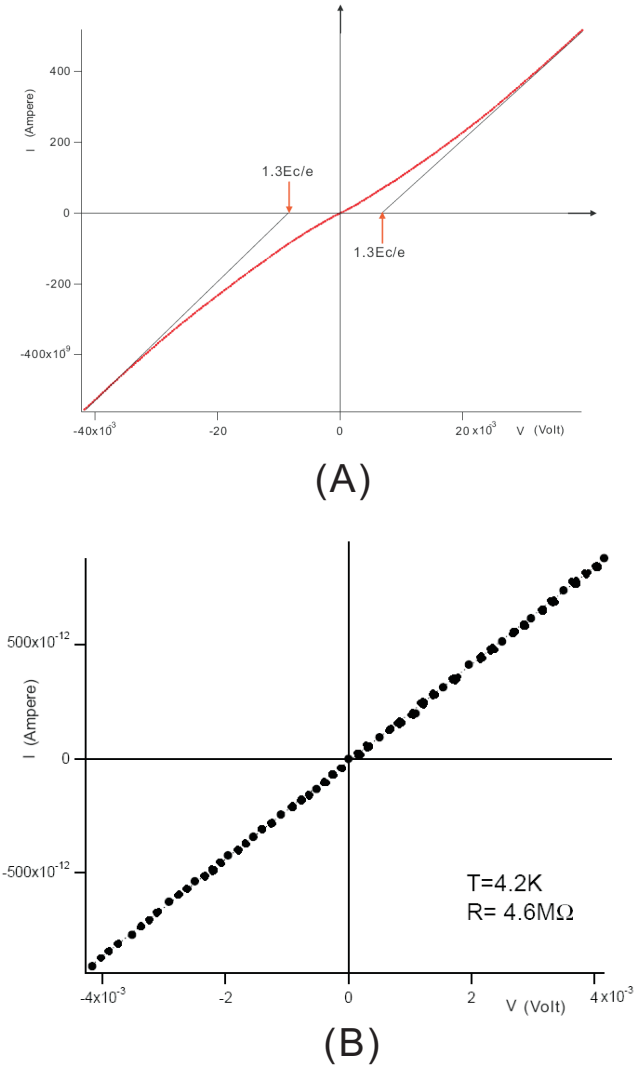

Figure 4.1: (A) The I (current) vs. V (voltage) curve of Sample 1 (with aluminum grains), the corresponding offset is $1.3E_C/e$, where C is the average capacitance of the grains.(B) The IV curve data, and dash line is the linear curve fit for the data of sample (without aluminum grains).

4.2 Spin-Valve Effect

Figures 4.2 (A), (B), and (C) display current versus magnetic field in samples 1, 2, and 3 respectively, at constant bias voltage. All samples exhibit TMR, which demonstrates that the tunnelling current is spin-polarized. Samples 1 and 3 exhibit a spin-valve effect: at a large negative field, the magnetizations of the cobalt reservoirs are down. If the field increases, the magnetization of one cobalt reservoir switches direction, and the tunnelling current drops abruptly from $I_{\uparrow\downarrow}$ to $I\uparrow\downarrow$. Finally, at a larger positive field the current jumps back up to $I_{\uparrow\uparrow} \approx I\uparrow\downarrow$. In sample 2, pinning of the magnetization of Co layer prevents spin valve effects.

4.3 Bias Voltage Dependence of TMR

In addition to these abrupt transitions in TMR, we find that TMR varies continuously with the magnetic field and it fully saturates in the applied field of $\sim 1T$. The cobalt films are generally multi-domain, and the average domain size in cobalt films is of the order of 1 micron [72]. If many domains were involved in providing the TMR signal, one would expect the resistance transitions to be gradual due to the spread in coercive fields from domain to domain. Thus, only a portion of the sample of order domain size or less is responsible for the abrupt TMR transitions. This behavior is in agreement with the finding that the tunnelling current is dominated by weak spots.

In sample 2, there is only one jump near zero field, followed by a broad TMR background that saturates at $B \sim 1T$, which shows that only one cobalt electrode exhibits an abrupt transition with magnetic field. The abruptness of the transition indicates again that this sample is sensitive to a very small fraction of the physical device. However, in contrast to samples 1 and 3, the magnetic behavior of cobalt on one side of the effective contact area indicates the presence of a very persistent magnetic defect, which for example could be a 360 degree domain wall [73].

Although our junctions are not ideal, we still can learn about the physics of spin-polarized tunneling through grains by studying how the abrupt resistance transitions depend on bias voltage and the perpendicular applied magnetic field. TMR corresponding to these

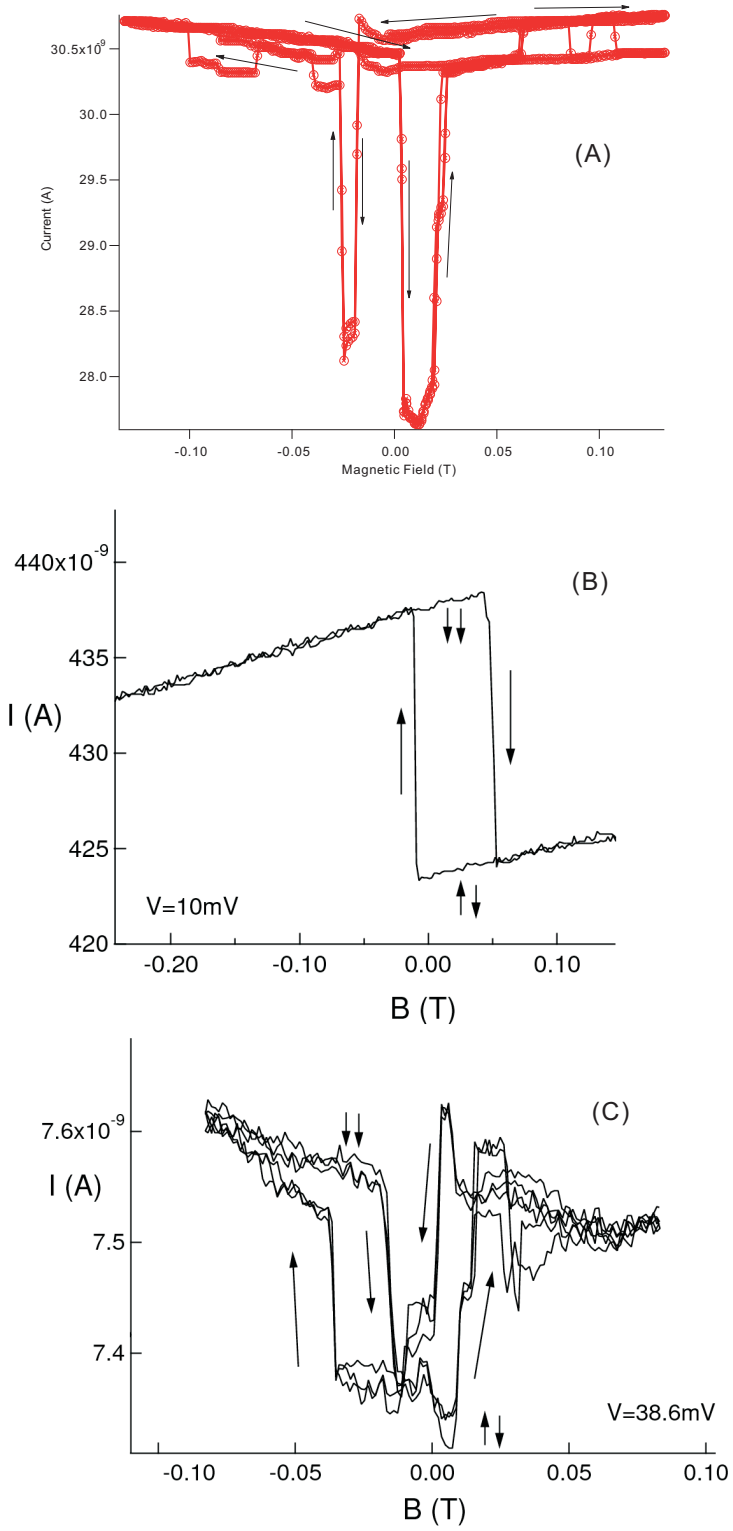

Figure 4.2: A, B, and C: I (Current) versus B (parallel applied magnetic field) at 4.2K, in samples 1, 2, and 3, respectively.

transitions is a measure of the spin-polarization of the current. The number of particles that contribute to the abrupt transitions is very small. It is certainly smaller than the number of particles that fit under a micron scale domain in cobalt (roughly 10^4). The abrupt TMR transitions are reproducible when the magnetic field cycle is repeated, as seen in Figure 4.2. For the Hanle effect studies, we select devices that exhibit spin-valve effect.

The tunnelling magneto resistance is calculated as equation 2.3, where the current values were taken immediately before and after the resistance transitions. Figure 4.3 (A) and (B) display differential conductance G with bias voltage in samples 1 and 2, respectively. G is measured by the lock-in technique. As the bias voltage is varied slowly at 3 mv/hr, the magnetic field is swept between -0.25 T and 0.25 T at 0.01 Hz. The differential conductance switches between $G(P)$ and $G(AP)$ when the magnetizations switch alignment.

$G(P) - G(AP)$ changes significantly when the bias voltage varies in a narrow interval around zero-bias voltage. In sample 2, the asymmetry in $G(P) - G(AP)$ is dramatic: conductance is spin-unpolarized at negative bias and significantly spin-polarized at positive bias. TMR also changes significantly around zero bias voltage, as shown in Figure 4.3 (C) and (D). Circles represent TMR from equation 2.3, and squares are obtained as $TMR = \int G_P(V)dV / \int G_{AP}(V)dV - 1$.

TMR values in our devices are less than 10 %. In the state of the art magnetic tunneling junctions, TMR exceeds 40 % at room temperature and it is critically dependent upon the fabrication process and annealing of the tunneling junctions [74]. As discussed before, tunneling in our samples is dominated by weak spots caused by the surface roughness and oxygen vacancies. The junctions are not ideal and thus the TMR is reduced.

Our sample's TMR versus V is shown in Figure 4.3. At positive bias voltage (V), where TMR is large, TMR is weakly dependent on bias voltage in interval 0.5 mV $<$ V $<$ 3 mV. At larger voltage, TMR begins to decrease rapidly with voltage. At voltage $\approx$ 10 mV, the decrease in TMR with bias voltage slows down. At very large bias voltage, TMR is significantly reduced but not fully quenched to zero.

At negative bias voltage (V), where TMR is small, TMR is weakly dependent of voltage in interval -3 mV $<$ V $<$ -0.5 mV. But, in sample 2, where TMR is fully quenched at $V =$

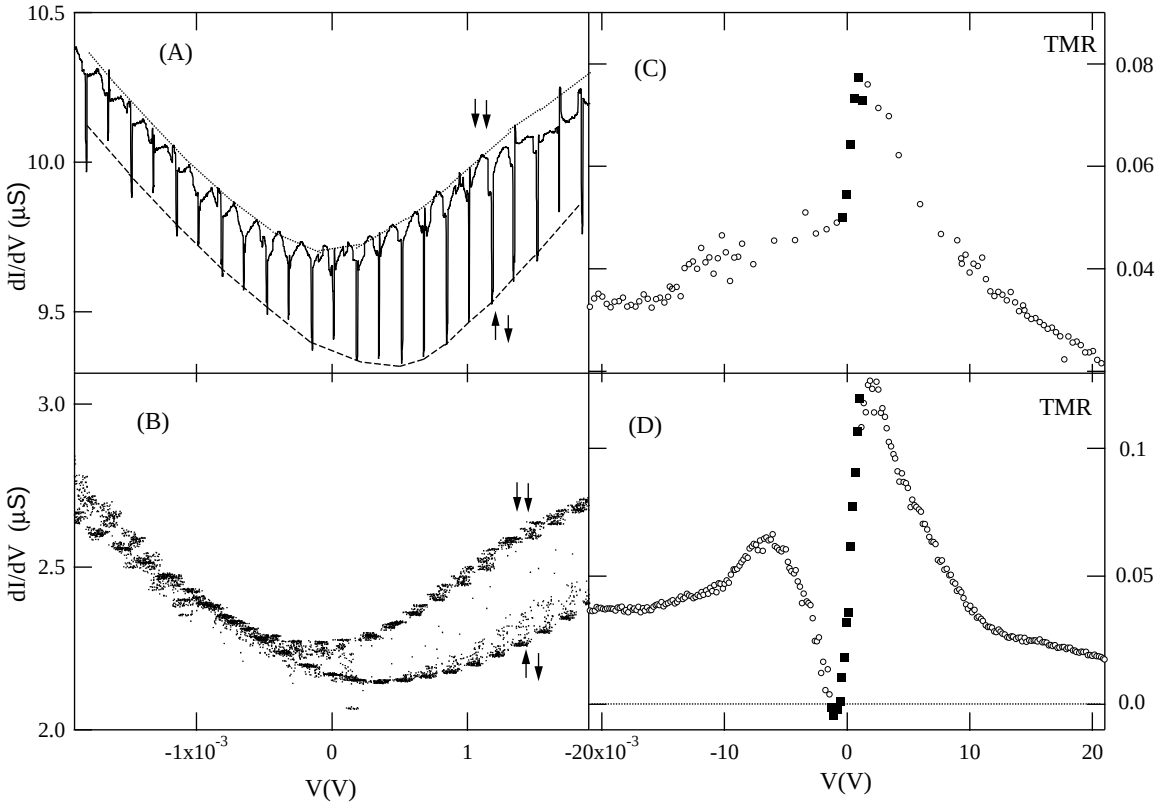

Figure 4.3: A and B: Differential conductance versus bias voltage in samples 1 and 2, respectively. The data display differential conductance G with bias voltage in samples 1 and 2, respectively. G is measured by the lock-in technique. As the bias voltage is varied slowly at 3 mv/hr, the magnetic field is swept between -0.25 T and 0.25 T at 0.01 Hz. The differential conductance switches between $G(P)$ and $G(AP)$ when the magnetizations switch alignment. C and D: TMR versus bias voltage in samples 1 and 2, respectively. Circles represent TMR from equation 2.3, and squares are obtained as $TMR = \int G_P(V)dV / \int G_{AP}(V)dV - 1$.

-0.5 mV, there is a maximum in TMR at around mV. In sample 1, where TMR is not fully quenched at V = -0.5 mV, there is a much weaker maximum around a similar voltage.

Note that we assume that the level spacing is $< k_B T$, so the transitions between the energy levels can be thermally driven. If the level-spacing is $> k_B T$, this relaxation mechanism is suppressed and T_1 is enhanced.

At finite bias voltage, we assume that the energy relaxation rate is larger than the escape rate, so that the distribution of electrons in the grain is in equilibrium (the basis of this assumption is as follows: TMR decrease with V suggests that $\tau_D > T_1$; since we expect $T_1 \gg \tau_{e-ph}$, it follows that $T_1 \gg \tau_{e-ph}$, so electrons are in equilibrium).

In the antiparallel state, electron spins accumulate in the grains by transport, which creates a difference PeV between the Fermi levels of spin up and spin down electrons, as shown in figure 4.3 (A) and (B). However, if T_1 is shorter than the dwell time, then spin-up electrons in energy window $E_F \pm PeV/2$ can undergo a transition into one of the unoccupied spin-down states at lower energies, as sketched by the arrow. TMR decreases with voltage because T_1 decreases with bias voltage , since electron-phonon transition time τ_{e-ph} decreases with bias voltage (V). This qualitatively explains TMR versus V at $V > 0$.

In this picture, TMR begins to decrease with voltage roughly when the spin-imbalance PeV becomes comparable to k_BT, that is, when $V \approx k_BT/(Pe) \sim 1.5mV$, in agreement with the data.

At $V \sim 10mV$, the decrease in TMR with voltage slows down, and TMR is not fully quenched at very large bias voltage. In addition, TMR has a maximum at $\sim -10mV$. We suggest that these effects are caused by electron transport through small grains, in which $k_BT < \delta^s$ (s refers to small grains).

Near zero bias voltage ($V \sim k_BT/e$) only a very small fraction ($\sim k_BT/E_C^s$) of small grains are conducting (because of Coulomb-blockade), so TMR is dominated by electron transport through larger grains. Spin relaxation is fast in large grains, as discussed before, and it leads to asymmetric TMR. Spin-relaxation is suppressed in small grains, so small grains have large and symmetric TMR, but, their contribution to total TMR is reduced because of the Coulomb-blockade.

At a large positive or negative bias, $V = \pm\delta^s/eP \approx 5\delta^s/e$, the fraction of conducting small grains increases to $eV/E_C^s \approx 5\delta^s/E_C^s$, which is on the order of 1. At this voltage, small grains still do not exhibit spin relaxation, because there would be only one energy level in energy window PeV in Figure 4.4, so these grains have large and symmetric TMR at this bias voltage. Thus, TMR of the junction is enhanced at this voltage, which explains the slow down and the maximum at positive and negative voltages, respectively. With further increase in voltage, TMR of small grains begins to decrease, because the energy window PeV becomes $> \delta^s$.

We explain the asymmetry in TMR by spin-relaxation in aluminum grains and the

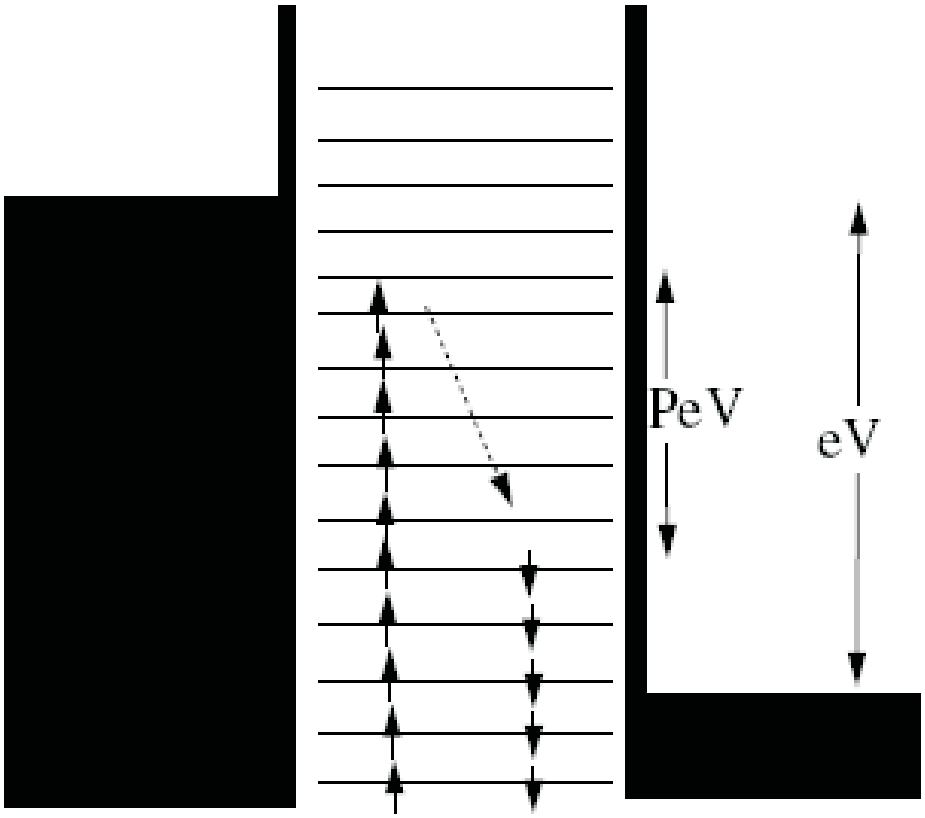

Figure 4.4: Sketch of the grain electronic configuration at bias voltage V. The arrow indicates electron-phonon induced transition with spin-flip.

asymmetry between the resistance between the grains and the two reservoirs. Asymmetric resistances are easily introduced by sample fabrication. For example, exposure of the bottom aluminum oxide layer to air increases the oxide thickness by hydration.

At large magnitude of bias voltage, TMR has a complex dependence on the magnitude of bias voltage. It is difficult to explain the origin of this dependence, but we speculate that energy dependence of the spin relaxation time, single electron charging effects, and the distribution of energy level spacings in the ensemble of grains may play important roles.

4.4 TMR Hanle Effect

Here we discuss the effects of spin precession in the applied magnetic field B_n applied perpendicular to the film (the Hanle effect). Figure 4.5 (A) displays the resulting peak in current versus B_n, for sample 3 in the antiparallel configuration (in zero applied parallel

field). The dependence is reversible when B_n is swept up and down, which shows that the curve does not arise from the hysteresis loop in the leads. The peak amplitude is close to $(I_{\uparrow\uparrow} - I_{\uparrow\downarrow})/2$.

The characteristic field B_C, defined as half-width of the peak, is 8 mT. We find that BC is symmetric with bias voltage, which shows that BC is independent of the dwell time. So, the processes that contribute to the Hanle effect half-width are different from the processes responsible for the TMR asymmetry.

The Hanle effect in a quantum dot had been calculated by Braun, et al [67]. The calculation shows that perpendicular field induces Larmour precession of the injected spin, which reduces spin polarization of the current. Current versus B_n exhibits a Lorentzian peak of amplitude $(I_{\uparrow\uparrow} - I_{\uparrow\downarrow})/2$ (in agreement with our data) centered at $B_n = 0$. If a constant large parallel magnetic field B is present, then the peak width becomes B and the Hanle effect half-width is symmetric with bias voltage.

Our observations Figure 4.3 (C) can be explained by these theoretical results, if in zero applied field there exist a local magnetic field B_C acting on the grains. This local field induces spin precession in zero applied magnetic field, and the spin-coherence time is the Larmour period in the local field: $T_2^* \sim h/\mu_B B \sim ns$.

The local field could be caused by the surface roughness, which generates a finite dipole field originating from cobalt. Note that the top aluminum-oxide/cobalt interface in Figure 4.5 is irregular because of the underlying aluminum grains. The local field of 8 mT is certainly possible because the internal field in cobalt is 2 T. The hyperfine field from the nuclei can also create an effective field of order mT that causes dephasing [75]. In our junctions, tunnelling is dominated by weak spots. Consequently, the local magnetic field will fluctuate among samples, explaining the difference in B_C between the samples.

It might be surprising that electron transport is spin-coherent with such a short dephasing time. In this experiment, TMR survives dephasing because of the conservation of the spin-component along the local field direction. Even if the electron dwell time is much longer than the dephasing time, TMR will be finite. This is sketched in Figure 4.5 (B. If the magnetizations switch from a parallel to antiparallel state at finite bias voltage, then

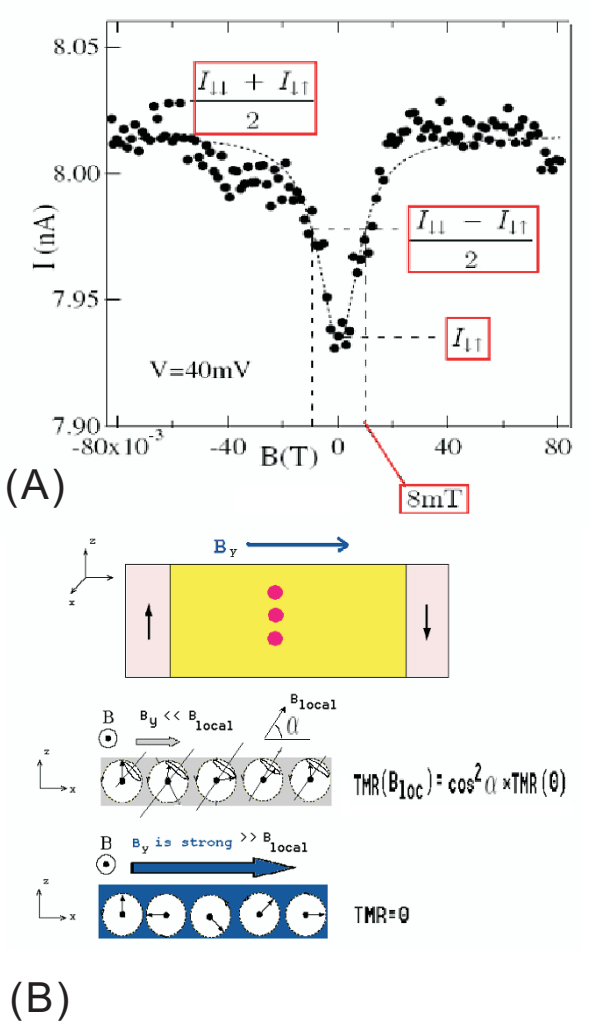

Figure 4.5: A. Current versus perpendicular field in sample 3. B. Sketch of the effects of the local field on TMR. The component of the injected spin along the local field direction gives rise to a finite TMR, even if $T_2^\star$ is much shorter than the dwell time.

the injected spin component along the local field direction switches from zero to finite value, giving rise to a finite TMR. The perpendicular component of the injected spin is averaged to zero, which reduces the TMR by a factor of $cos^2(\alpha)$, where α is the angle between the magnetization and the local field.

CHAPTER V

DISCUSSION AND SUMMARY

We investigated spin-polarized current through ensembles of nm-scale aluminum grains. The spin-coherence time is obtained from the Hanle effect measurement: $T_2^\star \sim ns$; for the first time in metallic grains (quantum dots). Fast dephasing is attributed to spin-precession in the local magnetic field. Tunnelling magneto resistance is asymmetric with current direction, and TMR has bias voltage dependence, which is attributed to spin relaxation.

5.1 Voltage Dependence on TMR

Our results showed the magnitude of the TMR decreases strongly with increasing bias voltage. One may explain the drop in TMR by the inelastic scattering of magnon excitations [76]. Since more magnons can be emitted with increasing bias voltage, this result in the reduced TMR values. However, this magnon excitations explanation may be useful in interpreting the softening of the TMR with bias about 200 mV. In our cases, the sample's TMR versus bias voltage is shown that TMR reduced rapidly within 3 mV (see figure 4.3). Also most of our samples showed strong asymmetric TMR with current direction dependence. Thus, this bias voltage dependence in TMR should be dominated by the mechanisms other than magnon excitations.

Another mechanism that may contribute to the voltage dependence of the conductance and TMR is related to the electronic structure of the ferromagnets. When a bias voltage is applied between the MTJ electrodes, this leads to the change of electronic structure of ferromagnets as a function of energy. Due to this change, the conductance or TMR should be energy dependent. This change should obviously be sensitive to the type of ferromagnet. But our results show a strong voltage-dependence in a range much small than the range for band structure effects.

One possible explanation is that the voltage drop in TMR is due to localized trap states

in the amorphous barrier or the impurity-assisted contribution. But our aluminum oxide is not defective. It is an extremely good insulator in our junctions, because junctions without aluminum nanoparticles and the same oxide thickness have immeasurably high resistance. Hence, we are certain that tunneling in our devices is a two-step process via the aluminum grains. It is well known that pure aluminum oxide does not have free electron spins. The only impurity spins may come from cobalt surfaces. However, our bottom cobalt layer is first covered with a 2 $\mathring{A}$ seed layer of aluminum in high vacuum. This aluminum film is then oxidized from the top at $\sim 3 \times 10^{-5}$ torr of oxygen, and then the additional oxide is grown on top by reactive evaporation without breaking the vacuum. Thus, the bottom cobalt layer surface is never exposed to oxygen, and it is protected when exposed to air. Also our large TMR is the evidence that spin relaxation by impurity spins in the oxide must be weak. One can argue that perhaps the top cobalt layer has surface impurity spins. But the top layer is deposited over pure aluminum oxide surface, which was not exposed to air. It is hard to imagine that the oxygen would remove itself from Al_2O_3 and attach to cobalt to create impurity spins.

So far, we have given the plausible arguments that there are no impurity spins. To clear the issue, now we prove that there are no impurity spins in the oxide. We have made tunneling junctions without aluminum nanoparticles, but with the aluminum oxide at half the thickness using the same procedure as described in Chapter 3, section 3.1. The data for I versus V and TMR versus V are shown in the figure 4.1. These samples do not exhibit any significant conductance suppression at $V = 0$, so the Coulomb-blockade-like behavior in our samples is caused by aluminum grains. More importantly, TMR is symmetric and independent of V in this small voltage range. This proves that there are no impurity surface spins in the barrier. We can conclude that asymmetric TMR and the bias voltage-dependence is therefore caused by the the aluminum grains. This means that the Voltage-dependence is caused by the processes inside the grains.

This TMR bias voltage dependence can be explained by a fast decrease in T_1 with voltage. This would be the case if spin-relaxation is caused by the electron-phonon energy relaxation in the presence of spin-orbit interaction, because electron-phonon relaxation time

τ_{e-ph} decreases with voltage. This spin-relaxation mechanism is well known in bulk metals, where $T1 = \tau_{e-ph}/\alpha$ (Elliot-Yafet relation), and α is the scattering ratio (10^{-4} in aluminum) [77].

The spin-conserving energy-relaxation in aluminum grains takes place by phonon emission with the relaxation rate [3].

$$\frac{1}{\tau_{e-ph}(\omega)} = \left(\frac{2}{3}E_F\right)^2 \frac{\omega^3 \tau_e \delta}{2\rho\hbar^5 v_S^5}, \tag{5.1}$$

Where $E_F = 11.7eV$ is the Fermi energy, ω is the energy difference between the initial and the final state, $\rho = 2.7g/cm^3$ is the ion-mass density, $v_s = 6420m/s$ is the sound velocity, and τ_e is the elastic scattering time. At zero bias voltage, typical excitation energy at 4.2 K is around $3.5k_BT = 1.3meV$. Equation 5.1 gives the average transition time $\tau_{e-ph}(1.3meV) = 60ns$ between the excited states at 4.2 K. So, T_1 is longer than 60 ns. If we assume that the Elliot-Yafet relation is valid in grains, we can estimate $T_1 = 60ns/\alpha \sim ms$, which is comparable to T_1 in GaAs quantum dots.

5.2 Asymmetric TMR

Another significant phenomenon is that we found a strong asymmetric TMR in our tunnelling juntions with grain (see figure 4.3 (C) and (D)). The TMR (the tunnelling junction without grain) are symmetric and independent of V at same bias voltage range (see figure 5.1). Therefore we can conclude that asymmetric TMR and the bias voltage-dependence are caused by the aluminum grains.

In non-ideal magnetic tunnelling junctions, TMR can be strongly asymmetric and bias voltage dependent [78, 79, 80, 81]. The asymmetry has been explained by the two-step tunnelling via localized states. In our control samples (without grains), TMR is found to be symmetric and weakly dependent on voltage (see Figure 5.1). This shows that the localized states responsible for asymmetric TMR in junctions with grains are the electronic states in the grains.

We explain this asymmetry in TMR by the asymmetry between the average resistances between the grains and the two reservoirs (in Figure 2.8). Asymmetric resistances are easily

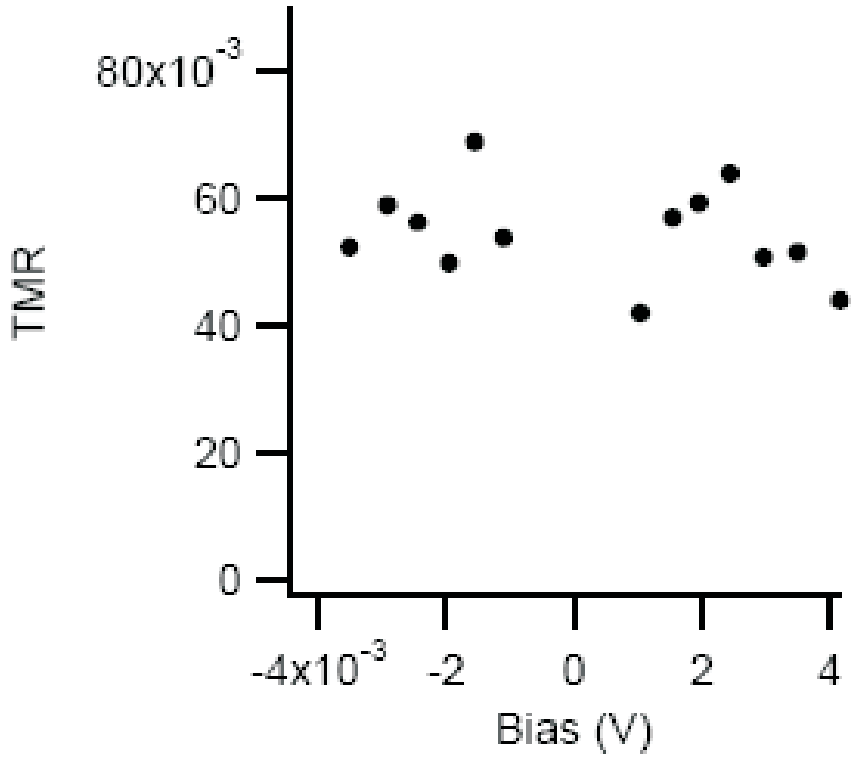

Figure 5.1: TMR versus bias voltage without Al Grains.

introduced by sample fabrication. For example, exposure of the bottom Al_2O_3 layer to air increases the Al_2O_3 thickness by hydration.

The average dwell time is $\tau_D \sim \frac{R_D}{R_Q}\frac{h}{\delta}$, where R_D is the average resistance between the grains and the drain reservoir, and $R_Q = 26k\Omega$. When the bias voltage changes sign, the drain reservoir changes, so τ_D also changes.

Asymmetric TMR occurs when the spin-relaxation time T_1 is smaller than the longer dwell time. For example, sample 2, figure 4.3 (B), suggests that T_1 is much smaller than the dwell time at negative bias, and T_1 is comparable to or longer than the dwell time at positive bias. The voltage interval around zero bias where the dwell times change is given by the Coulomb blockade thermal width $7k_BT/e$, in agreement with Figure 4.3 (A) and (B).

5.3 Summary

In this chapter, we analyzed spin-polarized current through MTJs embedded with ensembles of nm-scale aluminum grains. The main result is that tunnelling magneto resistance is asymmetric with current direction. The finding is significant because our spintronics devices have a similar behavior as the conventional diodes (resistance is dependent on current's direction). The difference is: our MTJs current carries spin state information, whereas the current though diodes carries electron information. This kind of device is a good complementarity for Spintronics community.

Finally, we have carefully discussed the several possible explanations and mechanisms for this voltage dependence phenomenon. The tunnelling magneto resistance has a complex voltage dependence, which we mainly attribute to the asymmetry in electron dwell times and spin-relaxation that we directly measured the spin-coherence time T_2^* that was found to be $\sim ns$. We suggested that the dephasing process in grains is attributed to spin-precession in the local fringing fields. Tunnelling magneto resistance survives dephasing because of the conservation of spin-component along the local field direction. Even if the electron dwell time is much longer than the dephasing time, TMR will be finite. Our observation is confirmed by the theoretical calculation of Hanle effect in a quantum dot by Braun, et al. [67].

CHAPTER VI

MOTIVATION AND INTRODUCTION

In this chapter, we present our motivation of the second component of this thesis, and describe the typical behaviors in relaxor ferroelectrics materials. Then, we discuss the Debye relaxation (simplest dielectric relaxation) with bistable model; next, we discuss about the dielectric relaxation with multi-relaxation time. All those context are essential to understand the behaviors of relaxor ferroelectric dielectric relaxation.

6.1 Our Motivation

Ferroelectricity is a dynamic area of both pure and applied research. Due to some recent developments in nanotechnology, discoveries of fundamental new physics, and societal demand for data handling and storage, there has been a renaissance in the realm of ferroelectrics. The purpose of this component is to understand the dielectric behaviors in those small nanoparticles and to discover their possible applications based on their peculiar behaviors at nanometer scale.

Recently the ferroelectric materials have been widely used in nanostructure device, and investigated extensively in the nanoscale ferroelectrics community. The relaxor ferroelectrics [82] are a special class of disordered crystals, with peculiar structure and properties, and were discovered almost 50 years ago among the complex oxides with perovskite structure. Today, the relaxor ferroelectric crystals are widely used in a variety of applications including transducers, capacitors, and non-volatile data storage elements. Some applications are based on very high dielectric constants of multi-crystalline ferroelectric samples.

In general, when the dimensions of the device approach dimensions associated with a characteristic length scale of the material of a given composition, the changes in properties of a ferroelectric material will be seen. Hence, it is very important to choose the appropriate parameters such as the nanoparticle size, film thickness for the industrial manufacture. All

those generated the need for an essential understanding for the recent rapid development of nanoscale ferroelectric structures that are keeping to reduce dimensions.

Most recently, the $Ba_{1-x}Sr_xTiO_3$ (BST) and $BaTiO_3$ (BTA) systems have received much attention due to their promising dielectric properties when used as thin film [83, 84, 85, 86, 87], and nano wire [88, 89].

The possible BST applications include the future generation of ultra-large-scale integrated dynamic random access memories (ULSI DRAMs) [4, 5, 6] and infrared detectors and filters [90]. With voltage tunable dielectric behavior, i.e., percent change in dielectric permittivity, ω_r, with DC bias, has been used for components such as phase-shifters (in phased-array antennas for radar) and preselect filters (in receivers for communication and radar) [91].

Investigation of size effects in ferroelectric materials could allow control and improvement of the ferroelectric effects by varying the grain size, rather than the chemical composition. Much of the recent development is focused on understanding fatigue and degradation, improvement of polarization retention, the switching speed, and the exploration of the finite size effects. The finite size effects are important when they are investigated in the nanoscale regime.

Many measurements are made in a wide range of frequencies and temperatures, and for many types of impurity-induced relaxor ferroelectrics (such as BST, BCT) [92, 93, 94, 95, 96, 97]. The measurements display the temperature and frequency dependence of the complex permittivity ($\epsilon^* = \varepsilon' - i\varepsilon''$) for thin films and bulk. Most experimental observations on bulk relaxor ferroelectrics are interpreted in terms of phenomenological models based on a very broad spectral distribution of relaxation times.

The theories of BST bulk dielectric and ferroelectric properties are well developed [98, 99]. But nanometer scale particles of these compounds are not well understood and they exhibit variation in their polarization behavior with particle size [100, 101, 102, 103], electric field, and temperature [93]. Electric properties of these nanometer scale particles are of fundamental interest for the physics of such dimensionally constrained microstructures. In addition, an understanding of their dielectric relaxation behaviors and ferroelectric

properties is essential before they may be successfully integrated into commercial devices.

In the second component of this thesis, we will focus on investigating the physical properties of nanoparticles that is the similar compositions of bulk BST material. First, we will try to study size dependence of the electric properties and the Curie temperature. Our measurements will be done in temperature range (4.2 K, 450 K). The average nanoparticle diameter will be varied in range (5 nm, 100 nm). The crystallinity will also be varied in this range of nanoparticle diameter, since we expect that the crystallinity will affect the electric properties. To study the relaxation time, the nanoparticle diameter will be varied from few nanometers to about 20 nm, since thermal switching is expected in this diameter range. The relaxation time will be determined from frequency dependence of the real and the imaginary part of the dielectric constant.

6.2 The Dielectrics Relaxation

First we begin our discussion by introducing the models of Dieelctric relaxation in ferroelectric materials. Dielectric relaxation refers to a process that shows the response and stimulus of a dielectric medium to an external electric field. This relaxation is often described in terms of permittivity as a function of frequency, which can, for ideal systems, be described by the Debye relaxation [104]. The mechanism of dielectric relaxation is often subtle and complicated. For example, the distortion related to ionic and electronic polarization shows behavior of the resonance or oscillator type. The character of the distortion process depends on the structure, composition, and surroundings of the sample. In most cases, the dielectric relaxation is non-Debye relaxation.

6.2.1 The Debye Dielectrics Relaxation with a Single Relaxation Time

As early as 1927, Peter Debye [104] established that dielectric relaxation, the dispersion of the real permittivity (ε') and the occurrence of dielectric absorption (ε'') in the frequency domain for dipolar liquids and solids, was due to the reorientational motions of the dioples. Normally, the Debye relaxation response assumes that there is an assembly of a non-interacting ideal dipoles system that has the same waiting time before making a transition, or alternatively for an assembly of identical dipoles that have a loss of energy

proportional to frequency.

The Debye relaxation may be derived from several models of the microscopic constitution of matter. The simplest and most useful model is the "bistable" model, which has been treated quantitatively by Frohlich [105]. Most people call it the bistable model.

In this bistable model, first we assume a simple case that a single dipole with charge $e^+ - e^-$ may be in one or other of two states, 1 and 2 in absence of electric field. Those states are defined as minima of the potential energy, and the Δ is a potential hill in the middle of those states, as shown in figure 6.1 (A). Then dipole moment μ has two equilibrium states with opposite dipole direction, but with equal energy for states 1 and 2 in the absence of a field. In this model, it is very easily to see that state 2 is equivalent to a 180 degree turn of an angle of a dipole moment that is occupied by state 1.

When this microscopic system is applied by the external electric field E, the potential energy is shown in Figure 6.1 (B). The states 1 and 2 will be modified by this external electric field E. Hence, in the state 1, the potential energy will be shifted down $-\mu E$ over the state 1 in Figure 6.1 (A). The minus sign holds if well 2 is higher than well 1, as shown in the figure where the electric field points towards the up. Similarly, the potential energy of state 2 will be shifted up μE compared with the original state in Figure 6.1 (A) (without electric field).

Hence, in Figure 6.1 (B), the potential energy difference for states 1 and 2 will be:

$$\phi_1 - \phi_2 = \mu E - (-\mu E) = 2\mu E. \tag{6.1}$$

One of assumptions in Debye theory is: there is an assembly of non-interacting ideal dipoles system. Here we assume a number N of bistable dipoles/unit volume representing a very small density, so that the field due to dipolar interaction can be neglected. We also assume the equal potential energy for the state 1 and 2 in the absence of an electric field.

As we know, the dipole moment states 1 and 2 will not change on macroscopic scale because they do not have the energy to overcome the "potential hill" called energy barrier Δ between those states.

However, in a microscopic system, we can imagine that there are spontaneously active N

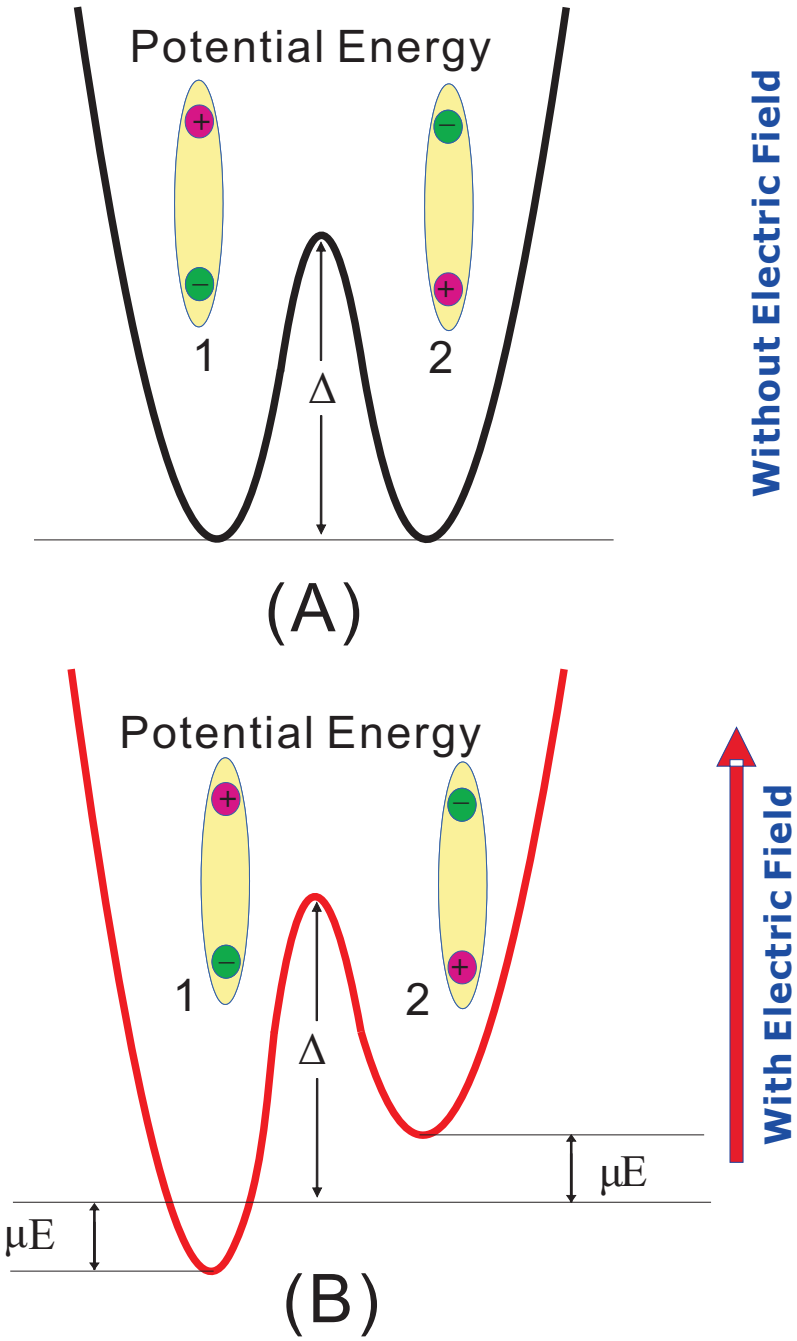

Figure 6.1: The Bistable Model. (A) In absence of an electric field, the potential energy, both in state 1 and 2 is shown in "potential well" two minima. (B) The potential energy is modified by an applied field E, the left-hand well is denoted by state 1, the right-hand well by state 2 (for example, the non-polarizable rigid dipoles). The two wells contain the dipole that may occupy either well.

bistable dipoles that exchange energy with each other dipole in a heat reservoir. Hence the directions of the dipoles fluctuate. For instance, the dipole in well 1 occasionally acquires an energy sufficient to lift it over the energy barrier Δ, and the dipole drops into the well 2 associated with it. On arrival in state 2, the energy of the dipole is returned to the heat reservoir, and the dipole stays in 2 until such time as it acquires enough energy from the reservoir to return over the energy barrier to state 1. In the case of absence of electric field (see Figure 6.1 (A)), the probability of finding it in either state 1 or 2 is the same.

According to statistical mechanics, the probability/unit time of those dipoles with energy $-\mu E$ (state 1) that jump over this double potential hill to arrive state 2 is given:

$$W_{1\to 2} = Ae^{-\frac{\Delta+\mu E}{K_B T}} \tag{6.2}$$

where A a factor that may or may not depend on the temperature, K_B is the Boltzmann constant, and T is the absolute temperature. The potential barrier Δ is usually described as an activation energy.

Similarly, the probability/unit time of jumps in the opposite direction, from 2 to 1, in the sketched case, is given by

$$W_{2\to 1} = Ae^{-\frac{\Delta-\mu E}{K_B T}} \tag{6.3}$$

When this microscopic system is kept in a thermodynamics equilibrium state, the population of N bistable dipoles in states 1 and 2 will not change with time if transportation only happens between states 1 and 2. then,

$$N_1 W_{1\to 2} = N_2 W_{2\to 1} \tag{6.4}$$

where N_1 is the number of occupied state 1, and N_2 is that of occupied state 2. The bistable dipole must be in one of the two states, and the total number of dipoles in occupied states/unit volume will no change, in order to agree with the physical condition. Hence, the total number of bistable dipoles is constant.

$$N_1 + N_2 = N. \tag{6.5}$$

The following are the time-dependent properties of this model. The change of state 1 with time should be equal to the sum of the number of dipoles that inflow from state 2 and outflow from 1. Thus

$$\frac{dN_1}{dt} = -N_1 W_{1\to 2} + N_2 W_{2\to 1}. \tag{6.6}$$

While the constancy of $N_1 + N_2$ (equation 6.5) gives:

$$\frac{dN_2}{dt} = -\frac{N_1}{dt}. \tag{6.7}$$

hence,

$$\frac{d(N_1 - N_2)}{dt} = 2\frac{dN_1}{dt}. \tag{6.8}$$

Putting equation 6.2 and 6.3 into equation 6.6, then

$$\frac{dN_1}{dt} = -N_1 A e^{-\frac{\Delta+\mu E}{K_B T}} + N_2 A e^{-\frac{\Delta-\mu E}{K_B T}}. \tag{6.9}$$

Thus the equation 6.8 can be written as:

$$\frac{d(N_1 - N_2)}{2dt} = -N_1 A e^{-\frac{\Delta+\mu E}{K_B T}} + N_2 A e^{-\frac{\Delta-\mu E}{K_B T}}, \tag{6.10}$$

$$\frac{1}{(2Ae^{-\frac{\Delta}{K_B T}})}\frac{d(N_1 - N_2)}{dt} = -N_1 e^{\frac{-\mu E}{K_B T}} + N_2 e^{\frac{\mu E}{K_B T}}. \tag{6.11}$$

In most cases it is permissible to assume

$$\frac{\mu E}{K_B T} \ll 1. \tag{6.12}$$

Developing equation 6.11 in terms of $\mu E/k_B T$, the average induced moment in the field direction is found to be

$$\frac{1}{(2Ae^{-\frac{\Delta}{K_BT}})}\frac{d(N_1-N_2)}{dt} = -N_1(1-\frac{\mu E}{K_BT}) + N_2(1+\frac{\mu E}{K_BT}) \tag{6.13}$$

$$= -(N_1-N_2) + (N_1+N_2)\frac{\mu E}{K_BT}. \tag{6.14}$$

This is a differential equation for the argument N_1-N_2. In general, the polarization/unit volume is given by that number of dipoles in one direction that are not compensated by dipoles in the opposite direction, namely:

$$P = (N_1-N_2)\mu. \tag{6.15}$$

According to equations 6.15 and 6.14, for the polarization P(t) form, the equation 6.14 is written:

$$\tau\frac{dP(t)}{dt} + P(t) = \frac{N\mu^2 E}{K_BT}, \tag{6.16}$$

where the relaxation time τ is expressed as:

$$\tau = \frac{1}{2A}e^{-\frac{\Delta}{K_BT}}, \tag{6.17}$$

here we set,

$$\varepsilon_s - \varepsilon_\infty = \frac{N\mu^2 E}{K_BT}, \tag{6.18}$$

where ε_s is the static dielectric constant ($\omega\tau \ll 1$), and ε_∞ is the high frequency dielectric constant where relaxation does not occur ($\omega\tau \gg 1$).

Then equation 6.16 may be generalized and written as:

$$\tau\frac{dP(t)}{dt} + P(t) = (\varepsilon_s - \varepsilon_\infty)E(t). \tag{6.19}$$

in a periodic electric field

$$E^*(t) = E_0 \cdot e^{i\omega t}, \tag{6.20}$$

Since the dielectric may have been polarized as a consequence of its previous history, we have to take into account the initial polarization at $t = 0$. The general solution of equation 6.19 can be expressed in term of a complex quantity $P^*(t)$ for the dipolar polarization:

$$P^*(t) = P_i e^{-\frac{t}{\tau}} + \frac{\varepsilon_s - \varepsilon_\infty}{1 + i\omega\tau} \cdot E_0 e^{i\omega t}, \tag{6.21}$$

where P_i is the initial polarization. It can be seen that the first term in right side of equation 6.21 decays with time, and it can be neglected in comparison with the second term for alternating current measurements. When the first term is neglected, the dielectric constant may be defined as

$$\epsilon^*(\omega) - \varepsilon_\infty = \frac{P^*(\omega, t)}{E^*(\omega, t)}, \tag{6.22}$$

where asterisks denote complex quantities. Inspection of equation 6.21 shows that for $P_i = 0$,

$$\epsilon^*(\omega, \tau) = \varepsilon_\infty + \frac{\varepsilon_s - \varepsilon_\infty}{1 + i\omega\tau} \tag{6.23}$$

here ϵ^* may be separated into its real and imaginary parts, since

$$\epsilon^*(\omega, \tau) = \varepsilon'(\omega, \tau) - i\varepsilon''(\omega, \tau). \tag{6.24}$$

so the real and imaginary parts of the permittivity are:

$$\varepsilon'(\omega, \tau) = \varepsilon_\infty + \frac{(\varepsilon_s - \varepsilon_\infty)}{1 + \omega^2\tau^2} \tag{6.25}$$

and

$$\varepsilon''(\omega, \tau) = \frac{(\varepsilon_s - \varepsilon_\infty)\omega\tau}{1 + \omega^2\tau^2}. \tag{6.26}$$

the equations 6.25 and 6.26 are usually called Debye equations because they were derived by Debye on a molecular basis [104]. The dielectric response of non-interacting dipoles should follow this classical frequency response.

6.2.2 The Non-Debye Dielectric Relaxation with Many Relaxation Times

In the pervious subsection, the Debye relaxation (with a single relaxation time) is easily understood. However, the pure Debye relaxation is hardly ever found in nature and deviations from it may be relatively slight. Usually the measured dielectric functions are much broader than predicted by the Debye function. Moreover, in many cases the dielectric function is asymmetric. That means the short time (high frequency) behavior is more pronounced than the long time (low frequency) one. This is called non-Debye, or sometime non-ideal, dielectric relaxation behavior.

One can consider intuitively the Debye relaxation as a basic relaxations, the complicated and varied relaxation can be described naturally by many Debye relaxation behaviors. Formally the non-Debye relaxation behavior can be expressed in every case by a superposition of Debye-functions with different relaxation times. It should be pointed out that a formal separation of non-Debye relaxation behavior into different Debye relaxation processes does not justify a dipole interpretation according to independent Debye-like relaxation processes (see equation 6.23).

For this purpose, one can expect a distribution function for the relaxation time. K.S. Cole and R.H.Cole [106] gave the first empirical expressions for $\epsilon^*(\omega)$ in 1941. They evaluated their experimental data by a graphical display which plot $\varepsilon''(\omega)$ against $\varepsilon'(\omega)$ in complex plane. This kind diagram is often called as Cole-Cole plot. The cole-cole plot provides an excellent method to determine whether a system has a single relaxation time. This method is also very useful to characterize what the types of distribution function are.

A simple evaluation from the Debye equations 6.25 and 6.26, represents the Debye relaxation with a single relaxation time. Hence the Cole-Cole plot of the imaginary part of the complex relative permittivity against the real part is a semicircle. This is

$$\left(\varepsilon'(\omega) - \frac{\varepsilon_s + \varepsilon_\infty}{2}\right)^2 + \varepsilon''(\omega)^2 = \left(\frac{\varepsilon_s - \varepsilon_\infty}{2}\right)^2. \tag{6.27}$$

In many cases the Cole-Cole plot curve falls inside the Debye semicircle. K.S. Cole and R.H. Cole [106] suggested that in this case the permittivity might follow the empirical

equation

$$\epsilon^*(\omega,\tau) = \varepsilon_\infty + \frac{\varepsilon_s - \varepsilon_\infty}{1 + (i\omega\tau)^{(1-\alpha)}}, \tag{6.28}$$

where α is a constant, $0 \leq \alpha < 1$. In the limit $\alpha = 0$, of course, the Cole-Cole curve reduces to the Debye semicircle which is relaxation with only a single relaxation time. This type of Cole-Cole plot is symmetrical about a line through the center, parallel to the ε'' axis.

However, Cole and Davidson [107] found another type equation where the experimental results for certain materials, for example glycerol, do not have this symmetry, the Cole-Cole plot may be a skewed arc. They suggested that behavior of this kind asymmetry could be represented by the equation

$$\epsilon^*(\omega,\tau) = \varepsilon_\infty + \frac{\varepsilon_s - \varepsilon_\infty}{(1 + i\omega\tau)^\beta} \tag{6.29}$$

where β is again a constant, $0 < \beta \leq 1$. This equation seems to be very successful in representing the behaviour of substance at low temperatures. When $\beta \to 1$, the arc tends to a Debye semicircle again.

The third type relaxation function is the Negami-Havriliak (NH) equation [108], which has been widely used to describe the relaxation behavior of glass-forming liquids and complex systems.

$$\epsilon^*(\omega,\tau) = \varepsilon_\infty + \frac{\varepsilon_s - \varepsilon_\infty}{\left(1 + (i\omega\tau)^\alpha\right)^\beta} \tag{6.30}$$

here α and β are constants, in the range of $0 \leq \beta \leq 1$. It is easily seen that this equation is both a generalization of the Cole-Cole equation, to which it reduces for $\beta = 1$, and a generalization of the Cole-Davidson equation, to which it reduces for $\alpha = 1$.

All those empirical equations can be very successful in explaining the experimental results of dielectric behaviors in frequency domain. Actually the dielectric relaxation behavior can be also understood by the natural time domain. The most widely accepted interpretation invoked the concept of distribution of relaxation times (DRT) (see Appendix C), that modified the Debye expression equation 6.9 by introducing integration over the distribution

function $F(ln\tau)$ of loss peak frequencies. Let $F(\tau)d(ln\tau)$ be the fraction of the orientation polarization processes that have relaxation times between τ and $\tau + d\tau$. Then the complex permittivity is written as:

$$\epsilon^*(\omega,\tau) = \varepsilon_\infty + (\varepsilon_s - \varepsilon_\infty)\int_0^\infty \frac{F(\tau)d(ln\tau)}{1+i\omega\tau}. \tag{6.31}$$

separating real and imaginary parts:

$$\varepsilon'(\omega,\tau) = \varepsilon_\infty + (\varepsilon_s - \varepsilon_\infty)\int_0^\infty \frac{F(\tau)d(ln\tau)}{1+\omega^2\tau^2} \tag{6.32}$$

$$\varepsilon''(\omega,\tau) = (\varepsilon_s - \varepsilon_\infty)\int_0^\infty \frac{\omega\tau F(\tau)d(ln\tau)}{1+\omega^2\tau^2} \tag{6.33}$$

And here we define

$$\int_0^\infty F(\tau)d(ln\tau) = 1 \tag{6.34}$$

Thus, in relaxation time domain, the Cole-Cole and Cole-Davidson types can be described as arising from the existence of a continuous spread of relaxation times, each of which alone would give rise to a Debye type of behavior. The $F(ln\tau)$ can be obtained by doing the Laplace transform in the Cole-Cole and Cole-Davidson distribution functions 6.28 and 6.29 that are in frequency domain. Then the Cole-Cole function corresponds to a logarithmic relaxation time distribution function (see Appendix C).

In time domain, the expression for the pulse-response function cannot be obtained directly using the inverse Laplace transform to the Cole-Cole equation. Instead, the pulse-response function can be obtained indirectly by developing equation 6.28 in series. Taking the Laplace transform to the series one can obtain:

$$F(\tau) = \frac{1}{2\pi}\frac{sin\alpha\pi}{cosh[(1-\alpha)(\frac{\tau}{\tau_0})] - cos\alpha\pi}. \tag{6.35}$$

From the Cole-Davidson equation, the pulse-response function can be obtained directly by taking the inverse Laplace transform equation 6.29: and the Cole-Davidson distribution function that corresponds to it is given by

$$F(\tau) = \frac{sin\beta\pi}{\pi}\left(\frac{\tau}{\tau_0 - \tau}\right)^{\beta}. \tag{6.36}$$

In many cases the non-Debye relaxation behavior in the time domain is described empirically by the Kohlrausch-Williams-Watts (KWW) relaxation function. This function was introduced in 1863 to describe mechanical creep in glassy fibers [109] and later was used by Williams and Watts [110] in 1970 to describe dielectric relaxation in polymers. Though the KWW and NH relaxation functions are not exactly the Laplace transform in each other. They have a natural relationship that is proven by Alvarez's analytical paper [111].

The KWW relaxation function is:

$$F(\tau) = exp\Big[-\big(\frac{t}{\tau_{KWW}}\big)^{\beta_{KWW}}\Big] \tag{6.37}$$

the stretching parameter β_{KWW} $(0 < \beta_{KWW} \leq 1)$ leads to an asymmetric broadening of $F(\tau)$ at short times (high frequencies) compared with the exponential decay ($\beta_{KWW} = 1$). τ_{KWW} is the related relaxation time.

In the experimental cases, the $F(\tau)$ was extracted from the observed values of $\epsilon^*(\omega)$ that used to be described by the Debye (D), Davidson-Cole (DC), Kohlrausch-Williams-Watts (KWW), and the Cole-Cole (CC) empirical relaxation functions.

The relaxation time distribution functions are shown in Figure 6.2, where τ_D, τ_{CC}, τ_{KWW} and τ_{DC} are the most probable relaxation times for the corresponding laws. From the Figure 6.2, we can see that $F(\tau)$ is the an symmetrical distribution for Cole-Cole(CC) relaxation function, and the distribution function is asymmetrical form for the Davidson-Cole (DC) and Kohlrausch-Williams-Watts (KWW) relaxation function. But the $F(\tau)$ for Debye function is usually only one relaxation time.

In relaxor ferroelectrics, dielectric constants show strong dispersion of dynamic dielectric response, Because of this dynamic characteristics (frequency dependence of dielectric permittivity $\epsilon^*(\omega)$, polarization etc.) are caused by the very broad relaxation time distribution function $F(\tau)$.

However, the $F(\tau)$ (DRT) interpretation has the difficulty that there were no independent ways of confirming the form of $F(\tau)$ required to give the desired to experimental data.

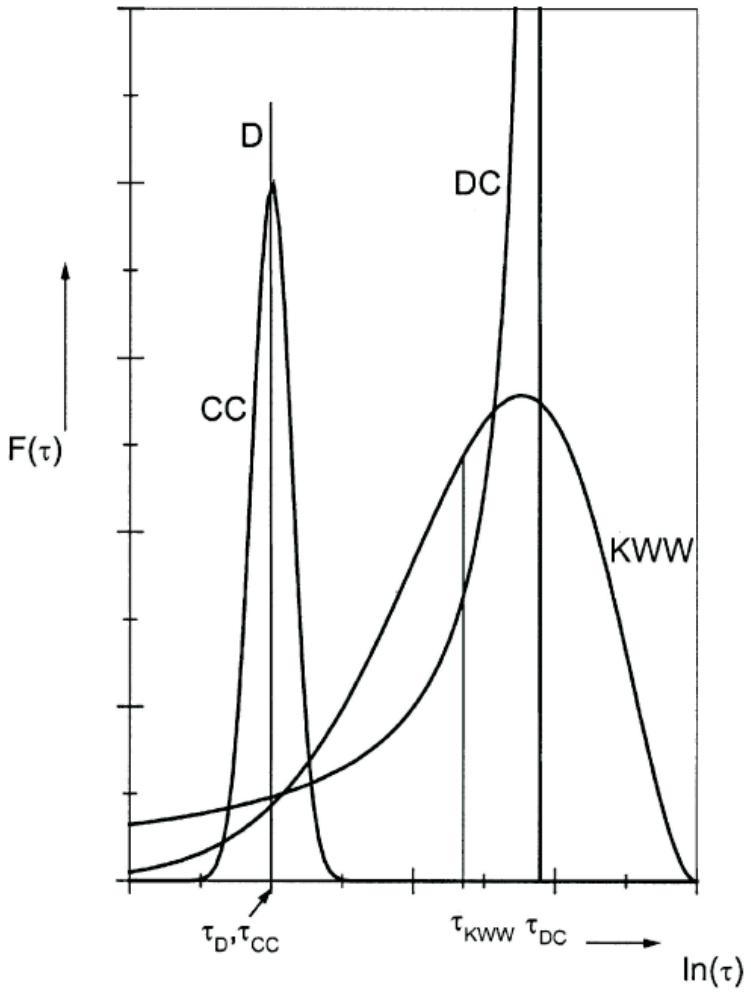

Figure 6.2: Relaxation time distributions for Debye (D), Cole-Cole(CC), Davidson-Cole (DC) and Kohlrausch-Williams-Watts (KWW)laws. From reference [112].

Moreover, the DRT approach fails to address the evident existence of universal fractional power law behavior that represents very well the high-frequency dipolar behavior.

There are some other theories proposed as an explanation for the non-Debye behavior of dynamic dielectric response in relaxor ferroelectrics, such as non-interacting polar regions in the superparaelectric model [113], dipolar glass state [114], micro domain state due to quenched random electric fields [115], random field theory based model [116], and Jonscher's many-body model [117]. However, all those interpretations seem to be plausible enough in different group materials.

The task of dielectric theory is so difficult because permanent dipoles cannot always

be identified, but mainly because they mutually influence one another; A dipole is not only subject to the influence of a field but also has a field of its own. Therefore, that it is essential to look for a more fundamentally satisfying interpretation of the relaxation behavior. Additional experimental and theoretical investigations are extremely desirable.

6.3 The Relaxation Time-Temperature Dependence Theories

The dielectric relaxation time τ refers in the last resort to the regression time of fluctuations of the polarization, and it is normally dependent on temperature. The common relationship for a single relaxation time τ is given by equation 6.17, and is called the Arrhenius Law. At the beginning, the Arrhenius Law is used to calculate the rate constant of a chemical reaction. Later, it is used in dielectric relaxation, and is the theory of rate process with temperature dependence.

$$\tau = \tau_0 \cdot e^{-\frac{\Delta}{K_B T}}. \tag{6.38}$$

Another type of relaxation time with temperature dependence is added by the pre-exponential factor compared with Arrhenius Law. In this form, we can draw conclusions regarding activation energies and pre-exponential factors from the shift with temperature of wide relaxation peaks. The expression is

$$\tau = \frac{\tau_0}{T} e^{-\frac{\Delta}{K_B T}}. \tag{6.39}$$

this equation is an appropriate approximation, τ_0 and Δ being constants, and is used successfully in many cases, particularly polymer.

In relaxor ferroelectrics, a large number of studies of dynamic properties have revealed a common feature of their behavior, namely a specific slowing down of the relaxation processes, which may be considered as a sum of those of relaxor ferroelectrics having an exponentially wide and smooth spectrum of the relaxation times. Such behavior is known to be an important characteristic for all disordered systems, i.e. relaxation processes.

It is commonly attributed to an evolution of the exponentially wide spectrum of the relaxation time τ rapidly increasing up to the macroscopic times scale, when the temperature decreases towards some characteristic temperature T_0, i.e., it is attibuted to singular, or at least very fast, broadening of the spectrum at $T \to T_0$.

$$\tau = \tau_0 \cdot e^{-\frac{\Delta}{K_B(T-T_0)}}. \tag{6.40}$$

this equation is called as the Vogel-Fulcher (VF) Law [118]. Under certain conditions, the equation corresponds to the Vogel-Fulcher ($T_0 \neq 0$) and Arrhenius ($T_0 = 0$) Laws for relaxation time-temperature dependence. In general, the VF Law of relaxation behavior was observed experimentally in all relaxors, and it is really the most important feature of a relaxor.

CHAPTER VII

DEVICE FABRICATION AND MEASUREMENTS

7.1 Materials Synthesis Methods

The progress in nanotechnology has led to a variety of novel techniques for fabrication of nanoparticles. Nowadays, there is a focus on large scale production of nanoparticles made from ferroelectric materials. There are several companies that produce nanoparticles using ball laser ablation, vapor condensation, sputtering, chemical precipitation, sol-gel processing, combustion synthesis, and plasma synthesis.

The early standard synthesis of ferroelectric nanoparticles included sol-gel techniques [119] and solution synthesis of mono-disperse $BaTiO_3$ nanoparticles [120]. Single crystal nanorods composed of $BaTiO_3$ and $SrTiO_3$ have also been synthesized by solution chemistry [121]. In particular, nonvolatile electric polarization can be reproducibly induced and manipulated on nanowires as small as 10 nm in diameter. Lead zirconate titanate (PZT) nanoparticles have also been synthesized by laser ablation [122]. Amorphous PZT nanoparticles began to crystallize above 600 $^{\circ}C$, and they became a perovskite (ferroelectric) structure at 900 $^{\circ}C$. Single crystal $BaTiO_3$ and $SrTiO_3$ nanostructures have been synthesized also by annealing of powdered chemical components at 820 $^{\circ}C$ [123]. Additionally, mesoporous PZT powders with nanoparticles of diameter 50 nm-60 nm have been created from the aqueous solution of Pb^{2+}, Zr^{4+}, and Ti^{4+} cations [124]. Similarly, the loosely connected submicron sized perovskite oxide particles have been synthesized by metathesis, at considerably lower temperatures than those for their synthesis by ceramic methods [125]. Recently, monodisperse PZT perovskite nanoparticles with diameters of 9 nm were produced by laser ablation followed by a gas-phase annealing at 900 $^{\circ}C$ [126].

More recently Liu, et al., [127, 128] have invented a generic approach for the synthesis of single-crystal complex oxide nanostructures of perovskites. The method is based on a reaction between a metallic salt and a metallic oxide in a solution of composite hydroxide

eutectic at 200 $^{\circ}C$ and 1 atm without using an organic dispersant or capping agent. The advantage of this one-step synthesis technique is cost-effective, easy to control, and can be conducted at low temperature and normal atmospheric pressure.

In this thesis, we selected $BaTiO_3$ (BTA) and $Ba_{0.77}Sr_{0.23}TiO_3$ (BST) manufactured by nGimat Co., a nanotech company in Atlanta. Those BTA and BST nanoparticles were created by combustion chemical vapor condensation (CCVD) technique, which works by decomposing metalorganic precursors in nanospray diffusion flames [129]. The key advantage of this technique is that the particles do not require any further thermal treatment to make them ferroelectric. Another advantage of CCVD nanopowders is that the nanoparticles are of high purity and have controlled properties (crystallinity, size, morphology).

The X-ray diffraction (XRD) of BST nanopowders are shown in Figure 7.2. The average nanoparticle size is 30 nm, the size range where we expect strong size effects on ferroelectricity. The nanoparticle shape is close to spherical. The nanoparticles are connected by the weak van der Waals forces and they can be separated by sonication in solvents. TEM demonstrates that the particles are crystalline. XRD-crystallite size is $\sim$ 10 nm.

7.2 BST Nanoparticles Character Measurements

The BST ($Ba_{0.77}Sr_{0.23}TiO_3$) and BTA nanoparticles were manufactured by nGimat Company (http://www.microcoating.com/nanotech/advantages.html). Figure 7.1 shows the images of these BST nanoparticles, where Figure 7.1 (A) is the image of Transmission Electron Microscopy (TEM), and the Figure 7.1 (B) obtained by the field emission scanning electron microscopy (SEM). Most particles are spherical and the diameter varies from 5 nm to 100 nm. Most particles are not single crystal, and the crystallite size varies in a similar diameter range.

The X-ray diffraction (XRD) pattern of the BST powder is shown in Figure 7.2 (A). All the peaks in the XRD pattern are attributed to the BST perovskite cube; the average crystallite size of the particles is 32 nm, which is estimated from the broadening of the (111) plane diffraction peak using the Scherrer equation.

In the perovskite structure, (Ba or Sr)-cations (represented by A in Figure 7.2 (B)) and

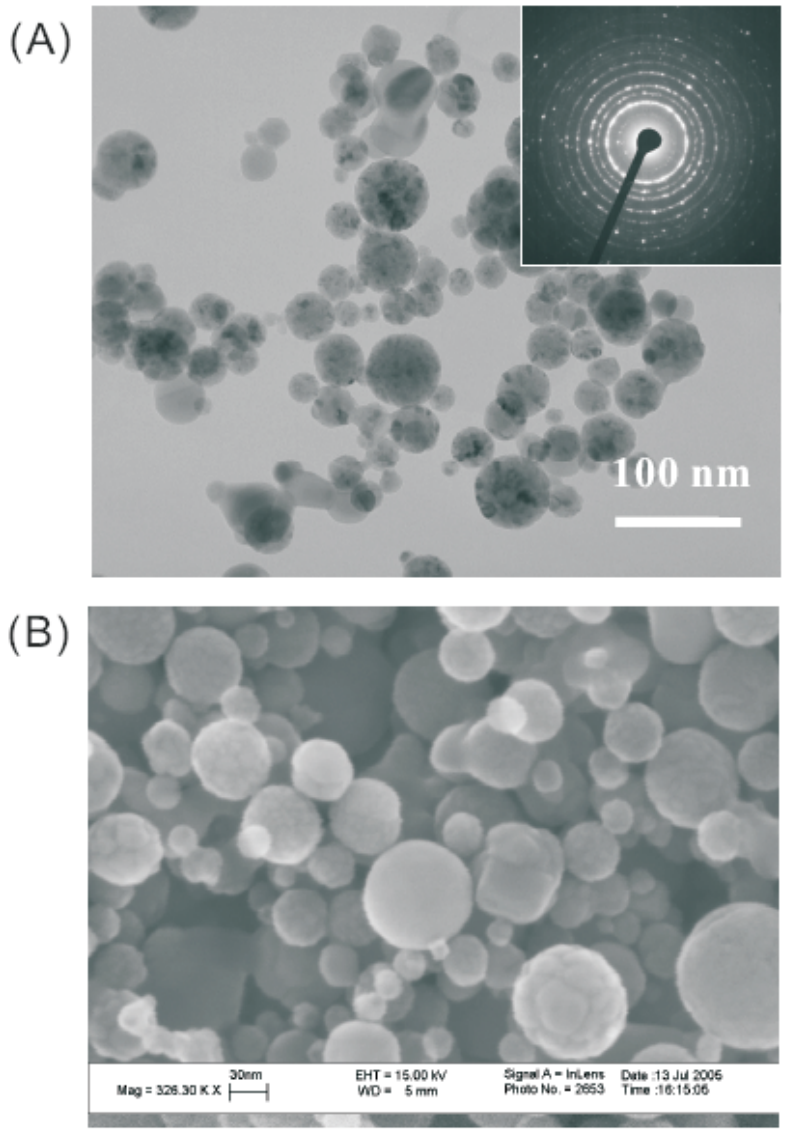

Figure 7.1: (A) The TEM image of BST nanoparticles; (B) the SEM image of BST nanoparticles. The BST nanoparticles have different sizes, and most particles are spherical and the diameter varies from 5 nm to 100 nm.

oxygen-anyons (represented by O in Figure 7.2 (B)) are cubic close packed, with the smaller Ti-cations (represented by B in Figure 7.2 (B)) occupying the octahedral holes between the oxygen-anions. Ti-cations can be displaced slightly, because they are too small for close packing with the oxygens. Since Ti-cations carry electrical charges, such displacements can result in a net electric dipole moment. The material is a ferroelectric, by analogy with a ferromagnet that contains magnetic dipoles.

The BST nanoparticles diameters distribution is in the range of $5 - 100\ nm$. We can consider that the (BaO or SrO) (+) and TiO_2 (-) dipole moment in a single unit cell. We will see that the structures for our BST nanoparticles are very complicated in high resolution TEM images, and those particles have different crystallitic structure even though they have same diameter sizes. The Ti-cations can be easily displaced slightly from normal position due to the internal and external electric field. Hence, it is very hard to estimate the polarization of individual particle with the certain size.

At high temperature, Ti-cations can jiggle around in the larger holes between oxygens, maintaining cubic symmetry. The static displacement occurs when the structure is cooled below a certain transition temperature, known as the Curie temperature (T_C). The displacement along the z-axis results in tetragonal symmetry. Below the Curie temperature, the electric polarization can point in two opposite directions, as sketched in Figure 7.2 (B).

This size is similar to the average size of the BST particles observed from SEM and Transmission Electron Microscopy (TEM), Figure 7.1. Figure 7.3 shows a high-resolution TEM image of BST particles, and demonstrates that some BST particles are crystalline (as shown in Figure 7.3 (A)), some are multi-crystalline (as shown in Figure 7.3 (B)).

7.3 Device Fabrication

Our samples are capacitors containing a dense array of nanoparticles in the insulation layer between the capacitor plates, sketched in Figure 7.4. The capacitors are fabricated in two evaporation steps. First, an aluminum film with a basal area of $2 \times 20\ mm^2$ is thermally evaporated on a SiO_2 substrate through a mask at 4×10^{-7} Torr pressure, and the Al film is then exposed to air. The nanoparticles are sonicated in methanol, which makes them well

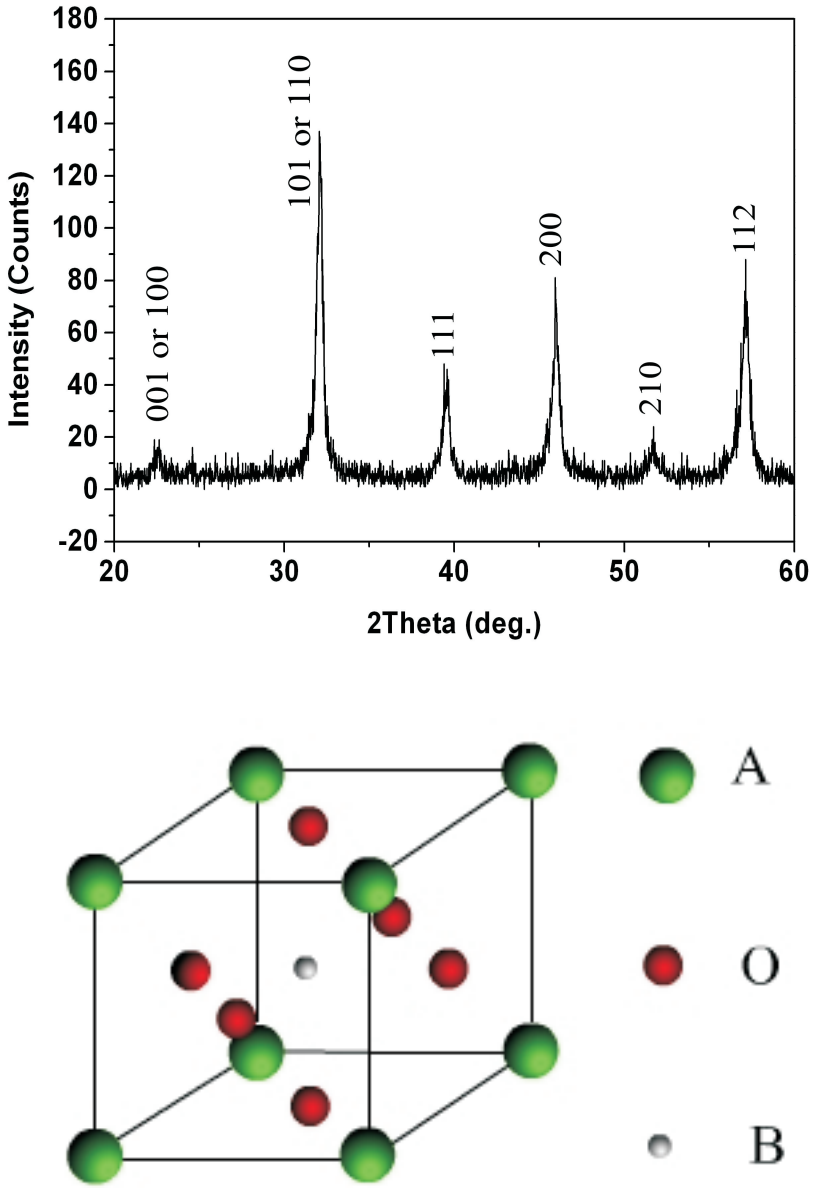

Figure 7.2: (A) The XRD pattern of BST nanoparticles: All the peaks in the XRD pattern are attributed to the BST perovskite cube; the average crystallite size of the particles is 32 nm, which is estimated from the broadening of the (111) plane diffraction peak using the Scherrer equation. (B) The typical perovskite cube structure: (Ba or Sr)-cations (represented by A) and oxygen-anyons (represented by O in the sites of face centers) are cubic close packed, with the smaller Ti-cations (represented by B) occupying the octahedral holes between the oxygen-anions.

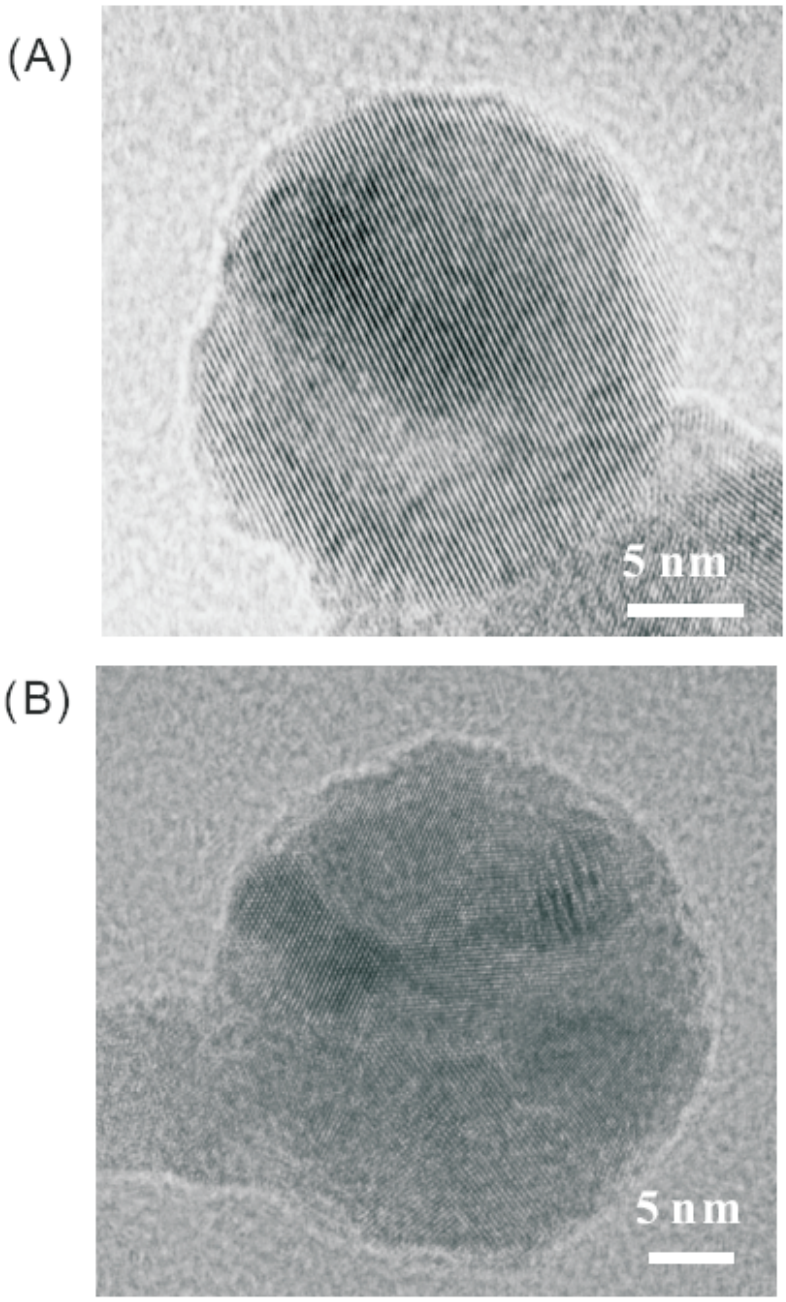

Figure 7.3: The high-resolution TEM images of BST nanoparticles. (A) These high-resolution TEM images show that these BST particles are single crystalline, with diameter size around 35 nm. (B) These high-resolution TEM images show that these BST particles are multi-crystalline, with diameter size around 35 nm.

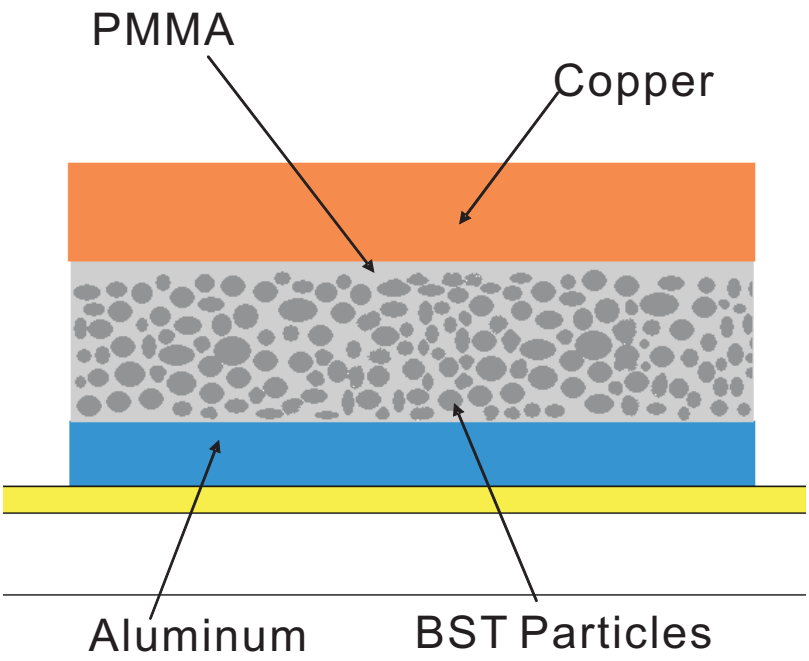

Figure 7.4: The sectional structure of the capacitor embedded with BST nanoparticles: the bottom layer is an aluminum film with a basal area of $2 \times 20\ mm^2$ is thermally evaporated on a SiO_2 substrate. Next, an uniform 5 μm thick BST nanoparticles film are deposited. After that, the BST nanoparticles are spin-coated by a 400 nm thick layer of polimethylmetacrylate (PMMA). Finally, the top film is covered with a copper layer.

dispersed. Several drops of this methanol mixture are placed evenly over the Al film and then dried. This process creates a uniform deposit with thickness in the range of $\sim$ 100 nm - 5 μm, depending on the nanoparticle density in methanol. In our case, 5 μm thick BST nanoparticles are deposited, and the thickness is measured by observing the cross-section with an optical microscope.

In the next step, the nanoparticles are spin-coated by a 400 nm thick layer of polimethylmetacrylate (PMMA) and baked at 150 $^{\circ}C$ to dry the PMMA. Finally, the nanoparticle film is covered with the top copper layer by thermal evaporation. All those arrangements are essential to measure the sample temperature in the immediate sample neighborhood and to keep the sample temperature as constant as possible.

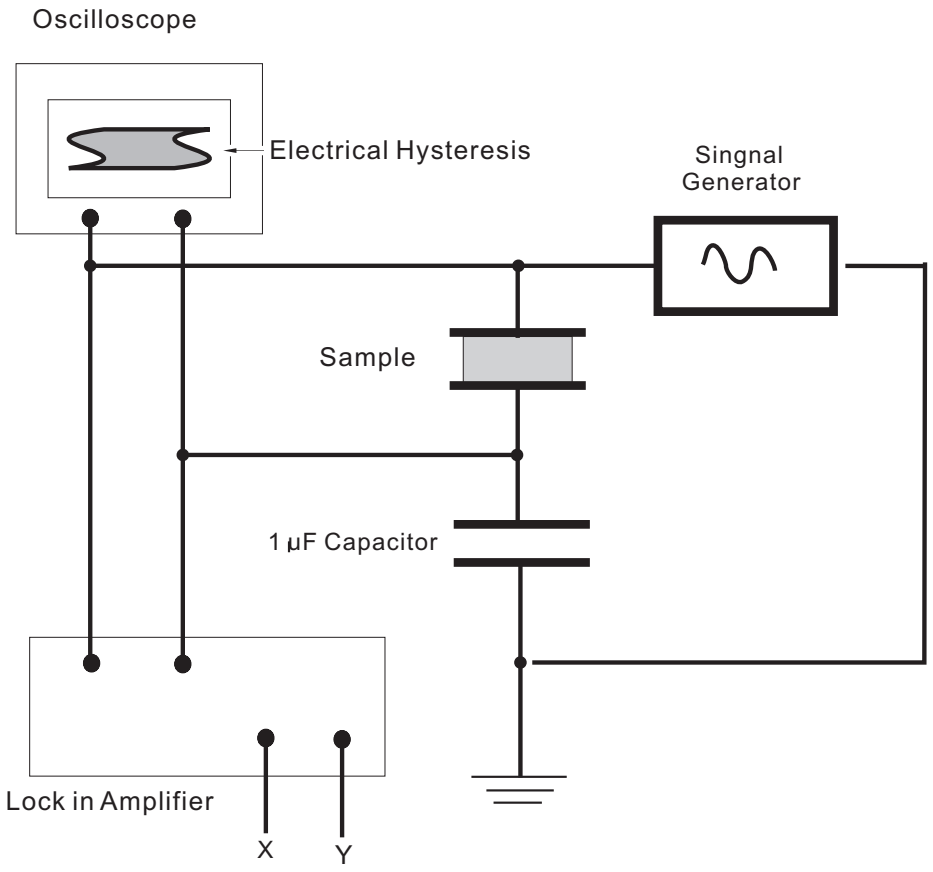

Figure 7.5: The measurement set-up of Sawyer-Tower Circuit.

7.4 Measurement Methods and Procedures

The complex dielectric function $\epsilon^* = \varepsilon' - i\varepsilon''$ can be measured in the very broad frequency regime from 10^{-6} Hz up to 10^{12} Hz. To span this dynamic range, different measurement systems based on different measurement principles have to be combined. Fourier correlation analyzers (10^{-6} Hz to 10^{7} Hz), impedance analyzer (10 Hz to 10^{6} Hz), network analyzers (10^{7} Hz to 10^{10} Hz), quasi-optical interferometers (10^{10} Hz to 10^{12} Hz), and fourier spectrometers (10^{11} Hz to IR).

Our typical samples have a capacitance of 3.5 pF. The sample geometry is a parallel plate capacitor arrangement. For the techniques discussed so far, a sample cell that is connected by BNC cables to the impedance plugs of the measurement system. Due to the parasitic inductance of the BNC lines and connectors the high frequency limit is reached at about 1 MHz (coaxial line reflectometry has to be employed at frequencies from 1 MHz

to 10 GHz). Where very low frequency range end, very small currents down to fA have to be measured. In this region, the measurement may be obscured by noise pick up and piezoeletric charges in the cables due to mechanical stress. Therefore a sophisticated cell and cable optimized design is required for both higher frequency (above 1MHz) and Lower frequency (low 0.1 Hz) performance.

Our measurements are performed in the temperature range $(4.2K, 340K)$ using a liquid helium cryostat. Both complex capacitances and electrical hysteresis are measured by the Sawyer-Tower circuit [130], which is sketched in Figure 7.5. In the Sawyer-Tower circuit, the sample capacitor is in series with a reference capacitor (1 μ F) that is much larger than the specimen capacitor. It should be noted that the hysteresis loop can also be exhibited on the oscilloscope. The circuit is driven by a $0.1V$ RMS sinusoidal signal, provided by signal generator at frequencies $(10, 10^2, 10^3, 10^4, 10^5)Hz$. The dielectric properties are commonly expressed as complex plane plots of permittivity, $\epsilon^* = \varepsilon' - i\varepsilon''$, and the equivalent complex capacitance given by $C^* = C' - iC''$ (the details are described in B). Using our sample dimensions, we can covert between ϵ^* and C^* as $\epsilon^* = (1.41 \times 10^{10} F^{-1}) \cdot C^*$ (see Appendix B, equation B.2).

CHAPTER VIII

EXPERIMENTAL RESULTS AND ANALYSIS

8.1 The Temperature Dependence of the Complex Permittivity

The capacitance (C' and C'') versus temperature (T) in a typical sample is shown in Figure 8.1. The data is obtained with an AC field corresponding to 0.1 Volt RMS and frequency 10^3 Hz. In Figure 8.1 (A) and (B), the thick and the thin line corresponds to increasing and decreasing temperatures, respectively. When the temperature increases from 4.2 K, initially both C' and C'' are constant and small. They are comparable to the stray capacitance of the leads. However, when temperature reaches approximately 20 K, there is a significant and rapid increase in C' accompanied by a sharp peak in C''. Later in the text we will show that the C'-increase and C''-peak are frequency dependent. When the temperature is larger than about 30 K, both C' and C'' are constant again, until the temperature becomes close to 200 K. When the temperature increases above 200 K, both C' and C'' increase quickly and display a broad peak centered around 270 K. In addition, there are a few smaller peaks between 210 K and 340 K.

When the temperature decreases from 340 K to 4.2 K, C' and C'' exhibit hysteresis. The broad peak centered around 270 K has reduced amplitude upon reducing the temperature. However, at around 200 K, C' and C'' saturate and there is no more hysteresis below 200 K. That is, when the temperature is below 200 K, C' and C'' versus T is a single valued function of temperature. Only the temperature range above 210 K is characterized by hysteresis. The broad maximum in permittivity versus temperature above 210 K is a behavior typical for relaxor ferroelectrics [113]. In this thesis we focus on the low temperature properties of the nanoparticles ($T < 200K$), where C' and C'' are single valued functions of temperature.

To determine the electric polarization versus applied electric field, we drive the capacitor by a triangle wave form with amplitude 3 V and frequency 10^3 Hz. We use the Sawyer-Tower

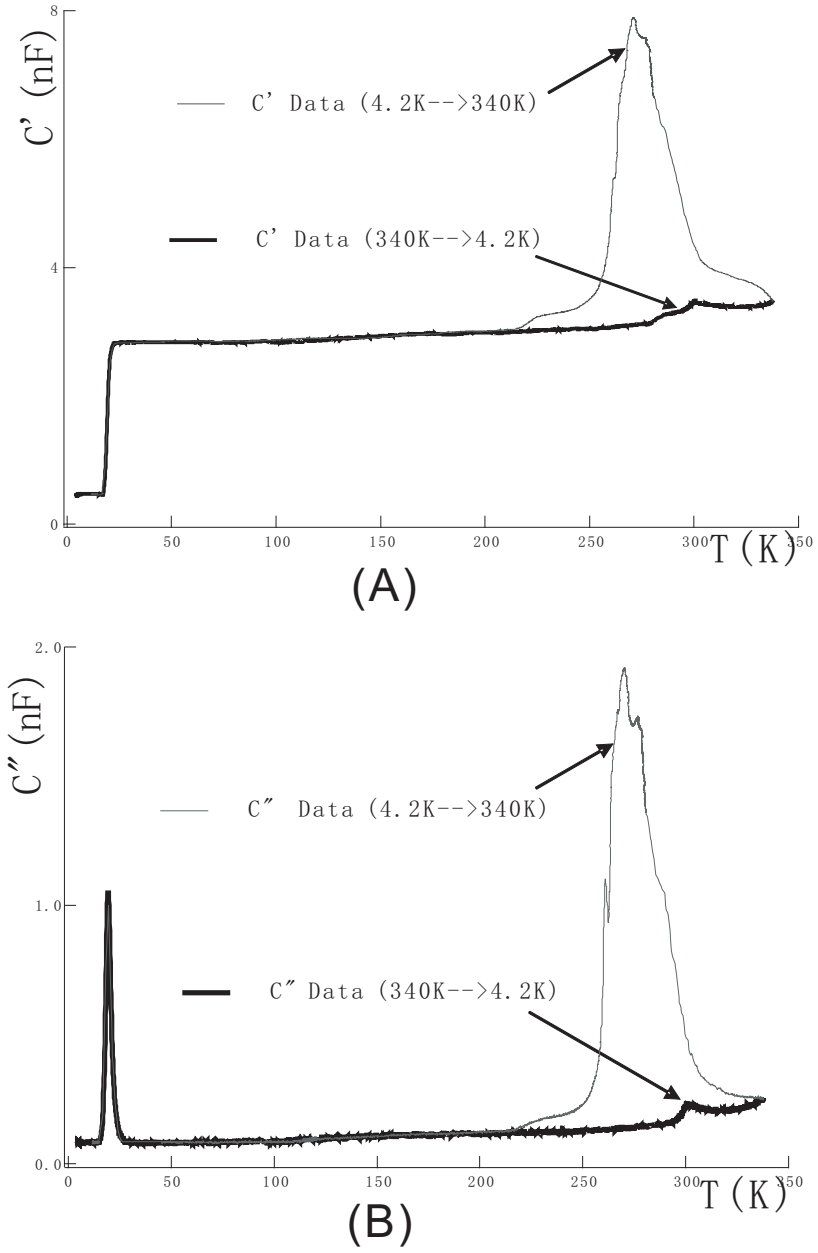

Figure 8.1: (A) Temperature dependence of C' and (B) C'' measured at $10^3 Hz$. The BST capacitor is driven by a triangle wave form with amplitude 3 V and frequency 10^3 Hz. The thick and the thin lines correspond to increasing and decreasing temperatures, respectively. The data was obtained by measuring the Sawyer-Tower circuit.

circuit (Figure 7.5). Figure 8.5 displays the resulting polarization versus applied voltage. At temperatures close to the peak in C'' near 20 K and in the temperature range above 210 K, hysteresis is observed. P_r is the effective remanent polarization, E_c is the effective coercive field, and P_s is the effective spontaneous polarization. P_r , E_c , and P_s are not necessarily the same as the remanent polarization, the coercive field, and the saturation polarization, respectively, because the hysteresis loop could originate from the time delay in the electric response. In particular, if the electric relaxation time is comparable to the period of the triangle wave, the hysteresis will occur because of the time delayed electric response of the sample.

8.2 The Different Frequencies Measurements at Low Temperature

In the same way, the experimental data was obtained by measuring the Sawyer-Tower circuit, where is driven by a sinusoidal eletrical field which the aplitudate is 0.1 Volt RMS and kept same frequency when we change the sample's temperature. The results of our measurements of the complex capacitance C' and C'' versus temperaure (T) are shown in Figure 8.2 (A) and (B). All data are measured at frequencies $(10, 10^2, 10^3, 10^4, 10^5)$ Hz and at a temperature range of 4.2 K- 65 K.

On the assumption there is a Debye relaxation, a simple evaluation of equation 6.26 shows that the ε'' have maximum value when $\omega\tau = 1$, then

$$\varepsilon' = \frac{\varepsilon_s + \varepsilon_\infty}{2} \tag{8.1}$$

$$\varepsilon''_{max} = \left(\frac{\varepsilon_s - \varepsilon_\infty}{2}\right) \tag{8.2}$$

The positions of maxima correspond to the condition $\omega\tau(T = T_m) = 1$ in Figure 8.2 (B). Namely, the C'' has a maximum when $\omega\tau = 1$. The relaxation time is equal to $\tau = 1/\omega$ where the ω is the drive frequencies we setup. In this way, we can find out the temperature T_m corresponding to C'' has a maximum in Figure 8.2 (B) with different frequencies.

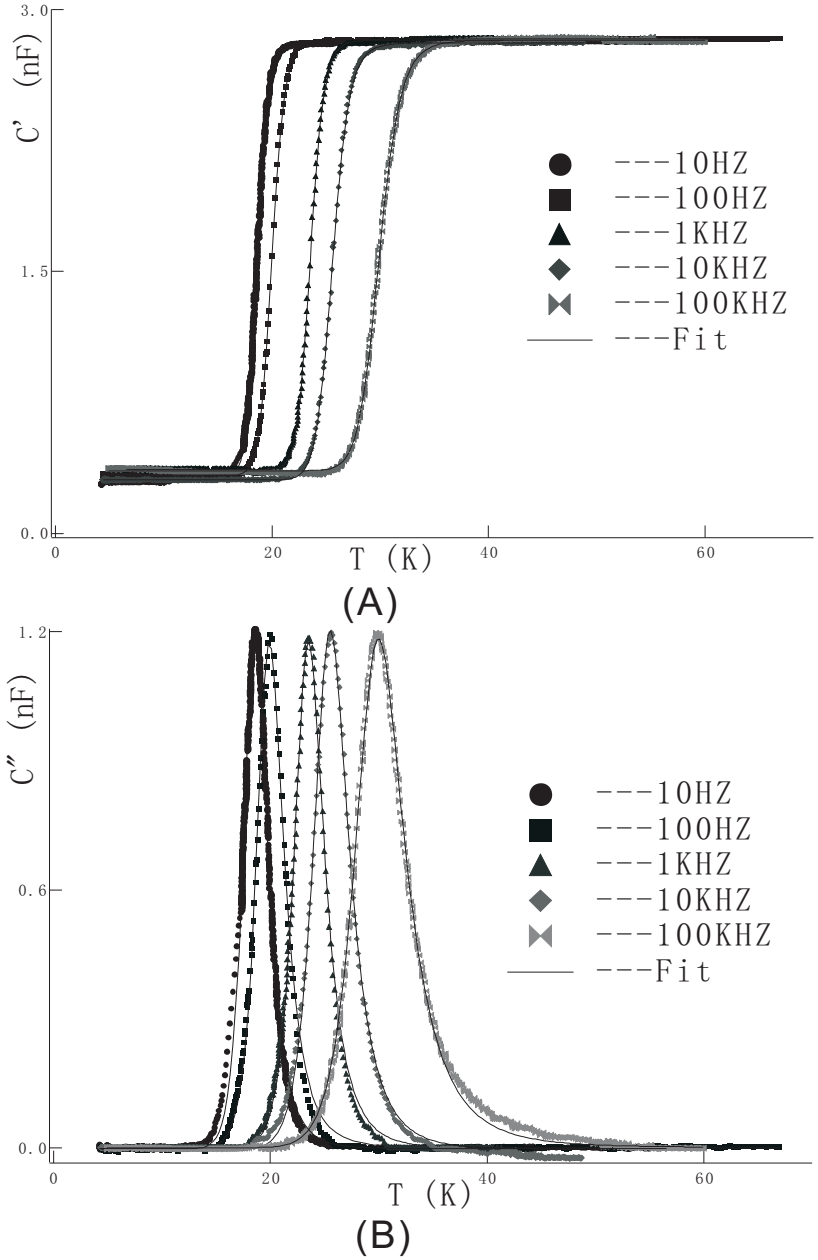

Figure 8.2: Temperature dependence at different frequencies of (A) the real parts C' and (B) the imaginary parts C''. All data are measured at frequencies $(10, 10^2, 10^3, 10^4, 10^5)$ Hz and at a temperature range of $4.2K - 65K$. The data was obtained by measuring the Sawyer-Tower circuit.

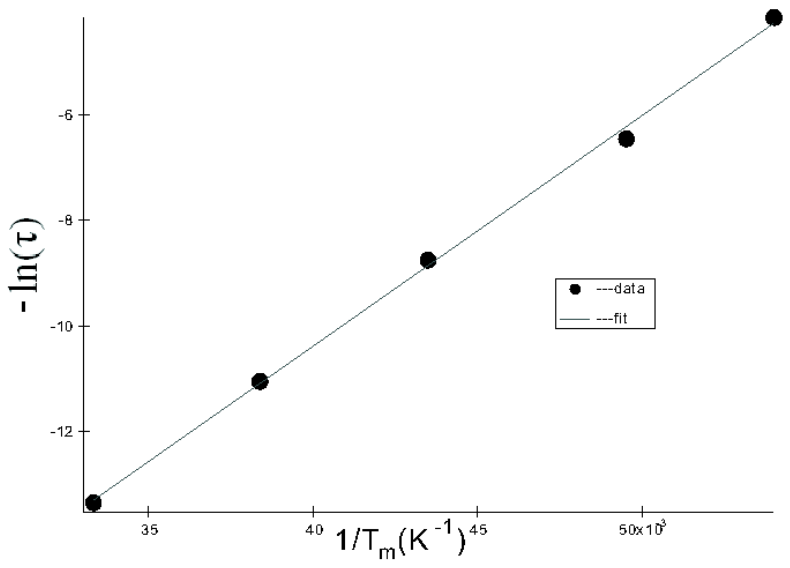

Figure 8.3: The $-\ln(\tau)$ vs. $1/T_m$ curve for BST (solid circles, the experiment data; thin line, the Arrhenius fits).

The peak shift to lower temperatures with decreasing frequency demonstrates that τ increases as T decreases, as expected from the Arrhenius law for the relaxation time:

$$\tau = \tau_0 \exp(\frac{\Delta}{K_B T}), \tag{8.3}$$

where τ_0 is the inverse of the attempt frequency, $\tau_0 = 1/f_0$, and Δ is the activation energy to orient the dipoles. An attempt was made to fit the data to the equation (converted from 8.3)

$$-\ln\tau = (\frac{\Delta}{K_B})(\frac{1}{T_m}) - \ln\tau_0. \tag{8.4}$$

In Figure 8.3, the data shows a linear curve fit. This result indicates that the Arrhenius Law (the relationship between relaxation time and temperature) is in quantitative agreement with our measurements. Because the Vogel-Fuchler Law 6.40 and equation 6.39 are expected to a nonlinear curve fit in Figure 8.3. The result of a linear curve fitting the data is: the slope is corresponding the activation energy, and the intercept is corresponding the attempt frequency. Finally, the activation energy and the attempt frequency are $\Delta = 37.8$ meV and $f_0 = 1.4$ THz, respectively.

The above analysis shows that the relationship of relaxation time and temperature follow the Arrenhius Law instead of Vogel-Fuchler Law (Normally it is a feature of relaxor). Next, we fitted our experimental data, which are indicated by markers in Figure 8.2. Whereas, the thin line is the curve fit based on equations 6.25 and 6.26. The relaxation time τ is based on the Arrhenius law (equation 8.4), and the activation energy and the characteristic relaxation time τ_0 are set as free variable parameters in these fits. The following table is the result of the best fit value for the activation energy and the characteristic relaxation time.

Table 8.1: The single relaxation fitted by the Debye model and Anhenius Law

ϵ^*	$parameters$	$10Hz$	10^2Hz	10^3Hz	10^4Hz	10^5Hz
Real part ε'	$\frac{\Delta}{K_B}$	327.26 K	342.95 K	448.31 K	420.12 K	449.78 K
	$\ln v_0$	19.68	20.39	23.40	21.94	21.71
	$\varepsilon_s - \varepsilon_\infty$	2.511 nF	2.497 nF	2.462 nF	2.503 nF	2.464 nF
Image part $\varepsilon"$	$\frac{\Delta}{K_B}$	351.33 K	355.53 K	445.50 K	446.74 K	441.67 K
	$\ln v_0$	23.06	24.28	27.68	28.54	28.08
	$\varepsilon_s - \varepsilon_\infty$	2.416 nF	2.353 nF	2.352 nF	2.411 nF	2.368 nF

Compared with the results fitted in Figure 8.3, the fitting parameters' fluctuations in Table 8.1 are large. Because our temperature dependence measurements are done on a fly and the sample is not in perfect thermal equilibrium with the thermometer, which is placed several centimeters away from the sample. We repeated the measurements of capacitance versus temperature, and found that the curves in Figure 8.3 can shift by approximately 2 K between different cool-downs. So the thermometer temperature is slightly different from the sample temperature when measuring on a fly. Nevertheless, the excellent fits of the curve shapes provide an adequate evidence for a single electric relaxation time scale in the sample.

8.3 Cole-Cole Plots with A Single Relaxation Time

As we mentioned in chapter 6, the Cole-Cole plot provides an elegant method of find whether a system has a single relaxation time. This plot also is used widely to find out the type of distribution function.

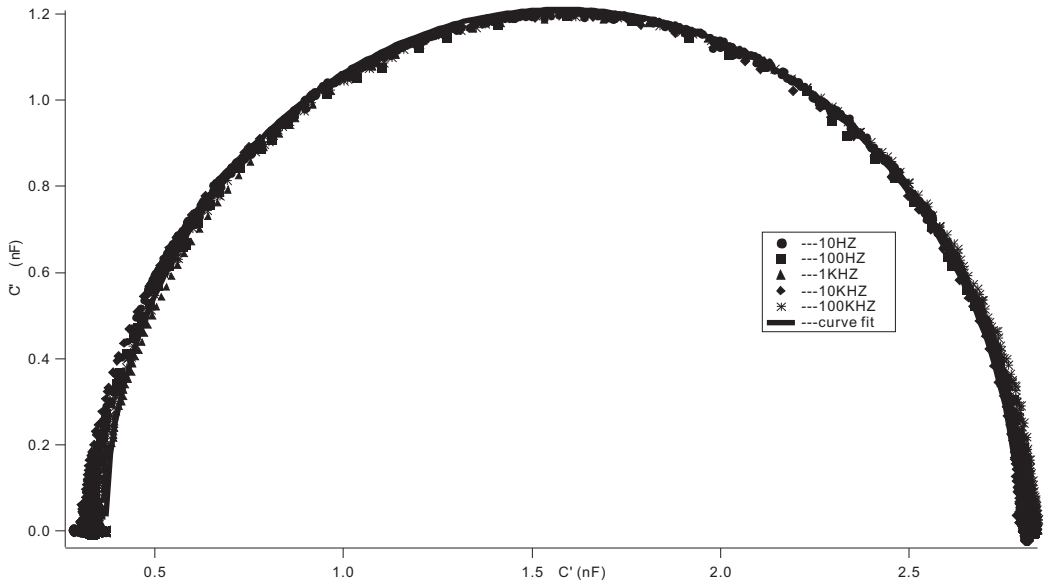

Figure 8.4: Cole-Cole plots (C' versus $C"$ is equivalent to ε' vs $\varepsilon"$) the experimental data (markers) at the different frequencies $(10, 10^2, 10^3, 10^4, 10^5)$ Hz in temperature range of $4.2 - 65K$ and the curve fit (solid line) from equation 6.27.

Here in Figure 8.4, we present our experimental data's Cole-Cole plot that displays out of phase capacitance versus in phase capacitance. All the experimental data are frequency independent and locate around a semicircle, as expected from equation 6.27. This means our experimental data is shown as dielectric relaxation with only a single relaxation time.

It is important to note that in the Cole-Cole plot, the data fall on a semicircle even if the sample temperature is slightly different from the thermometer temperature. We measured the real capacitance and imaginary capacitance at same time.

Thus, Figure 8.4 proves that only one relaxation time is present, in contrast to two [131] or multi relaxation time cases [132]. The data are fitted as shown by the solid black line based on equation 8.4. The fitting results are $C_s = 2.79nF$, $C_\infty = 0.37nF$.

8.4 The Polarization Versus Electric field Hysteresis Loops and Analysis

Hysteresis loops for the BST nanoparticles were measured in Sawyer-Tower circuit. To determine the electric polarization versus applied electric field, we drive the capacitor by a triangle wave form with amplitude 3 V and frequency 10^3 Hz. Each hysteresis loop

represents an average after 2000 runs, which were obtained over 2 second periods. At the same time, We read the temperature from the thermal meter located nearby the samples.

The Figure 8.5 displays the resulting polarization versus applied voltage. At temperatures close to the peak in C'' (for 1 KHz drive frequency, the temperature T_m is nearly 20 K) and in the temperature range above 210 K, hysteresis loops are obviously observed.

The P_r is the effective remanent polarization, E_c is the effective coercive field, and P_s is the effective spontaneous polarization. P_r , E_c , and P_s are not necessarily the same as the remanent polarization, the coercive field, and the saturation polarization, respectively, because the hysteresis loop could originate from the time delay in the electric response. In particular, if the electric relaxation time is comparable to the period of the triangle wave, the hysteresis will occur because of the time delayed electric response of the sample.

To analyze this result, we presented a new model. First, we assumed that the system has only a single relaxation time τ. When a dielectric is placed between charged plates, the polarization of the medium produces an electric field opposing the field of the charges on the plate. Then we can also obtain the time variation of the dipole moment $P(t)$ for the permittivity in an alternating field $E = V_{applied}(t)/D$, where D is the distance between the plates and V the potential difference between them.

From equation 6.18, we obtain the following linear differential equation:

$$\tau \frac{dP(t)}{dt} + P(t) = P_0 \cdot V_{applied}(t)/V_{max}, \tag{8.5}$$

where P_0=$(\varepsilon_s - \varepsilon_\infty) \cdot V_{max}/D$ is the equilibrium dipole moment at voltage V_{max}, and $V(t)$ is a triangle voltage wave with period $T = 2\pi/\omega$ and amplitude V_{max}. We take the Fourier Transform to both sides of equation 8.5, then obtain the $P(t)$:

$$P(t) = \sum_{n=1}^{\infty} \quad \frac{8P_0 \cdot (-1)^{n-1}}{\pi^2 \cdot (2n-1)^2 \left[1 + (2n-1)^2 \cdot \omega^2\tau^2\right]} \cdot \left[\sin\left[(2n-1)\omega t\right] - (2n-1)\omega\tau \cdot \cos\left[(2n-1)\omega t\right]\right] \tag{8.6}$$

$$V(t) = \sum_{n=1}^{\infty} \frac{8V_{max} \cdot (-1)^{n-1}}{\pi^2 \cdot (2n-1)^2} \sin[(2n-1) \cdot \omega t] \tag{8.7}$$

here ω is the driven angular frequency of the applied field $V(t)$. When $\omega t = 0$ and $\omega t = \pi/2$, we have:

$$P(0) = \sum_{n=1}^{\infty} \frac{8P_0(-1)^n \cdot \omega\tau}{\pi^2 \cdot (2n-1)\left[1 + (2n-1)^2\omega^2\tau^2\right]} \tag{8.8}$$

$$P(\frac{\pi}{2\omega}) = \sum_{n=1}^{\infty} \frac{8P_0}{\pi^2(2n-1)^2\left[1 + (2n-1)^2\omega^2\tau^2\right]} \tag{8.9}$$

where $P(0)$ and $P(\pi/2\omega)$ correspond to P_r and P_s shown in Figure 8.5, and we can obtain the values of relaxation time τ and dipole moment P_0 by solving equations 8.8 and 8.9. Then we obtain a single relaxation time model hysteresis loop $P(t)$ versus $E(t)$ by using equations 8.6 and 8.7.

At temperature below 200 K, we found the hysteresis loops are fitted very well by the above model based on a single relaxation time. However, when the temperature is above 210 K, the experimental hysteresis shrinks compared with the curve fit that is calculated within a single relaxation time approximation. Thus, a single Debye process is a good fit at low temperatures, where the capacitance is single valued function of temperature, but not above 200 K. The shrinkage of the data at 274 K compared with the single relaxation time model can be explained by a partial saturation of the electric polarization of the ferroelectric at large bias voltage.

The our BST nanoparticles are clearly ferroelectric because they displayed the hysteresis loops. The remanent polarization P_r at zero field is pretty small on order of nC/cm^2 in Figure 8.5, whereas the ideal BST bulk spontaneous polarization is around 24.5 $\mu C/cm^2$ (more than 20,000 times for the value of our BST particles). We also found that there is almost no spontaneous polarization for BST nanoparticles at low temperature in Figure 8.5, and those small hysteresis loops occurred due to the single electric relaxation response.

We have repeated these measurements in about ten BST nanoparticle samples and found that our results are quantitatively reproducible. We have also done measurements

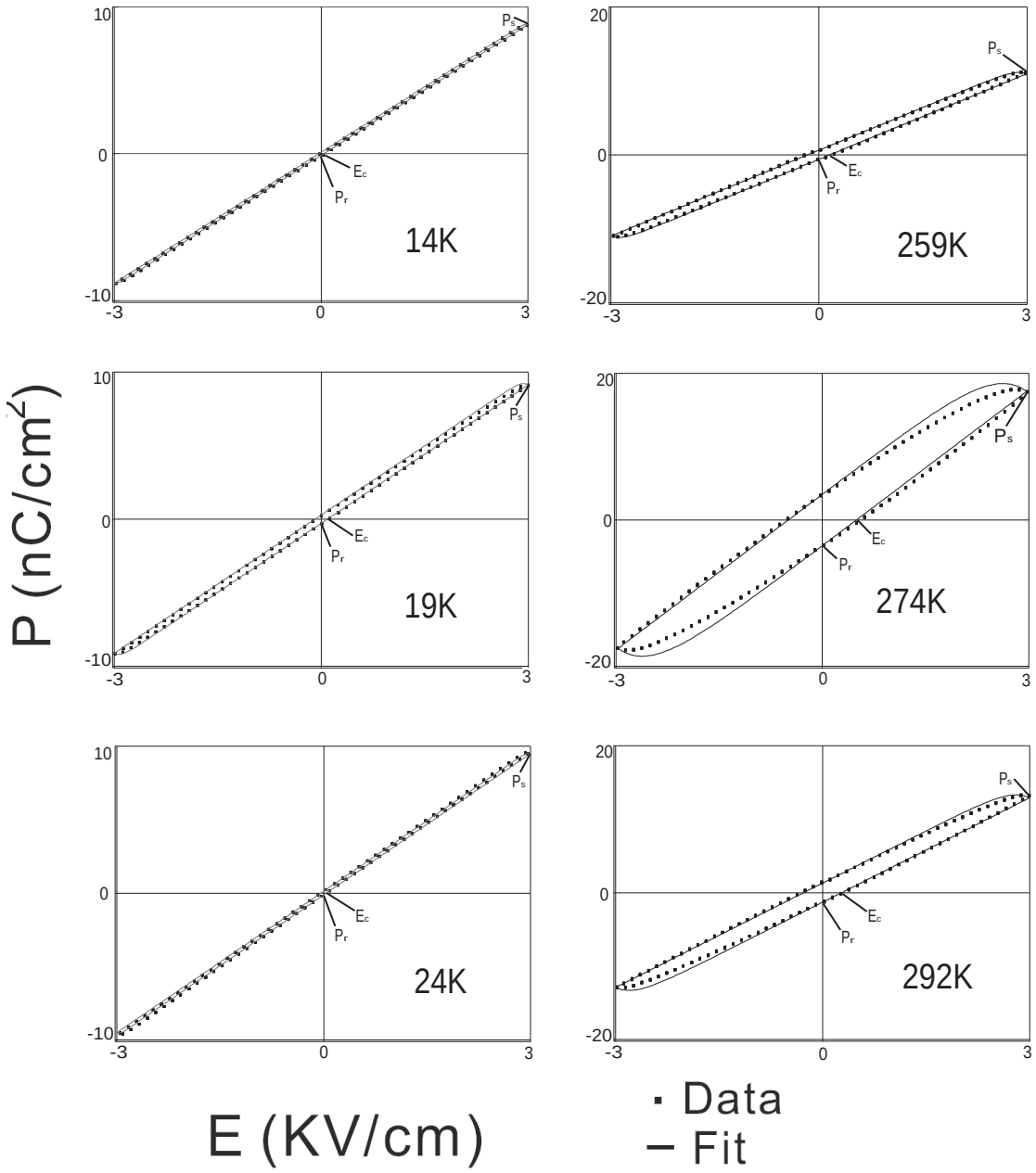

Figure 8.5: p versus $(E = V_{applied}/D)$ hysteresis loops of experimental data (solid squares) at various temperatures and applied by a $10^3 Hz$ triangle wave. p versus E hysteresis loops (thin line) as calculated from equations (2) and (3) with single relaxation times.

in BTA nanoparticle samples, and found similar results for the electric polarization at low temperatures with comparable relaxation time to that in BST nanoparticles.

CHAPTER IX

DISCUSSION

We had observed the unexpected relaxation behaviors by measuring the complex capacitance, which is equivalent to complex permittivity (ϵ^*), on the BST and $BaTiO_3$ (BTA) nanoparticles at frequencies between $10Hz$ and 10^5Hz, and in a temperature range of $4.2 - 340$ K. We find a clear anomaly in both real and imaginary parts of permittivity at low temperatures. This anomaly has a frequency and temperature dependence that can be fitted by the Debye theory [104] with only one relaxation time (τ). The relaxation time exhibits the Arrhenius Law. The activation energy is 37.83 meV and the attempt frequency is 1.4 THz. A single relaxation time at low temperatures is observed in $Ba_{0.77}Sr_{0.23}TiO_3$ nanoparticles at low temperatures.

At the low temperature (below 210 K), our experimental results are quite different with the those behaviors of bulk and film BST that have similar compositions. Recently, Bokov and Ye [82] had summarized the typical behaviors of relaxor ferroelectric in their review paper. There are four important property peculiarities distinguished from normal ferroelectrics crystals: First, they follow the Vogel-Fulcher law [118] instead of the Arrenius law for relaxation time-temperature dependence; second, they have non-Debye type dynamic dielectric response; third, they have non-ergodic behavior below the freezing temperature T_0 (i.e. properties depend on the cooling and heating regime); and fourth, they show a distribution of different property maxima in a Curie region ΔT around T_m, this is maximum of dielectric permittivity.

Zhang, et al., had done a series of similar studies [133, 134, 135] in large size grains, including studies of bulk ceramic $Ba_{0.7}Sr_{0.3}TiO_3$ (the composition is similar to our sample) with different grain size (1860 nm, 1100 nm, 370 nm, 223 nm, 198 nm). They found some size effects on the dielectric properties with temperature changes from 10 to 400 K, generally that the dielectric constant and ferroelectric tendencies are suppressed with decreasing grain

size.

The summation is that, clearly, all their results showed non-Debye type response and non-Arrhenius form in relaxation time, which is totally different from our results below 200 K. In addition, the temperature dependence of the dielectric constant did not show any measurable thermal hysteresis with heating and cooling, whereas we find thermal hysteresis in our samples when the temperatures are above 210 K. In range of 5 nm to 100 nm, recently Chen et al., [136] found that the BST films exhibited size effects with voltage and thickness dependences at room temperature. But they didn't study the temperature dependences. As for the 100 nm thickness BST film, Shaw et al., [137] work shows that the dielectric constant has no sharp peak, which is very different dielectric response type with our result.

There are also some other works [96, 97, 138] on size effects in BST that present the variations of the dielectric constant as a function of temperature. The cause of size effects in ferroelectrics are complicated, and it is often difficult to separate true size effects from the other factors that change with film thickness or particle size, such as film microstructure and defect chemistry or constraints such as electrode interaction and space change layers and so on. None of these studies found a single relaxation time.

In our case, it is surprising that the electric relaxation in BST nanoparticle powders at low temperature has only one relaxation time, because higher temperatures indicate relaxor ferroelectric behavior with a broad distribution of relaxation times. This broad distribution is attributed to the variation in the local Neel temperature and variation in the local environments of the correlated electric dipoles [113]. At low temperatures, however, when the correlated dipoles are frozen into the ferroelectric state, our data shows that there remains a significant fraction of dipoles that are responsive to the changes in the applied electric field. These free dipoles are characterized by only one relaxation time. Since our sample has significant disorder, which is due to small crystallite size and local compositional variation, the relaxation process of these free dipoles must be insensitive to the disorder.

The attempt frequency $f_0 \sim 1THz$ is on the order of optical phonon frequency, which suggests the free dipoles must be ions, not electrons. The energy barrier for tunnelling between sites (37.8 mV) is small compared to the ferroelectric free energy of the nanoparticles,

which is proportional to the nanoparticle volume. 37.8 meV could be an energy barrier to move a single titanium ion between two energetically degenerate positions.

A single relaxation time shows that activation energy does not vary among different ions and it is reproducible among samples. This shows that the activation energy must be set by the parameters of the crystal structure of BST, and not random defects.

In our samples, one possibility would be that the free dipoles are located on the nanoparticle surfaces, because the surface to volume ratio is large. But this explanation is problematic because different Ti ions on the surfaces would experience different crystal fields, so one would expect a broad range of energy barriers Δ. The average surface energy of the ideal BTA surfaces is around 1.358 eV per surface unit cell. This value is much greater than the energy barrier (0.038 eV) we measured. The surface energy of BST should be comparable to the value of BTA. Thus, the surface component of the dipole moment is relatively insensitive to the surface relaxation.

We suggest that these free dipoles are produced by a frustration effect, which prevents locking into the ferroelectric order. The physical origin of this frustration is not clear, but the small particle size must be playing an important role since the effect was not reported in thin films or bulk.

We propose that the electric frustration occurs because the ferroelectric state in nanometer scale particles is fundamentally different from ferroelectricity in bulk [139, 140]. Zero dimensional ferroelectrics were shown to display phase-transitions that are unknown in bulk [140], and we suspect that this could lead to a frustrated ferroelectric ground state, analogous to the frustration in frustrated antiferromagnets. This frustration would cause the Ti ions to remain responsive to the applied electric field at temperatures much below the Neel temperature. Our measurements show that the the energy barrier for the electric response in this state does not vary among different ions and it is reproducible among samples. This suggests that the barrier is set by the parameters of the crystal structure of BST, and therefore it should be calculable from the first principle calculations. More theoretical work is needed to explain our measurements at low temperatures. Nevertheless, our results show that below some particle size, there is no true ferroelectric order, as expected.

As for the high temperature (above 210 K), the permittivity exhibits a broad range of relaxation times typically found in relaxor ferroelectrics. One possible causes of this broad maximum in permittivity versus temperature above 210 K is: The compositional disorder, i.e., the disorder in arrangement of different ions (e.g., Ba and Sr) on the crystallographically equivalent sites, this disorder is the common characteristic of relaxors such as BST, because it is difficult to maintain homogeneity in the cation distribution during the synthesis and processing. It is well known that curie temperature (T_c) are dependent of the the cation distribution. When the temperature changes, the thermal motion in different T_c BST nanoparticles can result in broadened phase transition, and suppression in the peak permittivity. As a result, a T_c shift, as well as the broadening and depression of the permittivity maximum (there are also a lot of smaller peaks between 210 K and 340 K) were observed due to the compositional disorder.

Another possible interpretation is: the phenomena of this broad maximum in permittivity can result in grain size effect, because the properties of ferroelectric are always associated with the special structure and length scales. The main cause of this decrease in permittivity is thought to be the presence of a low permittivity layer at the grain boundaries. Where grain boundaries exist parallel to the electrodes and hence can act in series with the bulk of the grain, the permittivity can be greatly reduced and depends strongly on nanoparticles sizes.

In addition, we find thermal hysteresis in our samples when the temperatures are above 210 K. In some literature, this phenomena is called as the nonergodic relaxor state, which can be irreversibly transformed into a FE state by a strong enough external electric field. This is also an important characteristic of relaxors which distinguished them from typical dipole glasses. When the temperature (below 200 K) are all below those T_c of nanoparticles, a spontaneous phase transition happened and thus the nonergodic state does not exist.

9.1 Conclusion

The purpose of this part is trying to understand the factors that may influence the properties of ferroelectric materials at small dimensions. The XRD results indicated that BST

and BTA are oxide ferroelectrics with structures based on the perovskite structure. The SEM and TEM images showed that our BST nanoparticles sizes distribution is in the range of $5-100\ nm$. Though the whole physical picture is unclear to us, we still can conclude that there is a characteristic size in this size range $5-100\ nm$ and indicating that this fundamental limit of ferroelectric memory occurs above 5 nm diameter. This characteristic value is a very important parameter for the future development of the application in nanoscale electronic devices, such as high-density dynamic random access memories (DRAM).

From the results of the electric hysteresis loops, we found no permanent polarization of the free dipoles in our samples when the temperature is below 210 K, whereas a huge thermal hysteresis was observed in our samples when the temperatures are above 210 K. This behavior is explained as originating from two types of particles, larger particles are ferroelectric, and they produce the relaxor behaviors above 210 K. Smaller particles are not ferroelectric, exhibit no permanent polarization, and display a simple Debye relaxation at low temperature.

APPENDIX A

LIST OF SYMBOLS

h	Planck Constant (6.62×10^{-34} Js)
k_B	Boltzman constant(1.38×10^{-23} J/K)
nm	nanometer (10^{-9} m)
$\mathring{A}$	Unit of length, Angstrom (10^{-10}m)
Ω	Ohm
K	Kelvin
T	Teslas
Torr	Unit of pressure, equal to 133.32 Pa
e	Charge of an electron
eV	electron volt
G	Differential conductance
I	Current
R	Resistance
U	Potential Energy
V	Bias Voltage
τ	Relaxation Time
f	Frequency
T	Temperature
t	Time
T_1	longitudinal spin relaxation time
T_2	spin dephasing time
T_2^*	spin dephasing time of ensemble spins
M	Magnetization

DOS	Density Of State
P	Spin Polarization
T_c	Critical Temperature
MTJ	Magnetic Tunnel Junction
SDT	Spin-Dependent Tunnelling
DRAM	Dynamic random access memories
FM/I/FM	Ferromagnetic Insulator Ferromagnetic
AP	Antiparallel
TMR	Tunnel Magneto Resistance
GMR	Giant Magnetoresistance
PMMA	PolyMethyl MethAcrylate
IPA	Isopropanol
SCCM	unit of flow, standard cubic centimeter per minute
BST	Barium Strontium Titanate ($Ba_{1-x}Sr_xTiO_3$)
BTA	Barium Titanate ($BaTiO_3$)
CCVD	Combustion Chemical Vapor Condensation
SEM	Scanning Electron Microscopy
XRD	X-Ray Diffraction
TEM	Transmission Electron Microscopy

APPENDIX B

DEBYE RELAXATION EQUIVALENT CIRCUITS

For the plate capacitor, when a capacitor is filled with a dielectric its static capacitance is, in practical units,

$$C = \varepsilon\varepsilon_0 \frac{A}{d} = \varepsilon C_0 \tag{B.1}$$

The capacitance under dynamic conditions may be expressed as the complex capacitance $C^*(\omega)$, which is in term of $\varepsilon^*(\omega)$ (the dynamic dielectric).

$$C^*(\omega) = \varepsilon^*(\omega) C_0 \tag{B.2}$$

or

$$\varepsilon^*(\omega) = C^*(\omega)/C_0 \tag{B.3}$$

The complex inpedance $Z^*(\omega)$ gives:

$$Z^*(\omega) = \frac{1}{i\omega C^*(\omega)} \tag{B.4}$$

In other form is

$$C^*(\omega) = \frac{1}{i\omega Z^*(\omega)} \tag{B.5}$$

In Figure (B.1) shows a combination of two capacitors and a resistor, where the branch containing C_1 and R_1 is in series, and they are parallel to capacitor C_∞. We will see that this is a equivalent circuit, which is analogue of the most famous Debye relaxation of a dielectric material.

The total inpedance (Figure B.1) in representation:

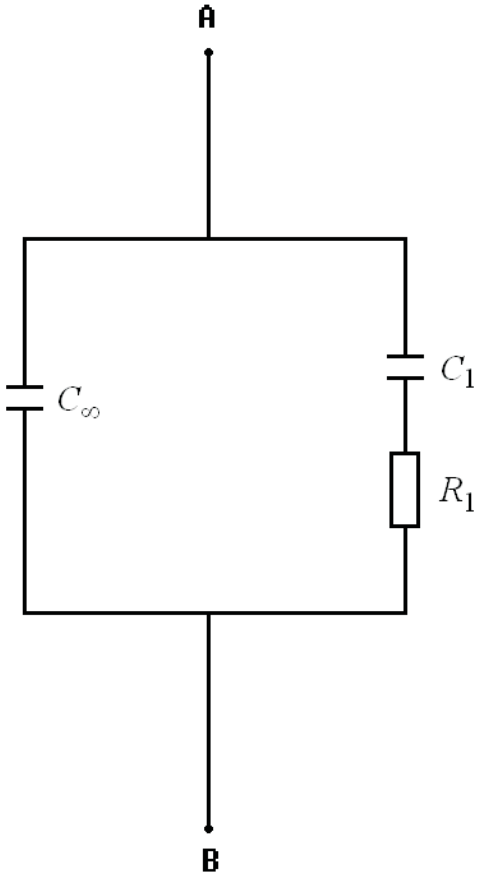

Figure B.1: The equivalent circuit of Debye relaxation with a single relaxation time

$$\frac{1}{z^*(\omega)_{total}} = \frac{1}{(i\omega C_\infty)^{-1}} + \frac{1}{R_1 + (i\omega C_1)^{-1}} \tag{B.6}$$

The total complex capacitance in equation (B.5) gives

$$C^*(\omega) = \frac{1}{i\omega z^*(\omega)_{total}} = C_\infty + \frac{C_1}{1 + i\omega\tau_1} \tag{B.7}$$

where

$$\tau_1 = R_1 C_1 \tag{B.8}$$

The real and imaginary parts of the complex capacitance $C^*(\omega)$ are given by

$$C'(\omega) = C_\infty + \frac{C_1}{1+\omega^2\tau_1^2} \tag{B.9}$$

$$C''(\omega) = \frac{C_1\omega\tau}{1+\omega^2\tau_1^2} \tag{B.10}$$

Then equation B.3 for the complex dielectric gives

$$\varepsilon^*(\omega) = \frac{C_\infty}{C_0} + \frac{C_1/C_0}{1+i\omega\tau_1} \tag{B.11}$$

If we let $\varepsilon_\infty = C_\infty/C_0$ and $\varepsilon_s - \varepsilon_\infty = C_1/C_0$, then the equation (B.11) will be in Debye relaxation form:

$$\varepsilon^*(\omega) = \varepsilon_\infty + \frac{\varepsilon_s - \varepsilon_\infty}{1+i\omega\tau_1} \tag{B.12}$$

Similarly, in the Debye relaxation with Muti-relaxation times case, the equivalent circuit was shown in Figure (B.2), where multi-branches where each branch contains resistance and capacitor in series. The equivalent complex capacitance in circuit (Figure B.2) gives

$$C'(\omega) = C_\infty + \frac{C_1}{1+i\omega\tau_1} + \frac{C_2}{1+i\omega\tau_2} + \cdots + \frac{C_n}{1+i\omega\tau_n} \tag{B.13}$$

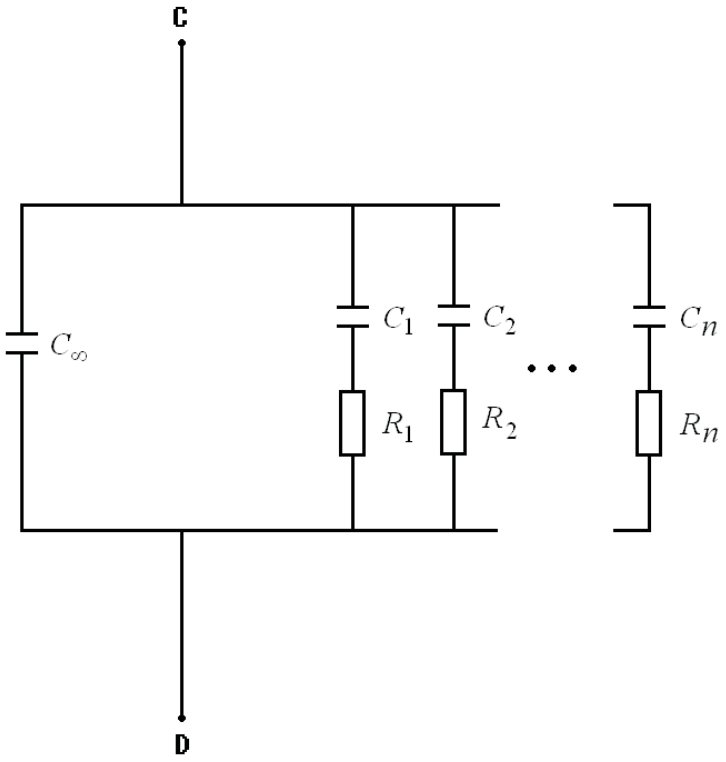

Figure B.2: The equivalent circuit of Debye relaxation with multi-relaxation times

APPENDIX C

THE GENERAL DISTRIBUTION FUNCTIONS

Most dielectrics are linear when the electric field strength is not too high. In dielectric relaxation response, the superposition principle is still valid, i.e. the polarization at a time to due to an a electric field with a time-dependence that can be written as a sum $E(t) + E'(t)$, is given by the sum of the polarization's $P(t_0)$ and $P'(t_0)$ due to the $E(t)$ and $E'(t)$ separately. The expression of polarization $P(t)$ is much convenient in form decay function of the polarization $\Psi(t)$.

$$P(t) = P(0)\Psi(t) = \chi E(0)\Psi(t), \tag{C.1}$$

The general expression for the polarization $P(t)$ can be written in the integral form in the case of a time-dependent Maxwell field.

$$P(t) = \chi \int_{-\infty}^{t} E(t')[-\frac{\partial \Psi(t-t')}{\partial t}]dt' \tag{C.2}$$

$$= \chi \int_{-\infty}^{t} E(t')\dot{\Psi}(t-t')dt', \tag{C.3}$$

Where, $\dot{\Psi}(t)$ is pulse-response function of polarization. Applying to the left and right parts of equation C.2 the Laplace transform and taking into account the theorem of deconvolution, we can obtain:

$$P^*(\omega) = \epsilon^*(\omega)E^*(\omega), \tag{C.4}$$

Where

$$\epsilon^*(s) = \int_0^\infty \dot{\Psi}(t)e^{-st}dt \tag{C.5}$$

$$\equiv L(\dot{\Psi}(t)) \tag{C.6}$$

$$= \int_0^\infty \frac{G(\tau)d\tau}{1+s\tau} \tag{C.7}$$

The variable s is complex and for the purposes of the present application can best be interpreted as $s = \gamma + i\omega$; $\gamma \to 0$ and we'll write instead of s in all Laplace transforms $i\omega$. The function $G(\tau)$ in this expression is

$$G(\tau) = \frac{y(\tau)}{\varepsilon_s - \varepsilon_\infty}, \tag{C.8}$$

The Laplace transform and the functions defined above appear in more mathematical literature of dielectric relaxation in various ways.

$$\dot{\Psi}(t) = L^{-1}(\epsilon^*(s)), \tag{C.9}$$

defines the inverse Laplace transform. The integral in equation C.1 is frequently expressed in term of a variable

$$p = ln(\frac{\tau}{\tau_0}), \tag{C.10}$$

where τ_0 is a positive constant. Now a distribution function $F(\tau)$ or F(p) is defined by

$$F(\tau) \equiv \tau G(\tau), \tag{C.11}$$

where

$$\int_{-\infty}^\infty F(p)d(p) = \int_0^\infty G(\tau)d\tau = 1, \tag{C.12}$$

while

$$\epsilon^*(p) = \int_{-\infty}^\infty \frac{F(\tau)}{1+s\tau}dp. \tag{C.13}$$

if real and imaginary parts are separated in equation C.7 or C.12 and we put $p = i\omega$

$$\epsilon^*(i\omega) = \epsilon'(\omega) - i\epsilon''(\omega) \tag{C.14}$$

$$= \frac{1}{\varepsilon_s - \varepsilon_\infty}(\varepsilon'(\omega) - \varepsilon''(\omega)) \tag{C.15}$$

where

$$\epsilon'(\omega) = \int_0^\infty \frac{G(\tau)d\tau}{1+\omega^2\tau^2} \tag{C.16}$$

$$= \int_0^\infty \frac{F(\tau)d(ln\tau)}{1+\omega^2\tau^2} \tag{C.17}$$

while

$$\epsilon''(\omega) = \int_0^\infty \frac{\omega\tau G(\tau)d\tau}{1+\omega^2\tau^2} \tag{C.18}$$

$$= \int_0^\infty \frac{\omega\tau F(\tau)d(ln\tau)}{1+\omega^2\tau^2} \tag{C.19}$$

REFERENCES

[1] L. D. Awschalom D.D. and S. N., *Semiconductor Spintronics and Quantum Computation.* (Springer Verlag, 2002).

[2] J. M. Elzerman, R. Hanson, L. H. W. van Beveren, B. Witkamp, L. M. K. Vandersypen, and L. P. Kouwenhoven, "Single-shot read-out of an individual electron spin in a quantum dot," *Nature* **430**, 431 (2004).

[3] O. Agam, N. S. Wingreen, B. L. Altshuler, D. C. Ralph, and M. Tinkham, "Chaos, interactions, and nonequilibrium effects in the tunneling resonance spectra of ultrasmall metallic particles," *Physical Review Letters* **78**, 1956 (1997).

[4] O. Auciello, J. F. Scott, and R. Ramesh, "The physics of ferroelectric memories," *Physics Today* **51**, 22 (1998).

[5] G. W. Dietz, M. Schumacher, R. Waser, S. K. Streiffer, C. Basceri, and A. I. Kingon, "Leakage currents in $Ba_{0.7}Sr_{0.3}TiO_3$ thin films for ultrahigh-density dynamic random access memories," *Journal of Applied Physics* **82**, 2359 (1997).

[6] J. F. Scott and C. A. P. Dearaujo, "Ferroelectric memories," *Science* **246**, 1400 (1989).

[7] R. Nakao, K. Ishizumi, I. Takahashi, H. Terauchi, Y. Hayafuji, and K. Miura, "Critical thickness for ferroelectricity of BaTiO3 by first-principles calculations," *Applied Physics Letters* **86**, 222901 (2005).

[8] G. A. Prinz, "Device physics magnetoelectronics," *Science* **282**, 1660 (1998).

[9] S. A. Wolf, D. D. Awschalom, R. A. Buhrman, J. M. Daughton, S. von Molnar, M. L. Roukes, A. Y. Chtchelkanova, and D. M. Treger, "Spintronics: A spin-based electronics vision for the future," *Science* **294**, 1488 (2001).

[10] R. Meservey, P. M. Tedrow, and P. Fulde, "Magnetic field splitting of quasiparticle states in superconducting aluminum films," *Physical Review Letters* **25**, 1270 (1970).

[11] P. M. Tedrow and R. Meservey, "Spin-dependent tunneling into ferromagnetic nickel," *Physical Review Letters* **26**, 192 (1971).

[12] P. M. Tedrow and R. Meservey, "Spin polarization of electrons tunneling from films of fe, co, ni, and gd," *Physical Review B* **7**, 318 (1973).

[13] M. Julliere, "Tunneling between ferromagnetic-films," *Physics Letters A* **54**, 225 (1975).

[14] R. J. Elliott, "Theory of the effect of spin-orbit coupling on magnetic resonance in some semiconductors," *Physical Review* **96**, 266 (1954).

[15] M. I. Dyakonov and V. I. Perel, "Spin orientation of electrons associated with interband absorption of light in semiconductors," *Soviet Physics Jetp-Ussr* **33**, 1053 (1971).

[16] G. A. A. Bir and G. Pikus, *Sov. Phys. JETP* **42**, 705 (1976).

[17] J. M. Kikkawa, I. P. Smorchkova, N. Samarth, and D. D. Awschalom, "Room-temperature spin memory in two-dimensional electron gases," *Science* **277**, 1284 (1997).

[18] J. A. Gupta, D. D. Awschalom, X. Peng, and A. P. Alivisatos, "Spin-coherence in semiconductor quantum dots (vol 59, pg R10421, 1999)," *Physical Review B* **60**, 8394 (1999).

[19] D. Loss and D. P. Divincenzo, "Quantum computation with quantum dots," *Physical Review A* **57**, 120 (1998).

[20] G. Burkard, H. A. Engel, and D. Loss, "Spintronics and quantum dots for quantum computing and quantum communication," *Fortschritte Der Physik-Progress of Physics* **48**, 965 (2000).

[21] A. V. Khaetskii and Y. V. Nazarov, "Spin relaxation in semiconductor quantum dots," *Physical Review B* **61**, 12639 (2000).

[22] A. V. Khaetskii and Y. V. Nazarov, "Spin-flip transitions between zeeman sublevels in semiconductor quantum dots," *Physical Review B* **6412**, 125316 (2001).

[23] T. Fujisawa, D. G. Austing, Y. Tokura, Y. Hirayama, and S. Tarucha, "Allowed and forbidden transitions in artificial hydrogen and helium atoms," *Nature* **419**, 278 (2002).

[24] R. Hanson, B. Witkamp, L. M. K. Vandersypen, L. H. W. van Beveren, J. M. Elzerman, and L. P. Kouwenhoven, "Zeeman energy and spin relaxation in a one-electron quantum dot," *Physical Review Letters* **91**, 196802 (2003).

[25] E. I. Rashba, "Theory of electrical spin injection: Tunnel contacts as a solution of the conductivity mismatch problem," *Physical Review B* **62**, R16267 (2000).

[26] M. Johnson and R. H. Silsbee, "Interfacial charge-spin couplinginjection and detection of spin magnetization in metals," *Physical Review Letters* **55**, 1790 (1985).

[27] F. J. Jedema, A. T. Filip, and B. J. van Wees, "Electrical spin injection and accumulation at room temperature in an all-metal mesoscopic spin valve," *Nature* **410**, 345 (2001).

[28] Y. Yafet, "G-factors and spin-lattice relaxation of conduction electrons," *Solid State Physics-Advances in Research and Applications* **14**, 1 (1963).

[29] J. Fabian and S. Das Sarma, "Spin relaxation of conduction electrons in polyvalent metals: Theory and a realistic calculation," *Physical Review Letters* **81**, 5624 (1998).

[30] J. Fabian and S. Das Sarma, "Band-structure effects in the spin relaxation of conduction electrons (invited)," *Journal of Applied Physics* **85**, 5075 (1999).

[31] J. Fabian and S. Das Sarma, "Phonon-induced spin relaxation of conduction electrons in aluminum," *Physical Review Letters* **83**, 1211 (1999).

[32] F. J. Jedema, H. B. Heersche, A. T. Filip, J. J. A. Baselmans, and B. J. van Wees, "Electrical detection of spin precession in a metallic mesoscopic spin valve," *Nature* **416**, 713 (2002).

[33] M. M. Deshmukh, E. Bonet, A. N. Pasupathy, and D. C. Ralph, "Equilibrium and nonequilibrium electron tunneling via discrete quantum states," *Physical Review B* **65**, 073301 (2002).

[34] J. Konig and J. Martinek, "Interaction-driven spin precession in quantum-dot spin valves," *Physical Review Letters* **90**, 166602 (2003).

[35] C. D. Chen, Y. D. Yao, S. F. Lee, and J. H. Shyu, "Magnetoresistance study in Co-Al-Co and Al-Co-Al double tunneling junctions," *Journal of Applied Physics* **91**, 7469 (2002).

[36] K. Ono, H. Shimada, S. Kobayashi, and Y. Ootuka, "Magnetoresistance of Ni/NiO/Co small tunnel junctions in Coulomb blockade regime," *Journal of the Physical Society of Japan* **65**, 3449 (1996).

[37] K. Ono, H. Shimada, and Y. Ootuka, "Enhanced magnetic valve effect and magneto-Coulomb oscillations in ferromagnetic single electron transistor," *Journal of The Physical Society of Japan* **66**, 1261 (1997).

[38] J. Barnas and A. Fert, "Effects of spin accumulation on single-electron tunneling in a double ferromagnetic microjunction," *Europhysics Letters* **44**, 85 (1998).

[39] J. Barnas and A. Fert, "Magnetoresistance oscillations due to changing effects in double ferromagnetic tunnel junctions," *Physical Review Letters* **80**, 1058 (1998).

[40] S. Takahashi and S. Maekawa, "Effect of Coulomb blockade on magnetoresistance in ferromagnetic tunnel junctions," *Physical Review Letters* **80**, 1758 (1998).

[41] A. Brataas, Y. V. Nazarov, J. Inoue, and G. E. W. Bauer, "Spin accumulation in small ferromagnetic double-barrier junctions," *Physical Review B* **59**, 93 (1999).

[42] K. Majumdar and S. Hershfield, "Magnetoresistance of the double-tunnel-junction Coulomb blockade with magnetic metals," *Physical Review B* **57**, 11521 (1998).

[43] A. Brataas, Y. V. Nazarov, J. Inoue, and G. E. W. Bauer, "Non-equilibrium spin accumulation in ferromagnetic single-electron transistors," *European Physical Journal B* **9**, 421 (1999).

[44] A. N. Korotkov and V. I. Safarov, "Nonequilibrium spin distribution in a single-electron transistor," *Physical Review B* **59**, 89 (1999).

[45] J. Martinek, J. Barnas, G. Michalek, B. R. Bulka, and A. Fert, "Spin effects in single-electron tunneling in magnetic junctions," *Journal of Magnetism and Magnetic Materials* **207**, L1 (1999).

[46] J. Barnas, J. Martinek, G. Michalek, B. R. Bulka, and A. Fert, "Spin effects in ferromagnetic single-electron transistors," *Physical Review B* **62**, 12363 (2000).

[47] W. Kuo and C. D. Chen, "Gate-controlled spin polarized current in ferromagnetic single electron transistors," *Physical Review B* **65**, 104427 (2002).

[48] H. Imamura, Y. Utsumi, and H. Ebisawa, "Parity effect and tunnel magnetoresistance of ferromagnet/superconductor/ferromagnet single-electron tunneling transistors," *Physical Review B* **66**, 054503 (2002).

[49] J. Martinek, J. Barnas, A. Fert, S. Maekawa, and G. Schon, "Transport in magnetic nanostructures in the presence of Coulomb interaction," *Journal of Applied Physics* **93**, 8265 (2003).

[50] M. M. Deshmukh and D. C. Ralph, "Using single quantum states as spin filters to study spin polarization in ferromagnets," *Physical Review Letters* **89**, 266803 (2002).

[51] M. A. Kastner, "Artificial atoms," *Physics Today* **46**, 24 (1993).

[52] R. C. Ashoori, "Electrons in artificial atoms," *Nature* **379**, 413 (1996).

[53] L. Kouwenhoven, L.P. Sohn and S. G., *Mesoscopic Electron Transport* (p. 549, Elsevier and Amsterdam, 1997).

[54] W. P. Halperin, "Quantum size effects in metal particles," *Rev. Mod. Phys.* **58**, 533 (1986).

[55] J. Von Delft and D. C. Ralph, "Spectroscopy of discrete energy levels in ultrasmall metallic grains," *Physics Reports-Review Section of Physics Letters* **345**, 62 (2001).

[56] C. T. Black, D. C. Ralph, and M. Tinkham, "Spectroscopy of the superconducting gap in individual nanometer-scale aluminum particles," *Physical Review Letters* **76**, 688 (1996).

[57] M. M. Deshmukh, S. Kleff, S. Gueron, E. Bonet, A. N. Pasupathy, J. von Delft, and D. C. Ralph, "Magnetic anisotropy variations and nonequilibrium tunneling in a cobalt nanoparticle," *Physical Review Letters* **8722**, 226801 (2001).

[58] S. Gueron, M. M. Deshmukh, E. B. Myers, and D. C. Ralph, "Tunneling via individual electronic states in ferromagnetic nanoparticles," *Physical Review Letters* **83**, 4148 (1999).

[59] S. Adam, M. L. Polianski, X. Waintal, and P. W. Brouwer, "Magnetic-field dependence of energy levels in ultrasmall metal grains," *Physical Review B* **66**, 195412 (2002).

[60] D. Davidovic and M. Tinkham, "Spectroscopy, interactions, and level splittings in an nanoparticles," *Physical Review Letters* **83**, 1644 (1999).

[61] J. R. Petta and D. C. Ralph, "Measurements of strongly anisotropic g factors for spins in single quantum states," *Physical Review Letters* **89**, 156802 (2002).

[62] J. R. Petta and D. C. Ralph, "Studies of spin-orbit scattering in noble-metal nanoparticles using energy-level tunneling spectroscopy," *Physical Review Letters* **87**, 266801 (2001).

[63] D. G. Salinas, S. Gueron, D. C. Ralph, C. T. Black, and M. Tinkham, "Effects of spin-orbit interactions on tunneling via discrete energy levels in metal nanoparticles," *Physical Review B* **60**, 6137 (1999).

[64] P. W. Brouwer, X. Waintal, and B. I. Halperin, "Fluctuating spin g-tensor in small metal grains," *Physical Review Letters* **85**, 369 (2000).

[65] K. A. Matveev, L. I. Glazman, and A. I. Larkin, "g-factors of discrete levels in nanoparticles," *Physical Review Letters* **85**, 2789 (2000).

[66] R. J. Epstein, D. T. Fuchs, W. V. Schoenfeld, P. M. Petroff, and D. D. Awschalom, "Hanle effect measurements of spin lifetimes in InAs self-assembled quantum dots," *Applied Physics Letters* **78**, 733 (2001).

[67] M. Braun, J. Konig, and J. Martinek, "Hanle effect in transport through quantum dots coupled to ferromagnetic leads," *Europhysics Letters* **72**, 294 (2005).

[68] H. R. Zeller and I. Giaever, "Tunneling, zero-bias anomalies, and small superconductors," *Physical Review* **181**, 789 (1969).

[69] D. C. Ralph, C. T. Black, and M. Tinkham, "Spectroscopic measurements of discrete electronic states in single metal particles," *Physical Review Letters* **74**, 3241 (1995).

[70] Z. W. Zhao, B. K. Tay, C. Q. Sun, and V. Ligatchev, "Oxygen lone-pair states near the valence band edge of aluminum oxide thin films," *Journal of Applied Physics* **95**, 4147 (2004).

[71] D. V. Averin and K. K. Likharev, *Mesoscopic Phenomena in Solids* (p169. Elsevier and Amsterdam, 1991).

[72] J. Unguris, D. Tulchinsky, M. H. Kelley, J. A. Borchers, J. A. Dura, C. F. Majkrzak, S. Y. Hsu, R. Loloee, W. P. Pratt, and J. Bass, "Magnetic depth profiling Co/Cu multilayers to investigate magnetoresistance (invited)," *Journal of Applied Physics* **87**, 6639 (2000).

[73] A. Hubert and R. Schafer, *Domain Walls* (Springer- Verlag, 1998).

[74] H. Park, A. K. L. Lim, A. P. Alivisatos, J. Park, and P. L. McEuen, "Fabrication of metallic electrodes with nanometer separation by electromigration," *Applied Physics Letters* **75**, 301 (1999).

[75] A. C. Johnson, J. R. Petta, J. M. Taylor, A. Yacoby, M. D. Lukin, C. M. Marcus, M. P. Hanson, and A. C. Gossard, "Triplet-singlet spin relaxation via nuclei in a double quantum dot," *Nature* **435**, 925 (2005).

[76] S. Zhang, P. M. Levy, A. C. Marley, and S. S. P. Parkin, "Quenching of magnetoresistance by hot electrons in magnetic tunnel junctions," *Physical Review Letters* **79**, 3744 (1997).

[77] F. J. Jedema, M. S. Nijboer, A. T. Filip, and B. J. van Wees, "Spin injection and spin accumulation in all-metal mesoscopic spin valves," *Physical Review B* **67**, 085319 (2003).

[78] J. R. Petta, S. K. Slater, and D. C. Ralph, "Spin-dependent transport in molecular tunnel junctions," *Physical Review Letters* **93**, 136601 (2004).

[79] S. Tarucha, D. G. Austing, T. Honda, R. J. vanderHage, and L. P. Kouwenhoven, "Shell filling and spin effects in a few electron quantum dot," *Physical Review Letters* **77**, 3613 (1996).

[80] E. Y. Tsymbal, A. Sokolov, I. F. Sabirianov, and B. Doudin, "Resonant inversion of tunneling magnetoresistance," *Physical Review Letters* **90**, 186602 (2003).

[81] L. Zhang, W. Zhong, P. Wang, C.L.and Zhang, and Y. Wang, "Dielectric properties of $Ba_{0.7}Sr_{0.3}TiO_3$ ceramics with different grain size," *Physica Status Solidi A-Applied Research* **168**, 543 (1998).

[82] A. A. Bokov and Z. G. Ye, "Recent progress in relaxor ferroelectrics with perovskite structure," *Journal of Materials Science* **41**, 31 (2006).

[83] M. W. Cole, P. C. Joshi, M. H. Ervin, M. C. Wood, and R. L. Pfeffer, "The influence of Mg doping on the materials properties of $Ba_{1-x}Sr_xTiO_3$ thin films for tunable device applications," *Thin Solid Films* **374**, 34 (2000).

[84] T. Horikawa, N. Mikami, T. Makita, J. Tanimura, M. Kataoka, K. Sato, and M. Nunoshita, "Dielectric-properties of $(Ba, Sr)TiO_3$ thin-films deposited by RF-sputtering," *Japanese Journal of Applied Physics Part 1-Regular Papers Short Notes & Review Papers* **32**, 4126 (1993).

[85] J. Junquera and P. Ghosez, "Critical thickness for ferroelectricity in perovskite ultrathin films," *Nature* **422**, 506 (2003).

[86] W. J. Kim, W. Chang, S. B. Qadri, J. M. Pond, S. W. Kirchoefer, D. B. Chrisey, and J. S. Horwitz, "Microwave properties of tetragonally distorted $(Ba_{0.5}Sr_{0.5})TiO_3$ thin films," *Applied Physics Letters* **76**, 1185 (2000).

[87] T. M. Shaw, S. Trolier-McKinstry, and P. C. McIntyre, "The properties of ferroelectric films at small dimensions," *Annual Review of Materials Science* **30**, 263 (2000).

[88] G. Geneste, E. Bousquet, J. Junquera, and P. Ghosez, "Finite-size effects in $BaTiO_3$ nanowires," *Applied Physics Letters* **88**, 112906 (2006).

[89] W. S. Yun, J. J. Urban, Q. Gu, and H. Park, "Ferroelectric properties of individual barium titanate nanowires investigated by scanned probe Microscopy," *Nano Letters* **2**, 447 (2002).

[90] P. Padmini, T. R. Taylor, M. J. Lefevre, A. S. Nagra, R. A. York, and J. S. Speck, "Realization of high tunability barium strontium titanate thin films by RF magnetron sputtering," *Applied Physics Letters* **75**, 3186 (1999).

[91] M. J. Dalberth, R. E. Stauber, J. C. Price, C. T. Rogers, and D. Galt, "Improved low frequency and microwave dielectric response in strontium titanate thin films grown by pulsed laser ablation," *Applied Physics Letters* **72**, 507 (1998).

[92] C. Ang, Z. Yu, and Z. Jing, "Impurity-induced ferroelectric relaxor behavior in quantum paraelectric srtio3 and ferroelectric batio3," *Physical Review B* **61**, 957 (2000).

[93] K. A. W. R. Basceri C, Streiffer SK, "The dielectric response as a function of temperature and film thickness of fiber-textured (Ba,Sr)TiO3 thin films grown by chemical vapor deposition," *Journal of Applied Physics* **82**, 2497 (1997).

[94] J. Bianchi, U. Dec, W. Kleemann, and J. Bednorz, "Cluster and domain-state dynamics of ferroelectric $Sr_{1-x}Ca_xTiO_3$ (x=0.007)," *Physical Review B* **51**, 8737 (1995).

[95] S. E. P. S. P. P. T. E. A. Lemanov, V. V., "Phase transitions and glasslike behavior in $Sr_{1-x}Ba_xTiO_3$," *Physical Review B* **54**, 3151 (1996).

[96] K. A. Parker CB, Maria JP, "Temperature and thickness dependent permittivity of $(Ba, Sr)TiO_3$ thin films," *Applied Physics Letters* **81**, 340 (2002).

[97] R. P. Wang, Y. Inaguma, and M. Itoh, "Dielectric properties and phase transition mechanisms in $Sr_{1-x}Ba_xTiO_3$ solid solution at low doping concentration," *Materials Research Bulletin* **36**, 1693 (2001).

[98] R. Kingsmith and D. Vanderbilt, "1st-principles investigation of ferroelectricity in perovskite compounds," *Physical Review B* **49**, 5828 (1994).

[99] W. L. Zhong, Y. G. Wang, P. L. Zhang, and B. D. Qu, "Phenomenological study of the size effect on phase-transitions in ferroelectric particles," *Physical Review B* **50**, 698 (1994).

[100] S. Chattopadhyay, P. Ayyub, V. R. Palkar, and M. Multani, "Size-induced diffuse phase-transition in the nanocrystalline ferroelectric $PbTiO_3$," *Physical Review B* **52**, 13177 (1995).

[101] M. H. Frey and D. A. Payne, "Grain-size effect on structure and phase transformations for barium titanate," *Physical Review B* **54**, 3158 (1996).

[102] W. Y. Shih, W. H. Shih, and I. A. Aksay, "Size dependence of the ferroelectric transition of small $BaTiO_3$ particleseffect of depolarization," *Physical Review B* **50**, 15575 (1994).

[103] W. Zhong, R. D. Kingsmith, and D. Vanderbilt, "Giant lo-to splitting sin perovskite ferroelectrics," *Physical Review Letters* **72**, 3618 (1994).

[104] P. Debye, *Polar Molecules*, Reprint ed. (Dover Publications, New York, 1929).

[105] H. Frohlich, *Theory of Dielectrics* (Oxford University Press, London, 1958).

[106] K. Cole and R. Cole, *Journal of Chemical Physics* **9**, 341 (1941).

[107] D. Davidson and R. Cole, *Journal of Chemical Physics* **36**, 345 (1951).

[108] S. Havrilia and S. Negami, "A complex plane representation of dielectric and mechanical relaxation processes in some polymers," *Polymer* **8**, 161 (1967).

[109] F. Kohlrausch, *Pogg. Ann. Physik.* **119**, 352 (1863).

[110] G. Williams and D. C. Watts, "Non-symmetrical dielectric relaxation behaviour arising from a simple empirical decay function," *Transactions of The Faraday Society* **66**, 80 (1970).

[111] F. Alvarez, A. Alegra, and J. Colmenero, "Relationship between the time-domain Kohlrausch-Williams-Watts and frequency-domain Havriliak-Negami relaxation functions," *Physical Review B* **44**, 7306 (1991).

[112] M. Glinchuk, "Relaxor ferroelectrics: from cross superparaelectric model to random field theory," *British Ceramic Transactions* **103**, 76 (2004).

[113] L. E. Cross, "Relaxor Ferroelectrics," *Ferroelectrics* **76**, 241 (1987).

[114] D. Viehland, S. J. Jang, L. E. Cross, and M. Wuttig, "Freezing of the polarization fluctuations in lead magnesium niobate relaxors," *Journal of Applied Physics* **68**, 2916 (1990).

[115] V. Westphal, W. Kleemann, and M. D. Glinchuk, "Diffuse phase-transitions and random-field-induced domain states of the relaxor ferroelectric $PbMg_{1/3}Nb_{2/3}O_3$," *Physical Review Letters* **68**, 847 (1992).

[116] M. D. Glinchuk and R. Farhi, "A random field theory based model for ferroelectric relaxors," *Journal of Physics-Condensed Matter* **8**, 6985 (1996).

[117] A. K. Jonscher, "Review-A new understanding of the dielectric relaxation of solids," *Journal of Materials Science* **16**, 2037 (1981).

[118] A. K. Tagantsev, "Vogel-Fulcher relationship for the dielectric permittivity of relaxor ferroelectrics," *Physical Review Letters* **72**, 1100 (1994).

[119] C. Liu, B. S. Zou, A. J. Rondinone, and Z. J. Zhang, "Sol-gel synthesis of free-standing ferroelectric lead zirconate titanate nanoparticles," *Journal of the American Chemical Society* **123**, 4344 (2001).

[120] S. O'Brien, L. Brus, and C. B. Murray, "Synthesis of monodisperse nanoparticles of barium titanate: Toward a generalized strategy of oxide nanoparticle synthesis," *Journal of the American Chemical Society* **123**, 12085 (2001).

[121] J. J. Urban, W. S. Yun, Q. Gu, and H. Park, "Synthesis of single-crystalline perovskite nanorods composed of barium titanate and strontium titanate," *Journal of the American Chemical Society* **124**, 1186 (2002).

[122] K. S. Seol, S. Tomita, K. Takeuchi, T. Miyagawa, T. Katagiri, and Y. Ohki, "Gas-phase production of monodisperse lead zirconate titanate nanoparticles," *Applied Physics Letters* **81**, 1893 (2002).

[123] Y. B. Mao, S. Banerjee, and S. S. Wong, "Large-scale synthesis of single-crystal line perovskite nanostructures," *Journal of the American Chemical Society* **125**, 15718 (2003).

[124] S. Bose and A. Banerjee, "Novel synthesis route to make nanocrystalline lead zirconate titanate powder," *Journal of the American Ceramic Society* **87**, 487 (2004).

[125] T. K. Mandal and J. Gopalakrishnan, "From rocksalt to perovskite: a metathesis route for the synthesis of perovskite oxides of current interest," *Journal of Materials Chemistry* **14**, 1273 (2004).

[126] T. Katagiri, K. S. Seol, K. Takeuchi, and Y. Ohki, "Crystallization of monodisperse lead zirconate titanate nanoparticles produced by laser ablation," *Japanese Journal Of Applied Physics Part 1-Regular Papers Short Notes & Review Papers* **43**, 4419 (2004).

[127] H. Liu, C. G. Hu, and Z. L. Wang, "Composite-hydroxide-mediated approach for the synthesis of nanostructures of complex functional-oxides," *Nano Letters* **6**, 1535 (2006).

[128] C. G. Hu, H. Liu, C. S. Lao, L. Y. Zhang, D. Davidovic, and Z. L. Wang, "Size-manipulable synthesis of single-crystalline BaMnO3 and BaTi1/2Mn1/2O3 nanorods/nanowires," *Journal of Physical Chemistry B* **110**, 14050 (2006).

[129] A. T. Hunt, W. B. Carter, and J. K. Cochran, "Combustion chemical-vapor-depositiona novel thin-film deposition technique," *Applied Physics Letters* **63**, 266 (1993).

[130] C. B. Sawyer and C. H. Tower, "Rochelle salt as a dielectric," *Physical Review* **35**, 0269 (1930).

[131] P. Q. Mantas, "Dielectric response of materials: extension to the Debye model," *Journal of the European Ceramic Society* **19**, 2079 (1999).

[132] A. Pelaiz-Barranco, O. Garcia-Zaldivar, F. Calderon-Pinar, R. Lopez-Noda, and J. F. Betancourt, "A multi-Debye relaxation model for relaxor ferroelectrics showing diffuse phase transition," *Physica Status Solidi B-Basic Solid State Physics* **242**, 1864 (2005).

[133] L. Zhang, W. Zhong, C. Wang, P. Zhang, and Y. Wang, "Dielectric relaxation in barium strontium titanate," *Solid State Communications* **107**, 769 (1998).

[134] L. Zhang, W. Zhong, C. Wang, P. Zhang, and Y. Wang, "Finite-size effects in ferroelectric solid solution $Ba_xSr_{1-x}TiO_3$," *Journal of Physics D-Applied Physics* **32**, 546 (1999).

[135] L. Zhang, W. Zhong, C. Wang, P. Y.P., and Y. Wang, "Size dependence of dielectric properties and structural metastability in ferroelectrics," *The European Physical Journal B* **11**, 565 (1999).

[136] H. C. Chen, C. Yang, L. Fu, Zhao, and Z. Gao, "The size effect of $Ba_{0.6}Sr_{0.4}TiO_3$ thin films on the ferroelectric properties," *Applied Surface Science* **252**, 4171C4177 (2006).

[137] T. Shaw, Z. Suo, M. Huang, E. Liniger, R. Laibowitz, and J. Baniecki, "The effect of stress on the dielectric properties of barium strontium titanate thin films," *Applied Physics Letters* **75**, 2129 (1999).

[138] L. Zhou, P. Vilarinho, and J. Baptista, "Dependence of the structural and dielectric properties of $Ba_{1-x}Sr_xTiO_3$ ceramic solid solutions on raw material processing," *Journal of The European Ceramic Society* **19**, 2015 (1999).

[139] L. Fu Huaxiang, Bellaiche, "Ferroelectricity in barium titanate quantum dots and wires," *Physical Review Letters* **91**, 257601 (2003).

[140] F. H. Naumov II, Bellaiche L, "Unusual phase transitions in ferroelectric nanodisks and nanorods," *Nature* **432**, 737 (2004).

VITA

Liyuan Zhang was born in Quzhou, Zhejiang Province of China, in March 1975. He received his Bachelor degree of Science in Applied Physics from Changchun Institute of Optics and fine Machine,Changchun, China, in 1997. And he received his Master degree of Engineer from Institute of High Energy Physics, Beijing, China, in 2001. Since then, he has been conducting graduate research under supervision of Professor Dragomir Davidovic in the School of Physics, Georgia Institute of Technology.